2018-04-01

Development, Classification and Biomedical Applications of Nano Composite Piezoresponsive Foam

Aaron Jake Merrell
Brigham Young University

Development, Classification and Biomechanical Applications of Nano-Composite Piezoresponsive Foam

Aaron Jake Merrell

A dissertation submitted to the faculty of
Brigham Young University
in partial fulfillment of the requirements for the degree of

Doctor of Philosophy

David T. Fullwood, Chair
Anton E. Bowden
Brian A. Mazzeo
Matthew K. Seeley
Steven K. Charles

Department of Mechanical Engineering

Brigham Young University

ABSTRACT

Development, Classification and Biomechanical Applications of
Nano-Composite Piezoresponsive Foam

Aaron Jake Merrell
Department of Mechanical Engineering, BYU
Doctor of Philosophy

This dissertation focuses on the development of and applications for Nano-Composite Piezoresponsive Foam (NCPF). This self-sensing foam sensor technology was discovered through research in a sister technology, High Deflection Strain Gauges (HDSG), and was subsequently developed with some of the same base materials. Both technologies use nano and micro conductive additives to provide electrically responsive properties to materials which otherwise are insulative. NCPF sensors differ from HDSGs in that they provide a dual electrical response to dynamic and static loading, which is measured through an internally generated charge, or a change in resistance. This dissertation focuses on the development of the dynamic or piezoresponsive aspect of the NCPF sensors which tends to have more consistent electrical response over a larger number of cycles.

The primary development goal was to produce a sensor that was accurate, while providing a consistent, repeatable response over multiple impacts. The hypothesized electric generation is attributed to a triboelectric interaction between the conductive additives and the polyurethane foam matrix. This hypothesis was validated by examining different conductive additives with varying loading levels and specific surface areas while accounting for other design considerations such as the electrode used to harvest the response. The results of this analysis support the triboelectric model and point to carbon or nickel-based additives for optimal performance. The NCPF response measured by digital signal acquisition devices is directly dependent upon its input impedance. Increased input capacitance has a negative effect on the signal, however, higher input resistance has a positive linear correlation to voltage. Other considerations that affect the electrical response include the temperature and humidity in which the sensor is used and result in a scaled electrical response.

NCPF sensors are ideally suited for use in systems which benefit from impact energy attenuation while measuring the same. This work demonstrates how the NCPF sensors can be used to detect severity and location of impacts in systems with multiple sensors (football helmets), and those with one continuous sensor (carpets). When NCPF sensors were used in a football helmet the impact severity and location of impact was accurately identified. NCPF sensors provide the benefit of simplified design by replacing existing foam while providing a direct measure of the forces. Additional research was conducted on the changes in material properties, specifically how it affects the foam structure's ability to absorb energy in quasi static loading scenarios. NCPF sensors are demonstrated as viable tool to measure many different biomechanical systems.

Keywords: triboelectric, special detection, piezoresponsive, self-sensing foam, football helmet, impact detection, impact energy, impact velocity, acceleration, energy absorption

ACKNOWLEDGEMENTS

First and foremost, I would like to express my sincere gratitude and appreciation to my best friend and better half, Melissa, for her endless support. I would also like to thank my little princesses, Makenna, Avonlea, Caitlin and Claire for helping Mom while I was at school.

I also express my gratitude to Dr. David Fullwood for the continuous support offered throughout this dissertation, for his patience, motivation, enthusiasm, and immense knowledge. His guidance was much appreciated throughout my research and writing of this dissertation. I could not have imagined having a better advisor and mentor for my doctorial study.

I would like to thank the rest of my committee: Dr. Anton Bowden, Dr. Matthew Seeley, Dr. Brian Mazzeo, and Dr. Steven Charles, for their insightful comments, and hard questions.

I thank my fellow students and researchers: Taylor Remington, Dean Stolworthy, Adam Bilodeau, Parker Rosquist, Brady Anderson, Evan Bird, Nicole Martin, Cory Newton, Joseph Pace, Jordan Brown, Justin Weaver, Gavin Collins and Trevor Christensen. Their many hours measuring, mixing, casting, drop testing, and analyzing were key to the success of this research.

This material is based upon work supported by the National Science Foundation under Grant No. CMMI-1235365, CMMI-1538447 and NSF STTR-1549719. Any opinions, findings, and conclusions or recommendations expressed in this material are those of the author and do not necessarily reflect the views of the National Science Foundation.

Finally, I would like to thank my parents Ken and Mary Merrell, for supporting me and my family throughout my life, and giving me the experiences that helped me in my endeavors. My parents-in-law Steve and Marilyn Shumway were also a great help and support to me and my family during this wonderful experience.

TABLE OF CONTENTS

LIST OF TABLES

LIST OF FIGURES

1 INTRODUCTIONS AND OVERVIEW

There are many situations in which force or impact measurements can provide useful information pertaining to the interactions between multiple objects. Novel sensing devices are constantly being designed to expand the types of situations in which impact and force data can be gathered. Large-deflection piezoelectric and quasi-piezoelectric sensors constitute a family of such novel devices that have been implemented in a variety of circumstances to measure forces and impacts. Several different materials and topologies have been used in the fabrication of piezoresponsive sensors.

Nano Composite Piezoresponsive Foam (NCPF), the novel multifunctional sensor material studied in this dissertation, is an especially advantageous type of sensor. The sensing foam technology is a derivative technology to the High Deflection Strain Gauges (HDSG) developed at BYU [1-13]. The foam sensor was originally developed to produce a piezoresistive response to pressure, however a secondary response was discovered when the foam was dynamically loaded; it produced an electrical charge.

Initial development of the NCPF sensors focused on the same base additives found in the HDSGs, namely Nickel Nano strands (NiNs) and Nickel Coated Carbon Fiber (NCCF) in a silicone-based foam matrix. Subsequently, foam matrixes and conductive additives were evaluated based on the hypothesized triboelectric generation theory. A polyurethane foam matrix was selected as the standard foam matrix due to its high triboelectric affinity, wide use, large

range of physical properties, facile mixing and east of casting. Several conductive additives were selected for evaluation based on their base material, material geometry/topology and ease of mixing into the matrix. These materials were evaluated based on their contribution to a repeatable and large electrical response to impact.

The ultimate goal of this research was to create a model that predicts the electrical response from NCPF sensors based on conductive additive loading levels, density of the foam, impact characteristics and circuit design. Early in the testing process it was observed that different voltage measurement devices recorded different levels of response. Special considerations were given to the method in which the voltage is measured (circuitry and measurement device) as well as how environmental conditions (temperature and humidity) affect the electrical response. These observations are key to understanding how the NCPF material can be electrically modeled.

NCPF sensors have been used in systems ranging from football helmets for impact detection, to bushings for vibration monitoring, and shoes for gait analysis [14-16]. Analysis of the material performance in these applications has shown relationships between voltage response and acceleration, impact energy, frequency, and magnitude of solitary and vibrational impacts. These systems used discrete sensors to determine locational information. However, it was also demonstrated how NCPF sensors with multiple electrodes can be used to determine the location of impact with high accuracy on a 1D surface.

The final aspect of the NCPF material evaluated how the additives affect the material properties of the foam, specifically energy absorption. This was evaluated by testing the NCPF sensors under quasi static loading conditions with multiple primary and secondary additive densities and secondary fiber lengths. The NCPF sensors' primary function was to measure the

impacts but our analysis showed that the addition of fibers also slightly increased the ability to absorb energy under quasi-static loading.

NCPF sensors provide an accurate and versatile method to measure impact forces as demonstrated throughout this dissertation. Anticipated future NCPF development will focus on the dual sensing ability (simultaneous pressure and impact measurement), energy harvesting (ability to provide power to measurement device), and an electrical model.

Each chapter in this dissertation represents papers that are in various stages of journal publication. Chapter 2 "Development and Evaluation of Triboelectric Nano-Composite Piezoresponsive Foam" outlines the development of the NCPF material. The intrinsic, extrinsic and environmental variables that affect the foam's performance are evaluated through a phenomlogical methodology. This paper led to a NCPF material that could be applied to various applications, some of which are outlined in subsequent chapters. This paper will be submitted for publication in the coming months. This paper was co-authored by Joseph Pace, Evan Bird, Gavin Collins, Trevor Christensen, William Christensen, Anton Bowden and David Fullwood.

Chapter 3, entitled "Spatial Detection of Impact with Piezoresponsive Nano-Composite Foam", demonstrates that once the sensor's specific components are accounted for, one can achieve varying levels of spatial accuracy. The paper demonstrates that different components of the sensor affect the internal triboelectric response within the NCPF which can be adjusted for. This paper will also be submitted for publication before the end of the year. This paper was co-authored by Justin Weaver, Jordan Brown, Trevor Christensen, William Christensen, Anton Bowden and David Fullwood.

Chapter 4, "Nano-Composite Foam Sensor System in Football Helmets", as the title describes, demonstrates the use of NCPF sensors in a football helmet. A football helmet was

evaluated using Virginia Tech's STAR helmet testing procedure with eight NCPF sensors in place of the football helmet's existing pads. The NCPF sensors were shown to provide accurate correlation to several different impact severity measures and demonstrate their potential for use in biomechanical systems. This paper was published in Annals of Biomedical Engineering and was co-authored by William Christensen, Matthew Seeley, Anton Bowden and David Fullwood.

Chapter 5, "Using Nanoparticles and Short Fibers to Increase the Energy Absorption of Foams", demonstrates how the addition of the nano and mico-particles affects the energy absorption of the foam matrix it is added to. This paper evaluates different foam matrices and particle loading levels to determine how each affects the quasi-static energy absorption. The data show that with the inclusion of nano and micro-particles the energy absorption of the foam increases. This paper was co-authored by Matt Harris, Jordan Tanner and Scott Taysom. There are plans to add dynamic energy absorption tests to this paper and publish the findings in one paper.

In addition, there are five patents that have resulted from the above-mentioned research including: Composite Material used as a Strain Gauge (piezoresistive and piezoelectric), Shoe-Based Analysis System, Thermally Conductive Composite Foam and Polymeric Foam Deformation Gauge.

2 DEVELOPMENT AND EVALUATION OF TRIBOELECTRIC NANO-COMPOSITE PIEZORESPONSIVE FOAM

2.1 Abstract

Nano Composite Piezoresponsive Foam (NCPF), the sensor material studied in this paper, is an especially advantageous type of sensor which provides impact mitigation while also providing sensing capability through an internally generated electrical response. The hypothesized triboelectric effect is evaluated by assessing internal and external influences on the NCPF sensors. Multiple conductive additives with similar base materials, but vastly different geometries, were considered based on their ability to generate a consistent and large triboelectric charge. To ensure results from this and other analysis could be translated to measurements recorded from different digital signal acquisition devices (DAQs), the internal impedance of several DAQs were evaluated. The NCPF response is directly dependent upon the DAQ's input impedance. Increased input capacitance has a negative effect on the signal, however, higher input resistance has a positive linear correlation to voltage. By knowing the internal impedance of each DAQ the signal can be scaled to directly compare results.

Physical and electrical characteristics of each NCPF sample were measured and differences between additives were evaluated. A wide range of operating conditions were evaluated to determine their influence on the electrical response of the NCPF sensors. After all primary additives were considered, F104 graphite and nickel powder, were shown to provide the

most accurate and repeatable electrical response to impacts. Their electrical response was consistent throughout all levels of loading regardless of the model (categorical or continuous). Furthermore, all data provided evidence to support the internal triboelectric generation theory of the NCPF.

Key terms: Triboelectric, phenomenological, piezoelectric foam, self-sensing foam, bulk resistance, digital acquisition devices, temperature, humidity

2.2 Introduction

There are many situations in which force or impact measurements can provide useful information pertaining to the interactions between multiple objects. Sensing devices have recently been designed to expand the types of situations in which impact and force data can be gathered. Large-deflection piezoelectric and quasi-piezoelectric sensors constitute a family of such devices that have been implemented in a variety of circumstances to measure forces and impact energy. Several different materials and topologies have been used in the fabrication of piezoelectric sensors. For example, Lin et al. produced a piezoelectric sensor by placing a zinc oxide textured film between two sheets of polydimethylsiloxane film [17]. Wang et al. utilized polyvinylidene fluoride fabric between two electrodes as a force sensor [18]. Souri, Nam, and Lee showed that polyurethane combined with zinc oxide, copper, and multi-wall carbon nanotubes (MWCNTs) acted as a piezoelectric sensor [19]. Hwang developed a piezoelectric sensor from polyurethane with $BaTiO_3$ particles added to enhance the piezoelectric effect of the sensor [20]. Wegner et al. applied a large electric field to charge the surface of the of the foams internal voids to create a piezoelectric sensor [21]. These systems rely on different internal

electrical phenomena to create their sensing properties and allow for dynamic sensing in diverse applications.

Nano Composite Piezoresponsive Foam (NCPF), a multifunctional sensor material studied in this paper, is an especially advantageous type of sensor. The polymeric foam base gives the sensor high flexibility and versatility, while the distributed conductive nano-network provides sensing capability in all directions and unlimited topologies. The foam sensor can be embedded in objects of interest for detecting forces and impacts without altering the properties of the original components. This is accomplished by manipulating the foam matrix's density or chemistry to match the stiffness of the material of interest [22]. For example, the stiffness of the sensor has been tailored to match the stiffness of the protective foam inside of sports helmets to measure the magnitude of impacts to the head as they occur while retaining the protective function of the helmet [14]. Alternatively, the stiffness of the sensor has been matched to that of shoe insoles, and embedded in shoes, to measure ground reaction forces and evaluate aerobic energy output [23, 24]. The material has also been used to replace a bushing in order to measure vibrations in mechanical systems [15].

In addition to wide range of material properties granted to the NCPF by the foam matrix, these sensors also allow for flexibility in tailoring the magnitude of the electrical response through the choice of conductive nanoparticles, loading percentage, and size of NCPF sensor. The foam sensors consist of a polyurethane matrix with electrically conductive nanoparticle fillers dispersed throughout the matrix. The conductive nanoparticles include both a primary and a secondary filler. It is hypothesized that the quasi-piezoelectric response of the foam occurs as a result of a triboelectric effect between the polymer matrix and the combination of the nanoparticle fillers and the electrical circuit embedded in the foam. This hypothesis was assessed

through the development and optimization of the NCPF sensors; the evaluation of which was separated into intrinsic, extrinsic and environmental effects.

Intrinsic Considerations – the NCPF's internal triboelectric effect was studied by evaluating multiple nanoparticle fillers, their effects on the bulk properties of the foam, and the circuit used to measure the response.

Extrinsic Considerations – the voltage measurement device was expected to affect the measured voltage response from the NCPF, thus multiple digital signal acquisition devices were evaluated to determine their internal impedance, and its effect on the recorded voltage signal.

Environmental Effects - temperature and humidity were evaluated to determine their effect on the internal charge generation.

Intrinsic Considerations – The NCPF sensors generate an internal electrical charge upon impact that was hypothesized to come from a combination of triboelectric interactions: the interaction between the conductive nanoparticle additives and the polyurethane foam matrix, and the interaction between the NCPF and the conductive electrodes used to measure the response. The nanoparticle fillers in the NCPF sensor act as a conductive network generating the charge and transferring it to the electrical leads to be detected. Thus, the ideal filler maximizes charge generation from the triboelectric effect and provides an adequate electrical network to efficiently transfer the charge to the electrical leads.

Preliminary studies involving nickel nanoparticles in piezoresistive strain gauges have shown that a secondary filler, nickel-coated carbon fiber, serves as a backbone in the conductive network, and increases the composite sensor's sensitivity [25]. Thus, in this study, the amount of secondary filler by weight percent was held constant while the type and amount of material used

as the primary filler were optimized. Candidate materials selected as the primary filler in the foam sensor included nickel nanoparticles, carbon black, milled carbon fiber (PX30), graphite (M103, F104, P103), dendritic copper, and multi-walled carbon nanotubes (MWCNT). Interestingly, most of these candidate materials have been found to contribute to the piezoresistive behavior of sensors [12, 26-30]. It was expected that the different additives would affect the bulk properties of the foam, such as the bulk resistance and the void sizes. These properties were evaluated to determine to what extent they affect the NCPF electrical generation.

The internal NCPF charge generation was gathered through an electrical probe that was placed on or in the NCPF. The electrical probe was made from a metallic material which has a triboelectric affinity similar to the nanoparticles and can potentially generate additional charge measured by the digital signal acquisition device. The effects of the electrical probe were evaluated to determine to what extent they affected the measured response.

Extrinsic Considerations – The NCPF sensor systems can be separated into two different electrical subsystems, the NCPF and the digital signal acquisition device (DAQ) used to measure the response. Lenicek et. Al and others have demonstrated that a DAQs voltage reading can be affected by its input impedance [31, 32]. It is proposed that the first step in understanding the NCPF's electrical characteristics is to understand the DAQ's internal impedance. The internal impedance of several DAQs is evaluated representing inexpensive consumer to expensive research related devices.

Environmental Effects – The environmental conditions in which the NCPF will operate can affect the sensors in one of two ways; it will change the material properties of the foam matrix or change the electrical properties of the sensor. Many polyurethane foam matrices have temperature dependent material properties; as the foam's temperature increases it generally

becomes softer. NCPF's electrical response has been shown to be directly dependent upon total strain and strain rate and is therefore dependent upon temperature. Additionally, it is expected that the internal humidity of the NCPF would affect the bulk electrical properties, changing the electrical response to impacts.

2.3 Methods

2.3.1 Intrinsic Considerations

As two different materials come into contact, or rub against each other, they will either take away, or give up electrons. This phenomenon is referred to as the triboelectric effect and has been widely documented in charge harvesting devices [33-40]. The direction of charge transfer is dependent upon the triboelectric affinity of each material and the extent of the motion between the two materials. The material that takes the electrons from the other has a stronger affinity for negative charge or a more negative triboelectric affinity. There have been many different studies

Table 2-1: Several materials with their associated triboelectric affinities.

Material	Affinity (nC/J)
Polyurethane foam	+60
Polyurethane	+40
Nylon	+30
Glass	+25
Wool	0
Metals (Nickel, Copper)	-
Acrylic	-10
Polystyrene, Carbon Black	-70
Silicone	-72
PVC	-100
Latex natural rubber	-105
Teflon	-190

that attempt to quantify the triboelectric affinity of different materials into a series [41-46]. One of the most complete triboelectric series was created by AlphaLab Inc. and a portion of it is listed in Table 2-1[37]. However complete, this table doesn't list any of the carbon-based additives that are studied in this paper, but it does list metallic based materials (copper and nickel). While carbon-based materials are not widely reported in the triboelectric scale, one study found carbon black to have an affinity similar to polystyrene [47]. For the purpose of our study, we will classify all carbon-based materials in the negative range between the metallic materials and carbon black.

2.3.1.1 Additive selection and Sample Preparation

The NCPF fillers were classified as either a primary or secondary stabilizing filler. The primary filler selection focused on conductive particles with approximately the same conductivity and particle size as the nickel nano-strands used in early material development [48]. Foam samples incorporating the different candidate primary fillers with varying loadings were manufactured for testing. The primary fillers selected for testing were nickel nanoparticles,

Table 2-2: Primary additives used in analysis with material properties.

Additive	Base Material	Particle Size (µm)
Nickel Powder	Nickel	37 (400 Mesh)
Carbon Black	Carbon	44 (325 Mesh)
Multi-Walled CNTs	Carbon (94%)	.05 x 10
Milled Carbon Fiber	Carbon (99%)	7.2 x 100
M103	Graphite (99% Carbon)	5-7
F104	Graphite (96% Carbon)	8-12
P103	Graphite (85% Carbon)	10-15
Copper Powder	Copper	37 (400 Mesh)

carbon black, milled carbon fiber, Multi-Walled Carbon Nano Tubes (MWCNTs), graphite flakes, and dendritic copper. The nickel nanoparticles were Novamet 525 conductive nickel powder, a filamentary powder whose particles have a branch-like structure. The milled carbon fiber was produced by ZOLTEK from standard 7.2 μm diameter fiber milled to a length of approximately 100 μm. The Vulcan XC72 conductive carbon black was produced by Cabot Corporation and was selected based on its high conductance. The MWCNTs were produced by Graphene Supermarket and have a diameter of 50-85 nm with a length of 10-15 micrometers. All graphite fillers tested were produced by Carbon Graphite Materials, Inc., and were selected based on particle size, structure, and carbon content. M103 is a natural crystalline flake graphite with an average particle size of 6 microns and a carbon content of 99%. F104 is a natural crystalline flake graphite with an average particle size of 10 microns and a carbon content of 96%. P103 is a natural amorphous micro-crystalline graphite with an average particle size of 12 microns and a carbon content of 85%. The dendritic copper is sold by Novamet Corp with all particles being screened with a 400 mesh. The secondary stabilizing filler is a nickel-coated carbon fiber (NCCF) with a length of 1 mm coated by Conductive Composites, LLC. A summary of all the primary additives previously described are shown in Table 2-2.

Each filler material was evaluated at three loading percentages: 2, 6 and 10% by weight for all materials except the MWCNTs which were 0.33, 0.67 and 1% by weight. When the MWCNTs were loaded with anything above 2% they wicked up a large portion of the liquid foam components resulting in a non-producible mixture. The resulting loadings were selected based on the max percentage that resulted in similar foam properties of the other samples.

In addition to the above-described samples, multiple control samples were manufactured to identify secondary filler effects. The control samples were made with the same medium loading

of primary filler as above described but no secondary NCCF filler. These samples were used to evaluate to what extent the secondary stabilizing NCCF filler contributes to the NCPF triboelectric response. In previous work, with non-foamed silicone strain gauges, the filler was determined to stabilize the signal and create a more robust sensor [9, 25].

The NCPF samples in this study were prepared in a cylindrical mold with a diameter and height of 3.81 and 2.54 centimeters respectively. The sample preparation began by placing copper wires through holes on the side of a cylindrical mold, which are used to measure the electrical response. The ends of the wires on the inside of the mold were stripped and splayed so that the foam surrounded and adhered to them after the mixture was poured into the mold. Preparation of the foam mixture began by thoroughly mixing the specified amount of primary filler and secondary filler with the polyol component of the polyurethane matrix.

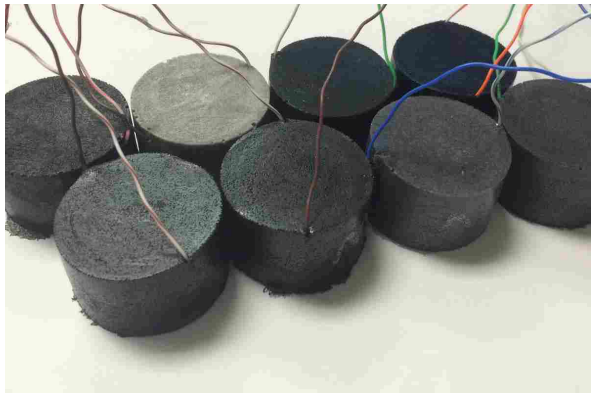

Figure 2-1: NCPF samples with different additives and loadings.

Mixing was initially hand mixed to wet the particles and followed by a more through mixing in a centrifugal mixer. Then, the isocyanate component of the polyurethane matrix was added to the mixture. The mixture was briefly stirred by hand and then returned to the centrifugal mixer to finalize the mixing process. The mixture was then promptly poured into an aluminum

heated mold and covered by a flat plate to confine the mixture to the desired cylindrical shape. After curing, the foam was removed from the mold and allowed to rest approximately 24 hours before being subjected to testing to ensure that the sample had fully cured. The order of production of the various samples was randomized to reduce bias in manufacturing. Figure 2-1: NCPF samples with different additives and loadings. Figure 2-1 depicts the diversity of samples tested in this study, the different primary fillers are apparent by their effect on the sample colors.

2.3.1.2 Primary Additive Topology

The morphology of each primary additive was evaluated by an Environmental Scanning Electron Microscope (ESEM) and a Brunauer-Emmett-Teller (BET) analysis. ESEM images were collected with an FEI/Philips XL30 and were used to identify general shape and morphology of each additive. The additives were prepared by adhering a small portion of each additive to a flat-topped SEM pin stub with some conductive carbon paint. A small portion of the paint was placed on the top of the stub and was dipped into the additive. The loose material was removed by tapping the side of the stub. Each specimen was evaluated at three different magnifications, 250, 2500 and 50,000, to evaluate macro, micro and nano characteristics of each additive. Surface area for each additive was evaluated by Micromeritics Tristar 3000 BET system, which can measure up to three separate samples simultaneously. Each sample was placed into a glass vial that was previously cleaned and weighed. To ensure accurate surface area evaluation, the mass of each sample was carefully weighed by taking the average of four separate measurements. Before the mass of the sample was appropriately recorded, the samples went through a degassing process. Degassing is accomplished by heating the samples to 120° C while flushing the particles with Helium gas with a loose stopper on top of the vials for at least 24 hours. After degassing and measuring the mass, the samples were placed on the BET machine

and submerged in liquid nitrogen to ensure a constant temperature of 77 K during the twelve-hour test. A standard BET analysis was carried out on each sample using nitrogen as the absorptive gas, which resulted in a BET surface area measurement of m^2/g for each sample.

2.3.1.3 Void Size

In a commercial production setting void size of polyurethane foam can be controlled by adjusting the amount of blowing agent or by creating the voids through the introduction of air and agitation. Void size is not controlled in the lab, rather observed. All NCPF samples used in this analysis were manufactured in a lab by hand with a polyurethane matrix, which uses a blowing agent to foam the NCPF. The process was controlled as far as possible, but differences between samples are inevitable. To evaluate the effects of internal NCPF structure, and not the variance in manufacturing on the electrical response, the internal void sizes of the sensors were evaluated. The foam matrix used in these tests forms a skin on the surface where it contacts the mold during casting. The foam's skin exhibits a different mechanical structure than the internal portion of the foam, with little to no voids. The skin was found to be about 1 mm thick on all samples. Two slices, 2.4 mm thick on average, were cut from the edge of each cylindrical NCPF sensor to ensure the internal structure was adequately represented. The second slice which was approximately 4.8 mm internal to the sensor was evaluated with an Olympus GX51 inverted optical microscope. Twenty voids were measured for each sample under the assumption that the voids were perfect ellipses and an average void size was recorded. These measurements were then evaluated against each NCPF's composition to determine whether they affected the macrostructure of the foam.

2.3.1.4 Bulk Resistance

Two separate evaluations were completed on the resistance measurements: a secondary additive effect, and a primary additive effect. As previously described, the secondary additive has been incorporated into sensors based on evidence in early development that it enabled a more consistent sensor reading [9, 25]. The primary additive evaluation will identify how additive level and additive type affect the bulk resistance. The resistance of the NCPF samples was measured from the same samples that were used for measuring the void size. Each slice of foam was measured for sample thickness on all four corners and recorded. There were some variations in sample dimensions, but each sample was cut to approximately 2 x 25 x 25 mm. The excess foam was removed from the larger samples to ensure consistent samples size and average sample thickness was recorded. Additionally, each sample was marked to indicate the direction that the foam rose, and measurements were recorded accordingly. A printed circuit was created which had two copper pads 4 mm apart which were connected to a General Radio 1863 Megohmmeter with wires that were soldered to the board. Each slice of foam was placed on top of the circuit with a non-conductive weight made of Teflon. The Teflon weight provided enough pressure to keep the foam in contact with the board without compressing the foam. The resistance of each sample was recorded from four separate directions: from top to bottom, left to right, right to left, and bottom to top. These measurements were then averaged to negate any effects from rising direction on foam conductivity.

2.3.1.5 Conductor Generation vs Foam Generation

Triboelectric voltage generation is present wherever there are two materials with varying triboelectric affinities that encounter each other. To evaluate the effect of the conductor's surface area within a wire-based system, two 7.5 cm x 7.5 cm x 2.5 cm samples of foam, one neat (no additives) foam, and one NCPF, were created. The samples contained multiple wires, which were cast through the middle of the sample with a custom mold as shown in Figure 6. When casting the NCPF, two of the eleven wires were inadvertently moved during casting and were determined to be unreliable, and thus were not used in this analysis. Each probe consisted of a solid copper wire with a diameter of 0.5mm. The wire probe was cast in the foam in a straight line through the foam allowing the surface area to be calculated by multiplying the circumference of the wire by the width of the foam, each wire having a surface area of 117.81 mm^2.

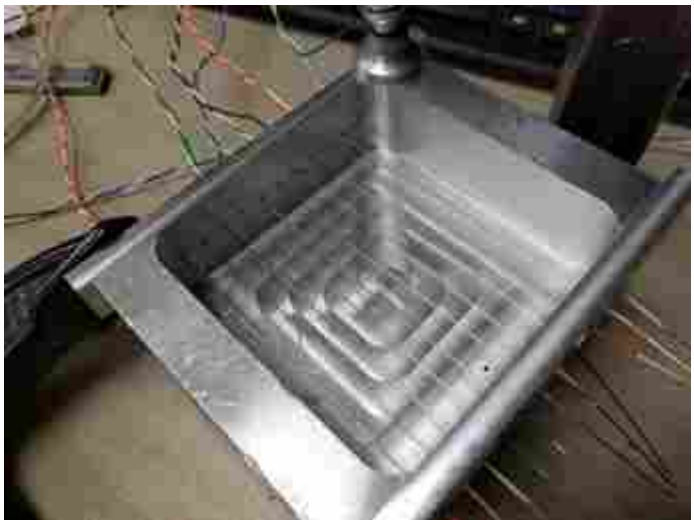

Figure 2-2: Mold setup prior to casting Neat and NCPF samples to evaluate the conductor voltage generation.

Each foam sample was tested by starting with all usable wires connected to the voltage measurement device and subsequently removing a random wire until only one wire remained connected. The wires were removed randomly to eliminate any bias in the data due to wire location. Each wire configuration was tested by impacting the sample five times. The entire test was repeated, resulting in a total of 90 impacts on the NCPF foam and 110 on the Neat foam.

2.3.1.6 Impact tests

All impact tests throughout this paper, with the exception of the temperature and humidity tests, were performed using an Instron Dynatup 8200 drop tester with a cylindrical drop head 10.5 cm in diameter. Since the correlation between impact energy and voltage output by the foam was of interest, three different drop heights were used to produce variable impact energies. These heights were 47 cm, 67 cm, and 84 cm. Each sample was impacted multiple times using all three drop heights. Energy calculations were based on the calculated potential energy of the impact head using:

$$E_{Impact} = mgh \tag{2-1}$$

where m is the mass of the impact head in kg, g is the gravitational constant of 9.81 m/s^2 and h is the height of the impact head in meters. Velocity was calculated by converting all potential energy to kinetic energy using:

$$V = \sqrt{2gh} \tag{2-2}$$

where g is the gravitational constant and h is the height of the drop head. The voltage response from the NCPF sensors was recorded by connecting the wire leads in the foam sensor the previously described microcontroller.

Figure 2-3: Modified Instron drop testing apparatus used in testing NCPF sensors.

The order of testing of the foam samples and the corresponding drop height for each test were randomized. In each test, the foam sensor was positioned beneath the cylindrical drop weight. The sample was held in place by securing the sample to the platform of the Instron drop tester with pressure sensitive cloth tape (duct tape). The tape covered the top of the sample, which also served to electrically isolate the sample from the drop weight. Additional precautions to limit the amount of electrical interference included lining the drop weight and platform of the drop tester with tape. After the sensor was positioned, the wire leads were connected to the microcontroller. Following preparation of the apparatus, the sample was subjected to five impacts of the drop weight from the prescribed height. Figure 2-3 depicts the setup of the testing apparatus used in this study.

2.3.2 Extrinsic Considerations

2.3.2.1 Digital Signal Acquisition Device Characteristics

Early in the testing of NCPF sensors it was observed that the measured response from the sensors changed dependent upon the Digital Signal Acquisition Device (DAQ) used to measure it. This inconsistency requires that each new DAQ be calibrated to draw correlations to the NCPF's electrical response. Multiple DAQs were evaluated to determine the differences in observed NCPF electrical response and how the input impedance affected said response. Furthermore, the input impedance of several DAQs were adjusted to match each other and tested again. By correlating the DAQs input impedance to measured NCPF response, the results from this paper can be translated into future work and other DAQs.

Six DAQs were evaluated, representing consumer to research level devices. An Arduino Uno R3 represented a common, inexpensive ($20) consumer-based system with voltage measuring capabilities. The National Instrument NI-9234, NI-9229, and NI-9215 signal acquisition modules represented expensive ($2,400) devices that are used almost exclusively in research. The other two devices represented a mid-level multimeter ($400) and a custom microcontroller ($150). The custom microcontroller was developed specifically for measuring and recording the NCPF response in a small form factor. The board was designed to record the data to an onboard microSD card and stream the data through Bluetooth to an iOS device.

Each DAQ was connected to a custom circuit as shown in Figure 2-4. The waveform generator and both Oscilloscopes represented in the circuit are all contained in the Analog Discovery™ device made by Digilent. This device was selected due to the internal timing synchronization of the waveform generator and the Oscilloscopes, facilitating correlations and

network analysis. The Oscilloscope used to measure V_{in} and V_{out} has an advertised input resistance of 1 MΩ and an input capacitance of 24 pF. These values were evaluated through a circuit analysis to ensure accurate measurement of the DAQ's input resistance and capacitance.

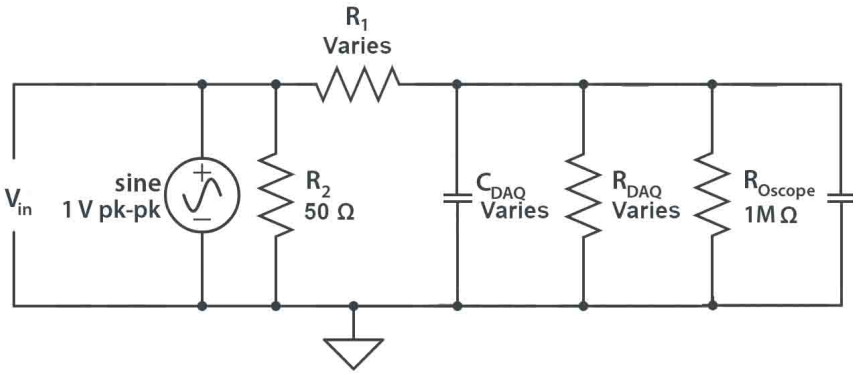

Figure 2-4: Modified circuit to represent the internal impedance of the DAQ and the oscilloscope.

The input resistance of each DAQ was evaluated by connecting the waveform generator with a 1-volt peak-to-peak sinusoidal input voltage (V_{in}) at various frequencies between 1 Hz and 1 kHz while adjusting R_1 until the output voltage (V_{out}) was half V_{in}. The circuit can be evaluated as a modified voltage divider circuit, which accounts for the internal impedance of the oscilloscope. The input resistance of the DAQ can be calculated using:

$$R_{DAQ} = R_1 * \frac{1}{\left(\frac{V_{in}}{V_{out}} - \frac{R_{Oscp} + R_1}{R_{Oscp}}\right)} \tag{2-3}$$

where R_{DAQ} represents the internal resistance of the DAQ, R_1 is the series resistor, R_{Oscp} is the internal impedance of the oscilloscope, V_{in} and V_{out} represent the input and output voltages.

Before any circuit analysis could be performed on the DAQs each component of the circuit, including the wave generator and oscilloscopes, was scrutinized to ensure complete characterization. The circuit was evaluated by passing a 500-point logarithmic voltage sweep,

from 10 Hz to 1 MHz, with a peak to peak voltage of 2 volts. The output signal from the circuit was compared directly to that of a model of the same. The circuit model was evaluated at 100 different capacitance values in .33 pF steps around an initial estimated capacitance with a custom written script. The V_{out} from the model was compared to the measured V_{out} of the Oscilloscope throughout a logarithmic sweep from 10 Hz to 1 MHz with 500 points. Each model output, with separate capacitor values, was evaluated by the Root Mean Squared Error (RMSE) and was plotted against frequency. The minimum point was identified, and the associated capacitance value was selected as the capacitor value for Oscilloscope. The resulting model demonstrated a larger input capacitance (36.5 pF) for the Oscilloscope than was advertised (24 pF) and was used as the input capacitance for all DAQ characterization tests.

With the measurement circuit properly characterized, each DAQ was evaluated in its standard configuration to determine the input capacitance. A 500-point logarithmic voltage sweep, from 10 Hz to 1 MHz, with a peak to peak voltage of 2 volts was used to evaluate the frequency response of each DAQ. The measured V_{out} was compared to theoretical V_{out} by a custom script to identify the input capacitance of each DAQ. Subsequently, the NI-9229 and NI-9215 were adjusted with parallel resistors and capacitors to match the input impedance of the NI-9234 and tested again with the circuit to verify impedance. Once the input impedance was characterized, the National Instrument DAQs were used to measure the voltage response from a .12 x 19 x 19 cm sample of NCPF. The NCPF sample was impacted ten times with a 6.82 kg mass from .46 meters with a 125 mm^2 impact head resulting in an impact energy of 30.78 J. The peak voltage was recorded and analyzed against the different input impedance characteristics of each DAQ in their standard form and then again with their matched impedance.

With the input impedance of the DAQ quantified the charge that the NCPF sensors can generate can be calculated using:

$$Coulomb = V * C \tag{2-4}$$

where V and C are the measured voltage and input capacitance of the DAQ respectively. The peak voltage was used as V in this equation to demonstrate the peak charge the NCPF sensor can generate.

2.3.3 Environmental Effects

The sensors used in this analysis (provided by Nano Composite Products, Inc.) were commercially manufactured by Rogers Corporation with 3% NCCF and 15% nickel powder by weight. The NCPF samples were cast onto both sides of a thin aluminum-coated PET film to a thickness of 4mm. Once cured, individual sensors were cut from this foam sheet to samples 25 x 51 x 4 mm. A small tab of the conductive film was left exposed as a medium to collect the voltage signal from the sensor.

The environmental tests were performed with a different impact tester than previous tests, which allowed for cyclic impacts over a longer period of time. A custom-built, cyclic drop testing machine, with an impact mass of 450 g and a drop height of 12 mm, was used for all environmental tests (Figure 2-5). The machine creates the cyclic impacts by rotating a pair of snail cams on an axel, which lifts, and subsequently drops the carriage that impacts the NCPF samples. The impact rate can be adjusted by changing the speed of the DC motor that is attached to the axel, however, all tests were performed between 0.86 and 0.93 Hz. The carriage was outfitted with an accelerometer (Vernier 25-g Accelerometer, connected to a LabQuest®2 data

collection module) to quantify the magnitude of each impact, tracking any deviations in input which could affect the NCPF response. The NCPF sample is electrically isolated from the impact machine by two nylon blocks, one on top and one underneath the NCPF sample. The entire testing apparatus was enclosed in an acrylic box into which different temperature and humidity conditions could be applied and measured.

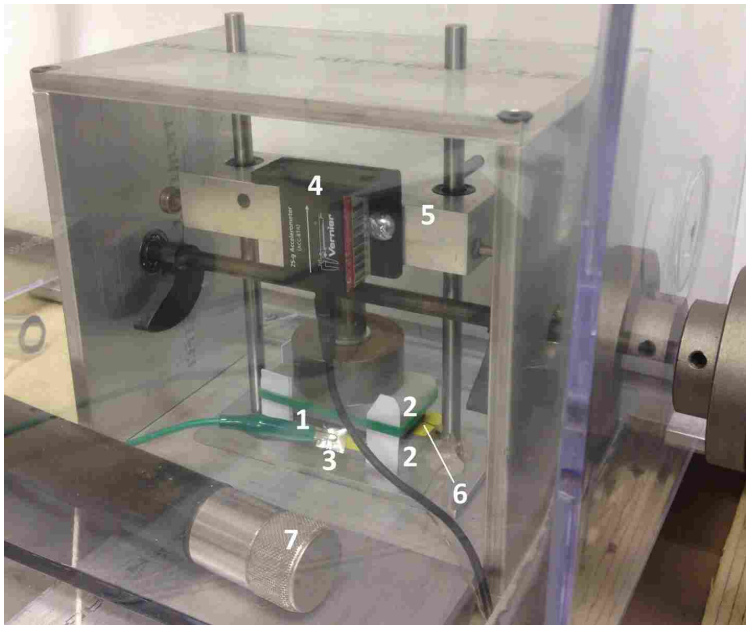

Figure 2-5: NCPF sensor (1) positioned between electrically-insulating nylon blocks (2) to sense impacts from a cyclic drop testing machine. Voltage data was collected by connecting the NCF sensor's conductive film (3) to an A/D channel of a custom-built microcontroller (not shown). Acceleration data was gathered through an accelerometer (4), mounted to the front of the weight carriage (5). Temperature data was collected through a thermocouple (6) inserted between underside of NCPF sensor and bottom nylon block. Humidity data was gathered through a hygrometer probe (7) situated near the sensor. The entire system is encased in an acrylic box to allow temperature and humidity control.

2.3.3.1 Humidity

Humidity was applied to the box at varying levels with a Honeywell MistMate HUL520P humidifier, measured by an Omega RH-201 hygrometer. Due to the size of the hygrometer, it measures the humidity of the box and approximates the internal humidity of the NCPF. It is unlikely that the humidity of the chamber directly matches the internal humidity of the NCPF but due to alternative testing equipment, this measurement is used. However, from an initial evaluation of the humidity and NCPF, response, it appears as though the chamber's humidity correlates well with the internal humidity of the sensor and will be used for the purposes of this paper (Figure 2-6). The chamber was exposed to 15 different steady-state humidity levels ranging from 35-95% RH, which represents the widest range of humidity possible with testing equipment. To ensure possible damage to the sensor didn't confound the results all of the humidity tests were performed in a random order. Additionally, the temperature and acceleration were found to be consistent across all tests.

2.3.3.2 Temperature

To evaluate the effect of temperature on the NCPF sensors, the box was heated to five separate steady-state temperatures between 21.5 and 31° C. The system's temperature was measured between the NCPF sensor and the nylon block placed beneath it at 5 Hz with a National Instruments LabVIEW DAQ system. When the internal temperature reached a steady state, the impact machine ran at 0.85 Hz for 10 min and recorded the following: the NCPF

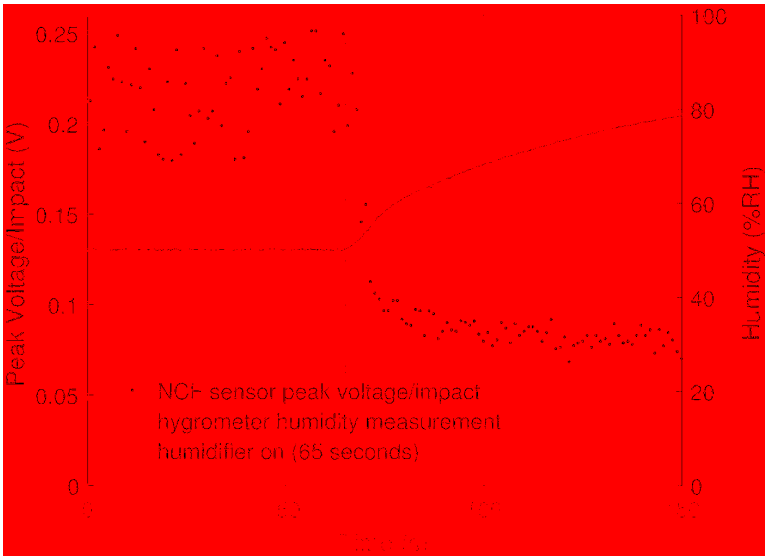

Figure 2-6: Data showing the NCPF response with relation to the humidity of the testing chamber.

response (with the custom micro-controller previously described), the temperature and the acceleration of each impact. All five temperature tests were performed in random order and at least 22 hours of rest time was allotted before the next test. It was determined that humidity changed significantly throughout the tests, which required the voltage response be normalized with respect to humidity using the model developed in the humidity tests.

2.3.4 Data Processing

All NCPF voltage data for the intrinsic analysis were collected at 1000 Hz with the custom microcontroller previously described. The sampling rate was preset on the microcontroller and was selected to be two to three times the Nyquist frequency of the NCPF response. All data was post-processed with a 5^{th} order lowpass Butterworth filter with a cutoff frequency of 200 Hz. The resulting filtered signal is easier to process for further analysis. The upper cutoff frequency was selected by evaluating the Fourier transform of the raw signal. By evaluation of the FFT

frequencies in Figure 2-7, one can see most of the signal is comprised of frequencies ranging from 0 up to 100 Hz, however, there is another band between 100 and 200 Hz that is picked up with the 200 Hz cutoff.

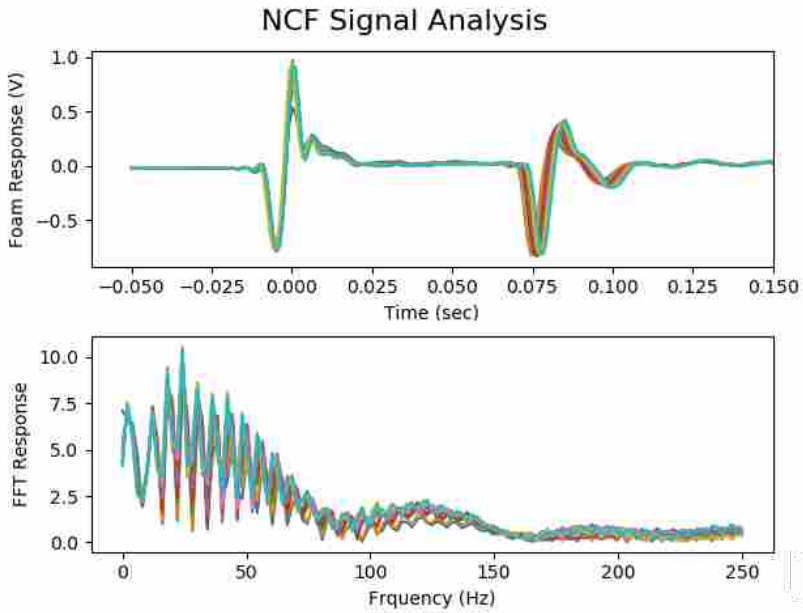

Figure 2-7: Typical NCPF response to impact, both plots show the analysis of 10 separate impacts. Top: FFT vs frequency response. Bottom: NCPF voltage response vs time.

2.4 Results

Multiple criteria were used in defining the optimal performance of the foam sensor. The purpose of the sensor is to predict the magnitude of impacts applied to the sensor based on voltage output readings, so a high correlation between impact energy and voltage response was desired. Additionally, a consistent readings of equal impact energy and a large signal to noise ratio are considered desirable. Finally, the cost of the primary additive material was a consideration in arriving at the optimal composition of the foam sensor.

2.4.1 Intrinsic Considerations

After all impact testing was completed, physical characteristics of the foam were recorded to determine if manufacturing variance, or additive effects, contributed to the difference in samples. If the measure was found to be significant between additives, it was used in the final model to evaluate the efficacy of the additives.

2.4.1.1 Primary Additive Topology

The results from the BET analysis confirm that the additives selected represent a wide range of specific surface areas (Figure 2-8). MWCNTs were found to have the largest specific surface area followed by carbon black, all three graphite materials, the metallic powders, and the milled carbon fiber. The milled carbon fiber specific area was determined based on specs provided by the supplier. All calculated surface areas along with the specifics of the BET

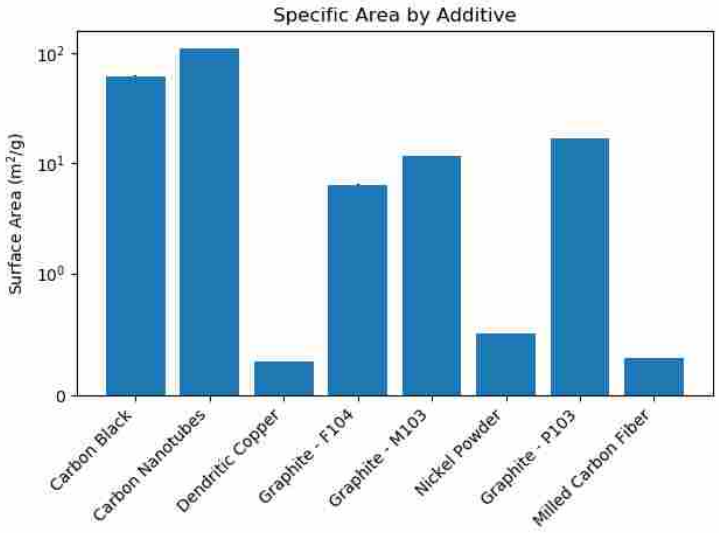

Figure 2-8: BET and calculated surface area of primary additives.

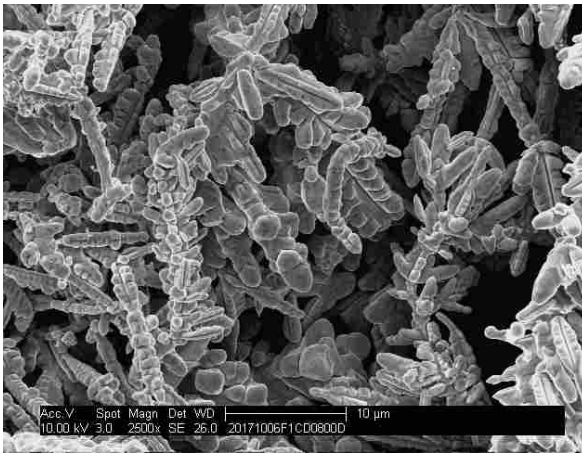

Figure 2-9: SEM image of the dendritic copper powder at 2,500X.

analysis, can be found in Appendix A. The results of this analysis were then used to determine the theoretical surface area of the additives in each sample by multiplying the specific surface area by the weight percent and sample weight. The resultant values were then evaluated for their effect on the different material and electrical characteristics of the NCPF samples.

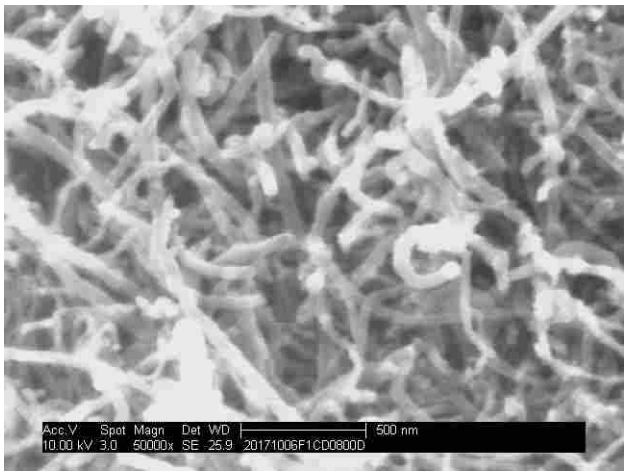

Figure 2-10: SEM image of high aspect ratio MCNTs.

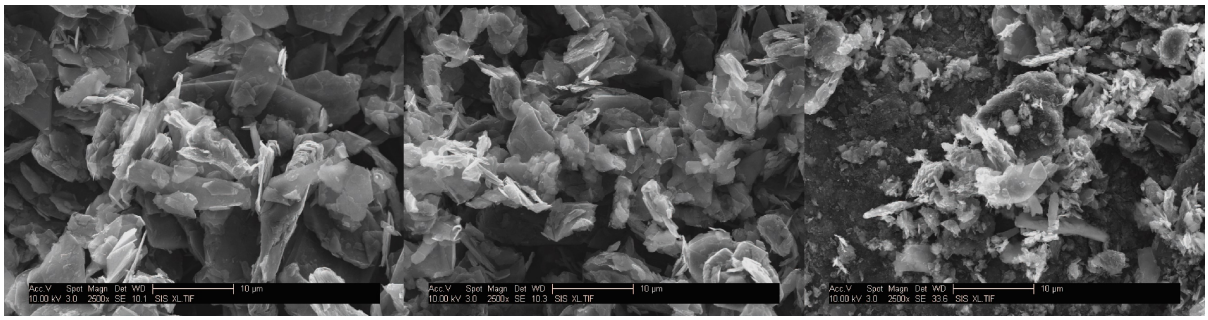

Figure 2-12: SEM images from flake additive category F104, M103, and P103 (from left to right). All samples are magnified to 2500X.

To determine if the general shape of the additive had any significance in its performance each additive was classified into one of four categories based on an evaluation of the SEM images. The four categories selected were flake, filamentary powder, dendritic powder, and high aspect ratio tubes. All three graphite powders had similar shape and structure and were classified as flaked structure (Figure 2-12). The carbon black and nickel powder had very similar filamentary structure but on vastly different scales (Figure 2-11). MWCNTs and milled fiber were both tubular in shape with high aspect ratio, MWCNT are shown in Figure 2-11. The

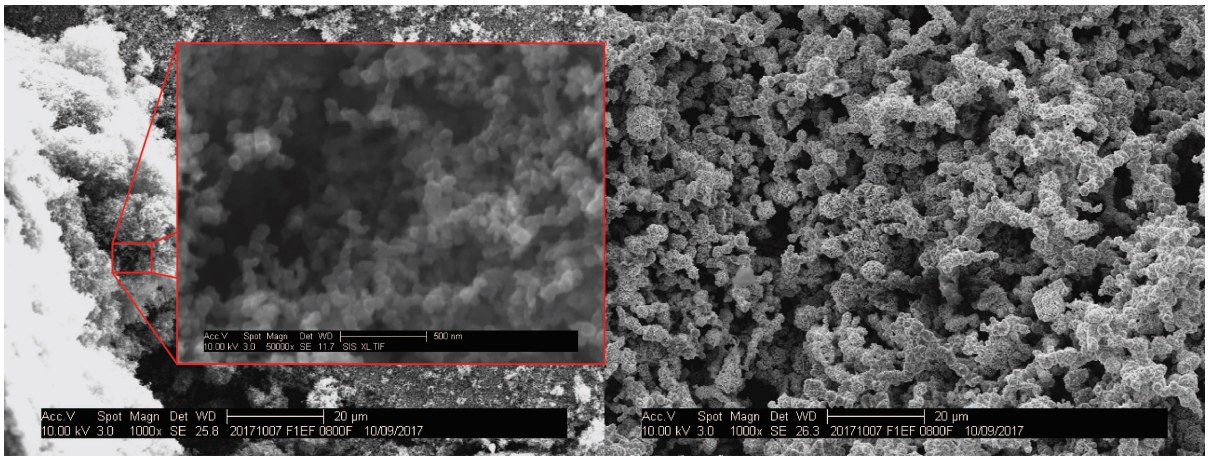

Figure 2-11: SEM image of filamentary fillers Carbon Black and Nickel Powder (from left to right). The Carbon Black image shows 1,000X with a portion magnified to 50,000X while the nickel powder was magnified to 1000X. The particles have a similar shape, but scale is very different.

copper powder was significantly different from all of the others and was classified as a dendritic particle nickel powder and is shown in Figure 2-13.

The particle surface area and general shape of the particles were both found to be significant in the NCPF response. A linear regression alysis determined there is a positive linear correlation between additive surface area and voltage response. With each square meter increase in surface area there was a 0.003 V increase in peak voltage with a p-value of 0.0003. Furthermore, cylindrical paricles as described above were found to produce a 16% higher peak voltage than the cylindrical particles (p-value = 0.0027). Flake and filamentary powders showed no statistical difference to either cylindrical or dendritic particles. These findings support the triboelectric hypothesis in that particles with larger surface areas and geometry that incourages motion generate larger triboelectirc charges.

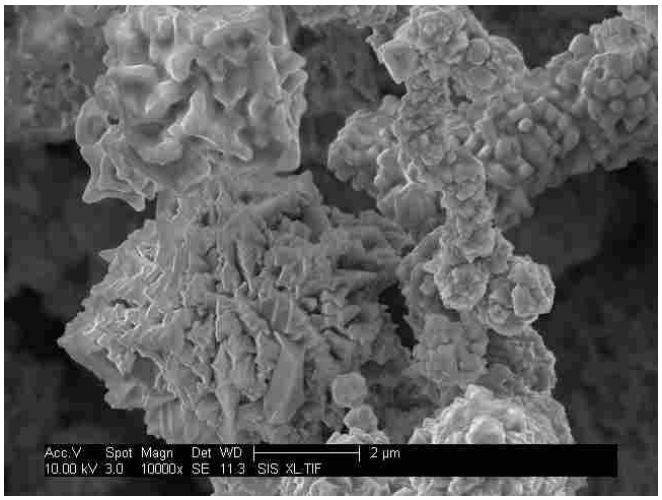

Figure 2-13: Nickel powder has a very low contact surface area resulting in higher contact resistance between conductive elements.

2.4.1.2 Void Size

A multiple linear regression analysis was used to determine if there was a correlation between void size and additive type between samples. Significant covariates in the model included additive type, additive loading level, and calculated surface area. The analysis demonstrated a statistically significant difference between additive types when loading level and surface area are held constant (alpha ≤ 0.05). The average differences in void size between additive types while controlling for additive loading and surface area, can be found in Figure 2-14. Carbon black was found to have the smallest voids followed in order by MWCNTS, milled carbon fiber, F104, copper powder, nickel powder, P103, and M103.

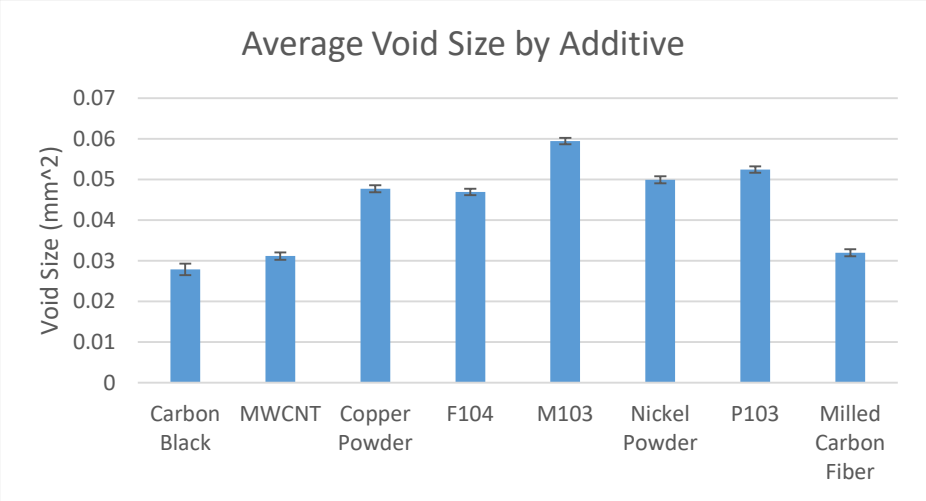

Figure 2-14: Bar plot showing the average differences in void size with respect to Additive type. The error bars represent the standard error of all voids measured.

The effects different additives have on nucleation within foam is a very specific research area which is beyond the scope of this paper. However, it is apparent that in these foam samples, the additives contribute to void size with significant difference found between additives. The bulk resistance analysis below demonstrates that increased void size has a negative effect on the NCPF response. Void size is shown to have a negative correlation with the bulk resistance of the

material, larger voids increase resistance. As the bulk resistance of the material increases the overall magnitude of electric response decreases as well.

2.4.1.3 Bulk Resistance

Two separate evaluations were completed on the resistance measurements: a secondary additive effect, and a primary additive effect. The data with and without fiber was initially evaluated to determine to what level the fiber contributed to the bulk resistance of each sample. Figure 2-15 demonstrates how the secondary filler contributed to a reduction in resistance between each primary additive. With each additive, we see some reduction in resistance with the addition of the secondary fiber filler. The secondary fiber reduced resistance the most in with the larger particles because they are not dispersed as well throughout the NCPF. The secondary fiber filler provides a way of connecting the individual clusters of particles, enabling more paths for the charge to follow. The MWCNTs offer a large aspect ratio and are very low density enabling them to create a well-dispersed network throughout the NCPF with or without the fiber. Nickel powder, on the other hand, has a much larger particle size and a smaller aspect ratio and benefits the most from the electrical branching between particles. The secondary fiber produced a significant benefit to all additives, strengthening the evidence that it is a necessary addition to the NCPF sensors.

Evaluation of the resistance data by additive demonstrates a large range of electrical properties between each additive. A multiple regression model was created to determine the NCPF variables that contributed to the bulk resistance of the foam. The variables considered for this model included: additive type, average sample thickness (the variation in cut sample size), calculated primary additive surface area, mean void size, and loading level. A cut off criteria for

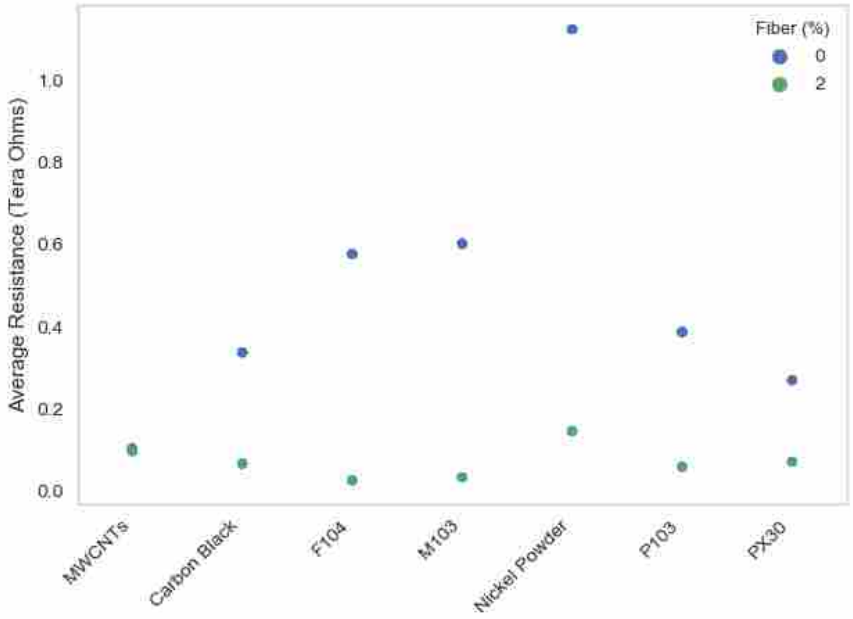

Figure 2-15: This plot demonstrates the difference in Average Resistance between NCPF one sample with and one without NCCF secondary filler.

model variables was based on an alpha value of ≤ 0.05. The resultant model demonstrated that there is a significant difference between the bulk resistance of the samples due to primary additive types, the total surface area of the additive, mean void size of the foam structure, and additive loading level. A plot demonstrating the differences in bulk resistance between additives while controlling for surface area, void sizes and loading level can be found in Figure 2-16.

It is interesting to note that the nickel powder samples were much less conductive than all the other samples. We propose that the disparity is caused by the additive's geometry. The surface of the nickel powder is very rough when compared to the other additives, reducing the contact surface area and increasing the contact resistance between itself and the secondary filler (Figure 2-13). This conclusion is supported by the negative correlation between calculated additive surface area and conductance. If all other variables were kept constant and additive

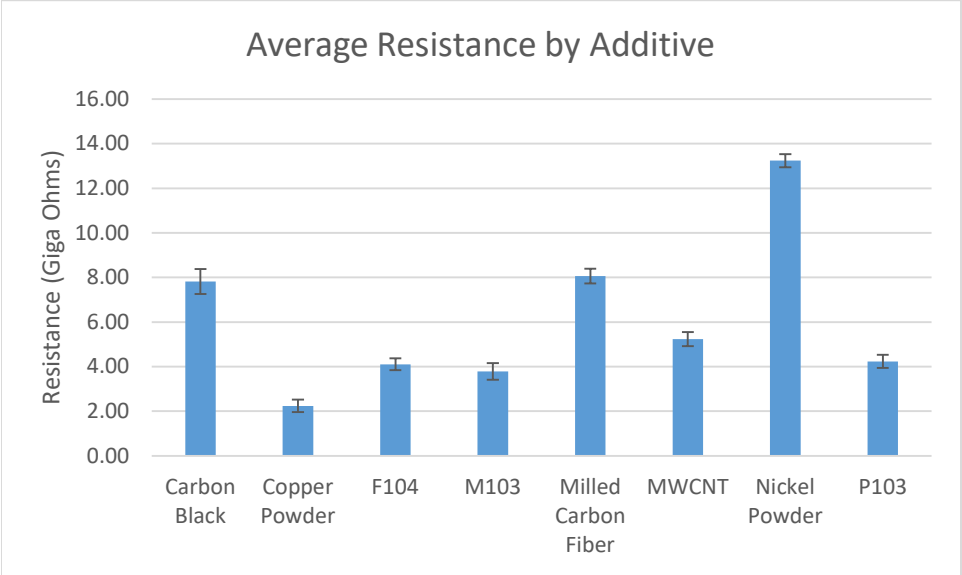

Figure 2-16: Average bulk resistance of each additive while controlling for additive level, calculated surface area and void size. The error bars represent the standard deviation in measured resistance with each sample.

surface area were increased, one would expect to see a decrease in resistance. Copper has approximately the same density as nickel, but the powder has a much smoother surface and higher aspect ratio making it the most efficient in reducing the resistance of all additives. Additionally, larger voids were found to have a negative correlation to resistance: with all else held constant, as the voids increased in size the resistance increased, on average.

2.4.1.4 Additive Selection

A piecewise approach was taken while evaluating the differences in measured peak voltage between additives. Initially, all additives are evaluated against each other in one large model, which accounts for effects found throughout all evaluated materials. The model is then broken up into subsets of additives of similar base material to provide insight into the triboelectric generation, which is a function of the interactive surface area. Lastly, we evaluate each additive individually to highlight trends found in relation to loading levels.

Combined Charge Generation Model

The combined linear regression analysis evaluated which variables were statistically significant throughout all additives; the understanding of which will provide insight into further optimization of the NCPF sensors. The following variables were considered in the model: additive type, loading level, calculated additive surface area, geometry, void size, and average resistance. Void size, additive type, and loading level were eliminated from the combined regression model based on an alpha greater than 0.05. However, void size is indirectly accounted for in the model through the material resistance as described earlier.

The resultant regression analysis demonstrates that higher additive surface area, lower resistance, and higher impact energy account for larger NCPF response. The estimated effects of each additive is shown in Table 2-3. All particle geometries are compared to the cylindrical particles and only Dendritic particles are found to be significant, with a lower response. There was no statistical difference between the cylindrical, filamentary and flaked particles.

Table 2-3: Combined electrical model parameter estimates.

Term	Estimate	P-value
Intercept	1.262944	<.0001
Additive surface area (m^2)	0.002935	0.0004
Impact Energy (J)	0.027779	<.0001
Bulk Resistance (TΩ)	-2.90	<.0001
Geometry[Dendritic]	-0.10379	0.0031
Geometry[Filamentary]	-0.04412	0.2346
Geometry[Flaked]	0.021304	0.3042

Additive Subset Models

The proposed theory behind the NCPF is that the additive surface interacts with the polymer matrix when impacted through a triboelectric effect. The magnitude of the triboelectric response is dependent upon both material's triboelectric affinity and the interactive surface area. Additives in this study were selected to represent specific base materials with varying surface areas. For example, carbon black, MWCNTs, milled carbon fiber, P103, M103, and F104 are all carbon-based with a large range of specific surface areas. Likewise, nickel and copper powder are both metal-based additives with different geometries. However, the carbon-based additives could be further separated into natural and manmade additives.

Two analyses were carried out to determine if additives there are stronger performance characteristics associated within subsets of the additives. One such grouping was carbon-based, and non-carbon-based additives. Within the carbon-based additives there was a potential separation into natural and manmade categories. The carbon/non-carbon group was evaluated while accounting for loading level, resistance, impact energy, and impact number. The additive base material was found to be statistically significant, demonstrating that the base material is important in the triboelectric model. The carbon-based materials on average produced a larger response than the metal-based additives. This is consistent with the hypothesized triboelectric effect as carbon-based materials have a larger difference in triboelectric affinity than the metals, providing a greater potential to create a charge (Table 2-1).

Furthermore, the performance of natural vs manmade carbon particles was evaluated while controlling for impact energy, resistance, impact number, additive level, and void size. The difference between natural and manmade additives was found to be statistically significant with the manmade additives contributing to a 10% larger response on average. We propose that the

larger response is attributed to the higher conductivity of the manmade additives due to their higher carbon / lower impurity content.

Additive Charge Generation Analysis

Based upon the statistical analysis of additive performance, an optimization exercise was undertaken. Performance criteria were based upon maximizing both signal-to-noise ratio and peak voltage response. Each of the eight additive types were evaluated individually for three different additive loading levels, resulting in 24 data points.

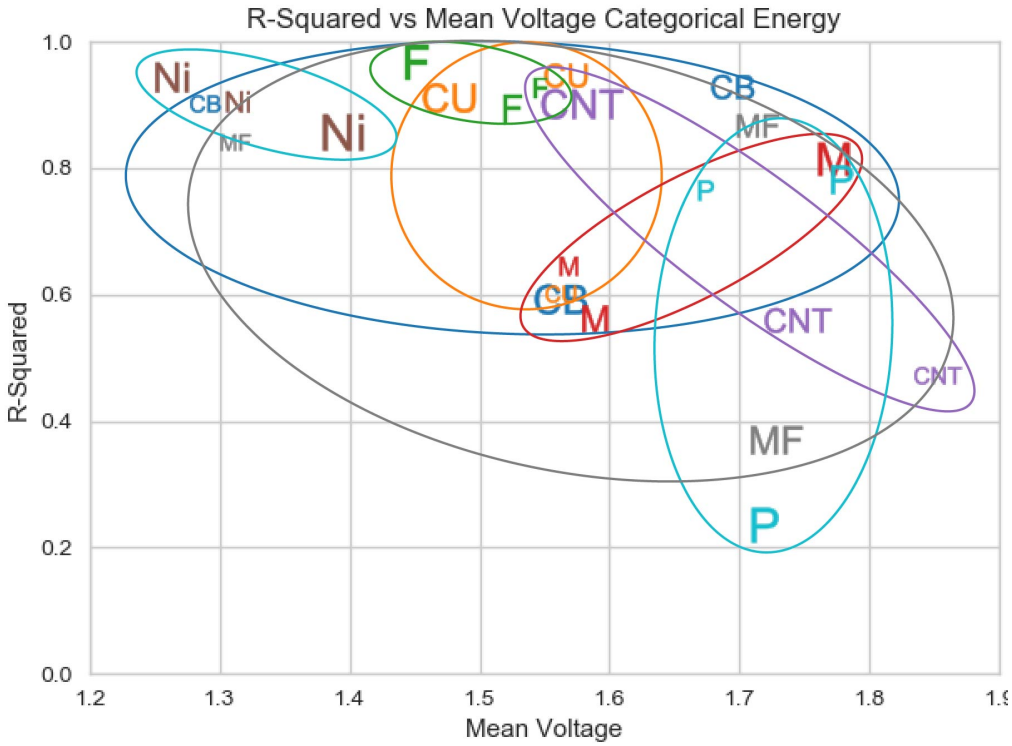

Figure 2-17: Plot showing R squared vs Mean Peak Voltage for each primary additive with impact energy as categorical. The different loading levels are represented by different sizes while each additive is represented by a shortened name as follows: CB – Carbon Black, CU – Copper Powder, F – F104 Graphite, M – M103 Graphite, CNT – MWCNTs, Ni – Nickel Powder, P – P103 Graphite, MF – Milled Carbon Fiber.

Impact energy can be correlated with NCPF response in either a continuous or categorical manner dependent upon the nature of the response. If there is a linear correlation between impact energy and NCPF response, then a linear model is the logical approach. However, if there are non-linearities between NCPF response and impact energy a categorical correlation would create better results. For the purpose of this paper we will evaluate both. The ideal material would be in the upper righthand corner of the R-squared (signal-noise-ratio metric) vs voltage plot, producing high mean voltage and a strong correlation between impact energy and voltage.

The average voltage and R squared were calculated for each additive and loading level, which were plotted against each other for the categorical (Figure 2-17) and continuous energy (Figure 2-18) inputs. As one can see, the categorical model has higher R-squared correlations in general throughout all additives when compared to the continuous energy model. Additionally, the additives seem to have a tradeoff with respect to Mean Peak Voltage: as the peak voltage increases, there is generally a decrease in R squared. The additives at all three loading levels are grouped by an ellipse to demonstrate how consistent they are with respect to loading within each additive type. Materials with larger spread between loading levels are less desirable as their signal is susceptible to slight variations in manufacture. Ultimately, these plots can be used to determine which additive and what loading level should be selected for a desired accuracy and response level. If a linear correlation were desired and peak voltage magnitude wasn't as critical as accuracy, then nickel powder or F104 graphite would be the best options.

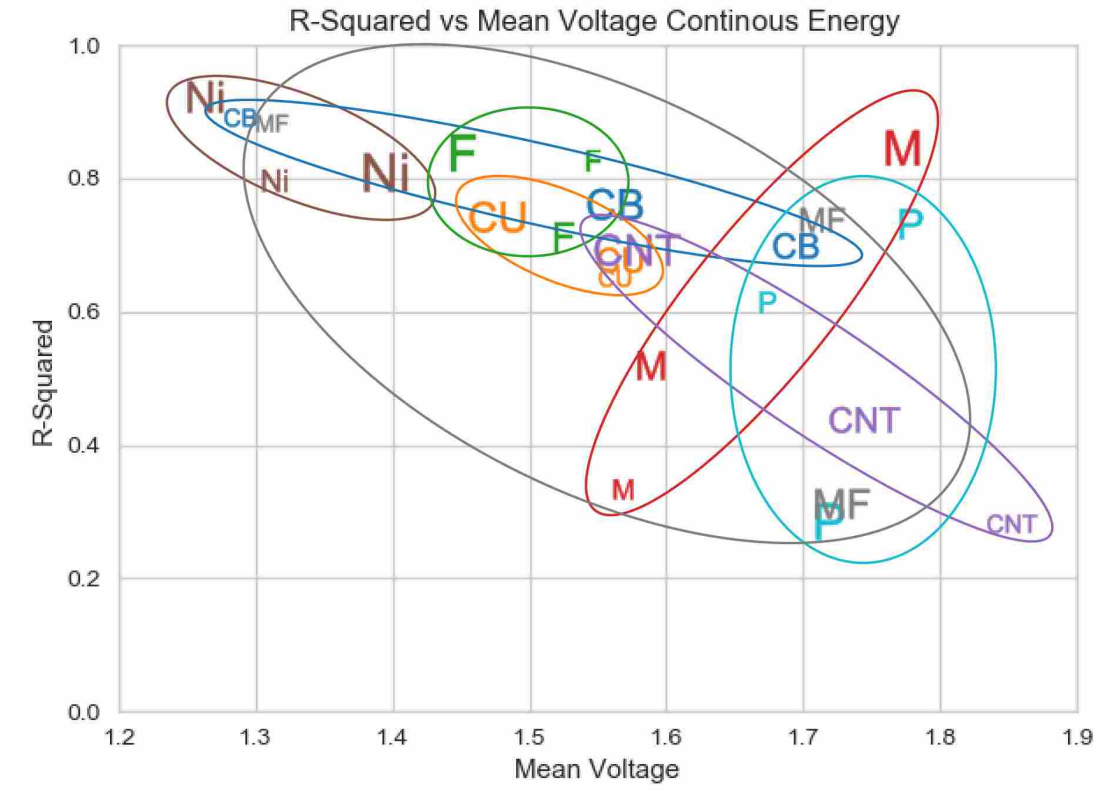

Figure 2-18: Plot showing R squared vs Mean Peak Voltage for each primary additive with impact energy as continuous. The different loading levels are represented by different sizes while each additive is represented by a shortened name as follows: CB – Carbon Black, CU – Copper Powder, F – F104 Graphite, M – M103 Graphite, CNT – MWCNTs, Ni – Nickel Powder, P – P103 Graphite, MF – Milled Carbon Fiber.

2.4.1.5 Conductor Generation vs Foam Generation

Two samples of foam, one NCPF and the other Neat, were evaluated with varying conductive wire probes connected to an NI-9229 analog voltage measuring device. The NI-9229 device was selected due to its high internal impedance and large voltage range. Each foam sample was impacted by the modified Dynatup drop tester previously described. Initially, all wire probes were connected to the voltage measuring device and in each subsequent test, a random wire was removed until no wires were connected. This process was repeated twice for

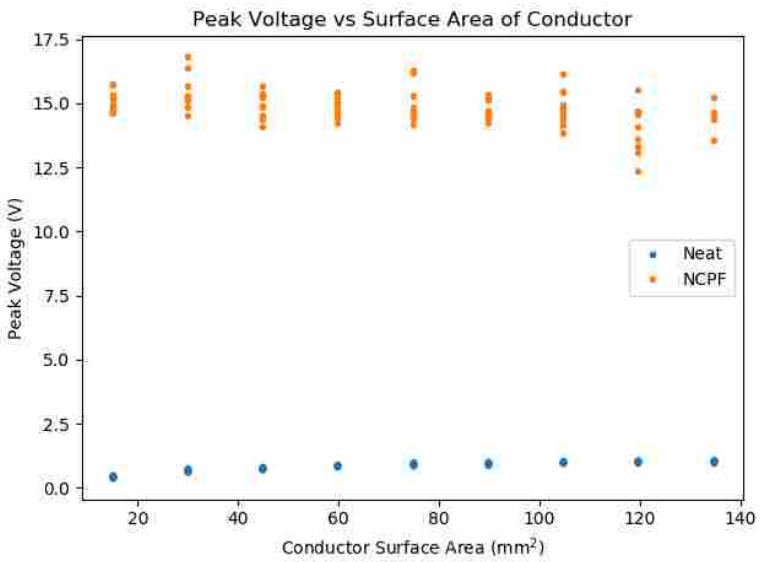

Figure 2-19: Peak voltage response from Neat and NCPF foam vs surface area of the wire used to measure the response.

each sample. The voltage response was recorded, and all data were evaluated to determine the peak voltage response for each impact. Peak voltage from each test is shown in Figure 2-19 where the NCPF foam is shown in orange and the Neat or standard foam is shown in blue. The NCPF foam shows little to no dependence on the surface area of the conductor and immediately jumps to a max voltage that is constant throughout all tests. The Neat foam, however, shows a logarithmic correlation to the surface area (Figure 2-20). An exponential curve, fit the data with $R^2 = .97$ with the following equation:

$$y = a + be^{-cx} \tag{2-5}$$

where a = 1.072, b = -0.998, c = 0.029 and x is the surface area of the wire.

These tests demonstrate two important characteristics of the NCPF sensors: the composite additives create a massive triboelectric effect within the material when compared to Neat foam,

and the NCPF response isn't dependent upon conductor surface area. As can be observed in Figure 2-19 the NCPF sensor response is independent of how many wires are attached to the DAQ, indicating a week correlation between conductor surface area and sensor voltage. Clearly the majority of the response results from triboelectric effects within the foam, and not between the foam and the conductor; the maximum probe effect in the neat foam experiment accounts for only 6% of the max signal in the NCPF samples.

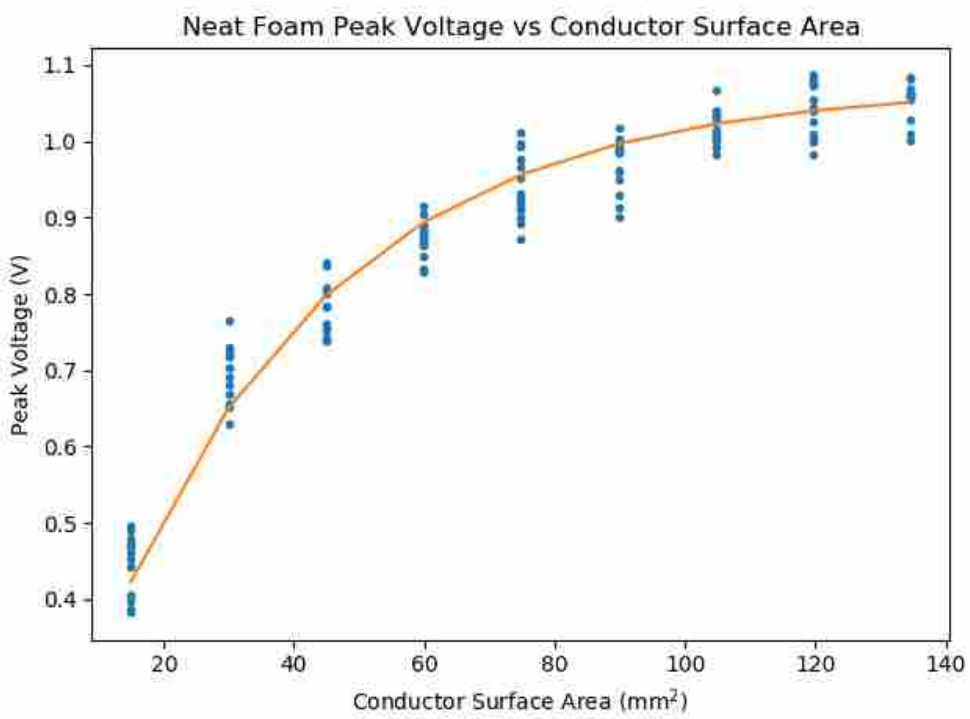

Figure 2-20: Peak voltage response vs conductor surface area with curve fit using exponential curve.

2.4.2 Extrinsic Considerations

2.4.2.1 Digital Signal Acquisition Device Characteristics

The input impedance of each DAQ tested is shown in Table 2-4, these values can be used as a reference when selecting a system to measure the NCPF. The table also lists the values of the capacitors and resistors which were added to the National Instrument devices to match the NI-9234 DAQ. One can see that each device provides a unique combination of input resistance and capacitance resulting in a wide range of input impedances. The NI-9215 had an initial input resistance that was too high for the custom circuit to measure without becoming unbalanced, so a 10 MΩ resistor was placed in parallel between the leads to reduce its input resistance to a lower level.

To reduce possible differences in electrical conditions while testing, three separate National Instrument DAQs (NI-9234, NI-9229 and NI-9215) were used for all voltage tests. These three devices interface with computer through the same MDAQ chassis and used the same

Table 2-4: Input impedance of several tested DAQs. All DAQs were tested in the circuit shown in Figure 2-5.

DAQ	Input Resistance (M Ohm)	Input Capacitance (pF)	R1 (k Ohm)	Added Capacitor (pF)	Added Resistor (M Ohm)
NI-9234	0.304	126.05	237.50	NA	NA
NI-9229	1.028	96.35	508.00	NA	NA
NI-9229 Matched	0.305	125.62	237.50	25.00	0.450
NI-9215	24.855	108.46	946.00	NA	10.00
NI-9215 Matched	0.307	122.02	237.50	10.00	10.317
Fluke 87 V	12.889	36.02	928.00	NA	NA
Xonano Board	0.748	21.64	428.00	NA	NA
Arduino Uno	1.475	20.17	596.00	NA	NA
Analog Discovery	0.305	36.50	488.00	NA	NA

probes to connect to the foam sample. Each DAQ was individually tested by connecting to the same NCPF sample, impacted with the same impact mass, and dropped from the same height with their unmatched impedance. The voltage response from each device is shown in Figure 2-21, showing the dramatic differences in measured response dependent upon the DAQ's input impedance. The change in measured response is linearly correlated to the DAQ's input resistance with a R-squared of 0.96. With each increase of 1 MΩ in input resistance there is an increase of 0.35 measured voltage for the same impact. This correlation allows us to scale the measured response with the input resistance of the DAQ and correlate signals between different DAQs. These tests were limited to input resistance of 305 k to 24.85 MΩ and we don't expect the voltage to increase forever but this range of input impedance covers a large portion of possible DAQs.

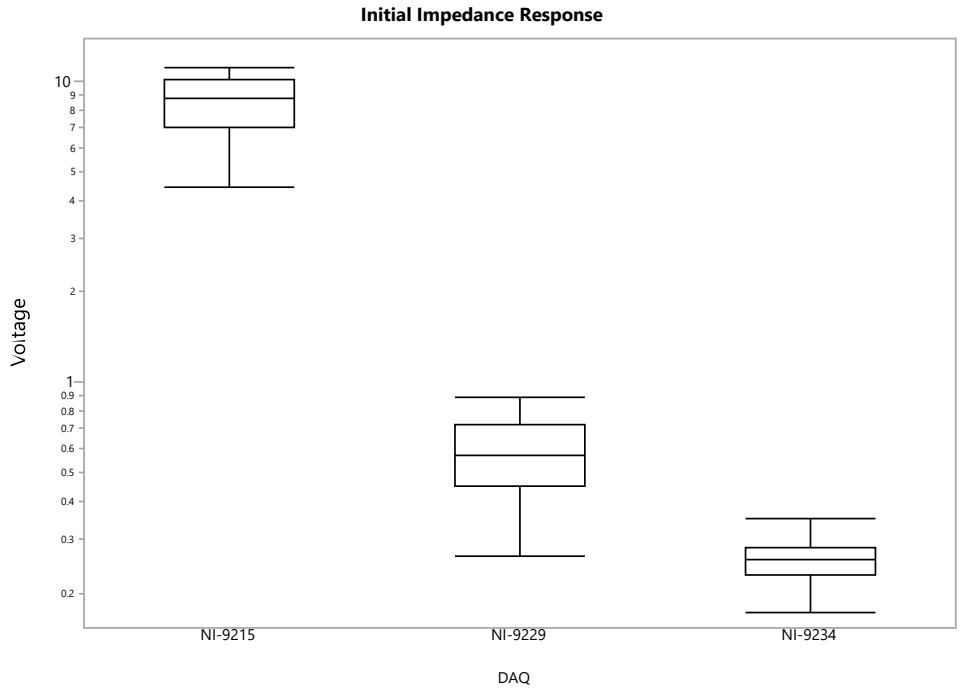

Figure 2-21: These box plots demonstrate the vast difference between voltage measurements when using DAQs with different input impedances.

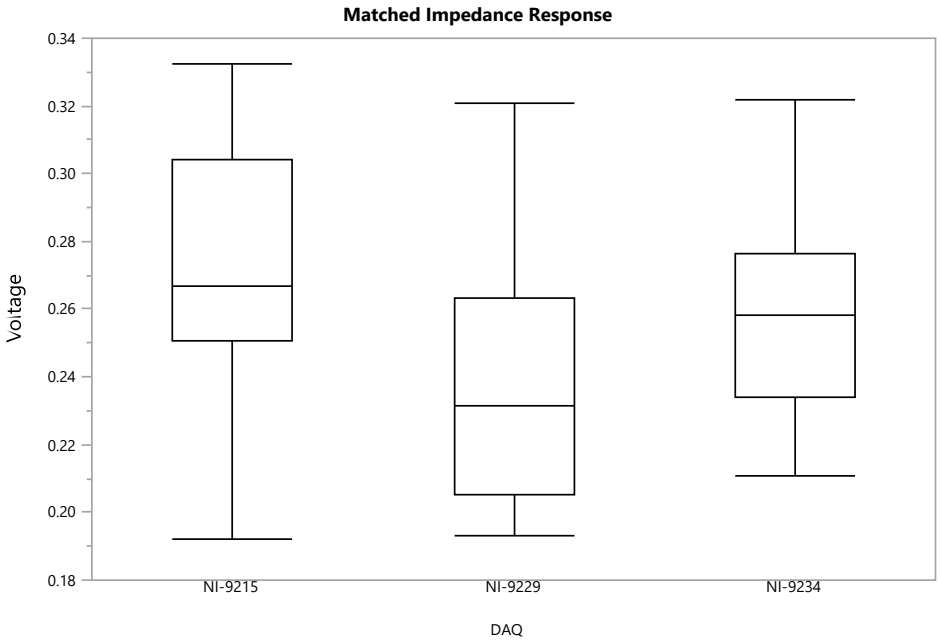

Figure 2-22: Box plots showing voltage recorded with input impedance matched between all three National Instrument DAQs.

To validate the proposed relationship between response voltage and device internal impedance, the input impedance of the NI-9229 and NI-9215 DAQs were adjusted to match that of the NI-9234. A 450 kΩ resistor and 25 pF capacitor were added in parallel to the ground and the measurement lead on the NI-9229, resulting in an internal impedance of 305 kΩ and 126 pF. As previously mentioned the NI-9215 device required a 10 MΩ resistor to move the impedance into the range that was measurable for our system and was tested as such for the data provided in . An additional 317 kΩ resistor and a 10 pF capacitor were added in parallel with the NI-9215 leads resulting in an internal impedance of 307 kΩ and 122 pF. All three DAQs, with approximately the same internal impedance, were connected to the NCPF sensor impacted and the resultant peak voltage was recorded. The resultant voltage responses, as demonstrated in Figure 2-22, show no statistical differences between all three DAQs (alpha ≤ 0.05). These results are very encouraging and demonstrate great correlation between DAQs that reference a constant

ground. These data further demonstrate how the NCPF response can be tailored to different applications by adjusting the input impedance of DAQs or selecting a DAQ based on its input impedance. However, other considerations must be given to devices that have floating grounds (microcontrollers) or use active feedback to adjust for external loads.

With a known input impedance, one can determine the charge generated by the NCPF using Equation 2-4. The peak voltage generated from the previously described 30.78 J impact was used to demonstrate the peak charge the NCPF sensors can generate and is shown in Figure 2-23. Increased impact energy or different NCPF characteristics would change the output. The peak charge for this single sensor produced anywhere from 20 to 45 pC which, at peak output, would create 20 to 40 pA. Modern energy efficient microcontroller systems operate in the low nA range and newer iterations are further reducing power requirements. There is potential for

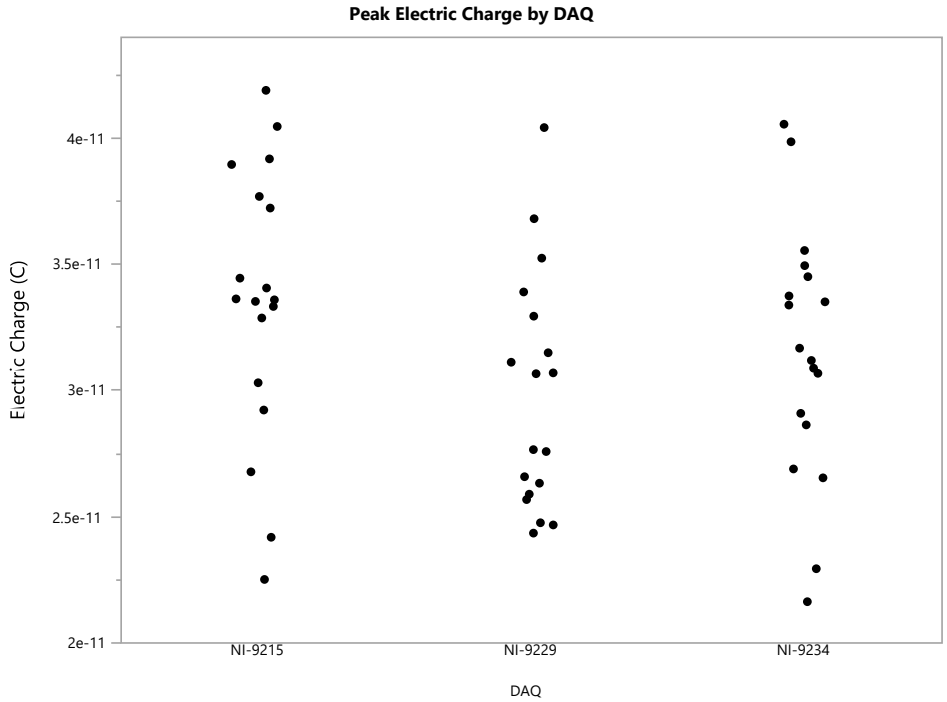

Figure 2-23: Peak electric charge generated for all impacts on the matched National Instrument DAQs.

these sensors to subsidize or eventually fully power such a microcontroller, creating a truly self-powered sensing system.

2.4.3 Environmental

The main environmental variables that are likely to affect performance of NCPF sensors in typical applications include humidity and temperature. In order to allow design engineers to either compensate for these variable, or eliminate the effects, studies of the relationship between these environmental factors and sensor performance are outlined below.

2.4.3.1 Humidity

Evaluation of the humidity test data shows that there is a strong correlation between the ambient humidity and the NCPF peak voltage. Figure 2-24 demonstrates the peak voltage response from four levels of humidity with respect to time showing the decrease in voltage with increased humidity. As the humidity increases within the low impact system described the peak voltage decreases in a linear manner between 35 and 63 %RH, levels greater than 64 %RH results in a constant peak voltage. This relationship is demonstrated by:

$$\begin{aligned} 35 \leq \%RH < 63 \qquad & \frac{average\ peak\ voltage}{impact} = -0.01 * (\%RH) + 0.63 \\ \%RH \geq 63 \qquad & \frac{average\ peak\ voltage}{impact} = 0.03 \end{aligned} \tag{2-6}$$

The results of all humidity tests and the proposed model are shown in Figure 2-25. While the voltage from the tests decreased significantly above 63%RH the signal was still clean enough to discern each impact due to the large signal to noise ratio.

It is well documented that humidity disrupts the triboelectric transfer of charge between materials [43, 49]. It is proposed that the decrease observed in peak voltage is due to a disruption in the triboelectric effect between the conductive additives and the foam matrix. The additives lose their efficiency in generating the charge and propagating it to the conductor until the point in which they no longer contribute to the response (63%RH). We propose that when the humidity exceeds 63%, the voltage response only comes from the triboelectric generation between the electrical probe and the NCPF. As demonstrated previously there is a smaller triboelectric charge that is generated between the NCPF and the electrode used to measure it. This triboelectric response accounts for approximately 6% of the signal in a dry environment with a sufficient

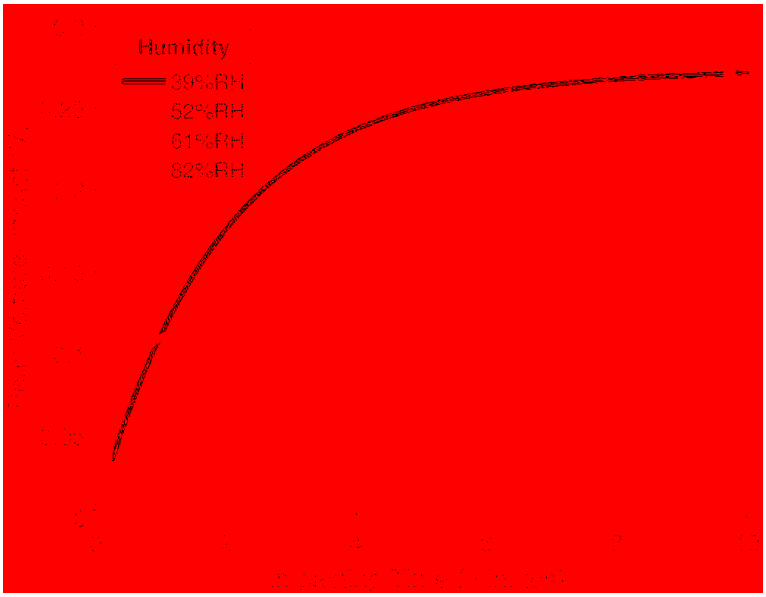

Figure 2-24: This plot demonstrates the influence of relative humidity on peak voltage over time from several levels of the humidity tests.

surface area in the experiment outlined. The voltage response above 63%RH is approximately 10% of the signal captured at ambient humidity demonstrating approximately the same fraction of the signal. The NCPF samples used in this analysis were made with a conductive film as opposed to the wires used in the previous tests, resulting in a higher conductor-to-foam ratio and a higher contribution to the signal. Another potential explanation for the drift associated with the increased humidity is a change in mechanical properties. Humidity is known to cause a change in mechanical properties in viscoelastic polymers [50, 51], however, it softens the material (by 0.8%/%RH) [52, 53]. The low impact energy associated with these tests results in minimal strain (< 5%) which maintained consistent throughout all the testing regardless of humidity. The lack of quantifiable change in material properties is most likely due to the very small strain; if the

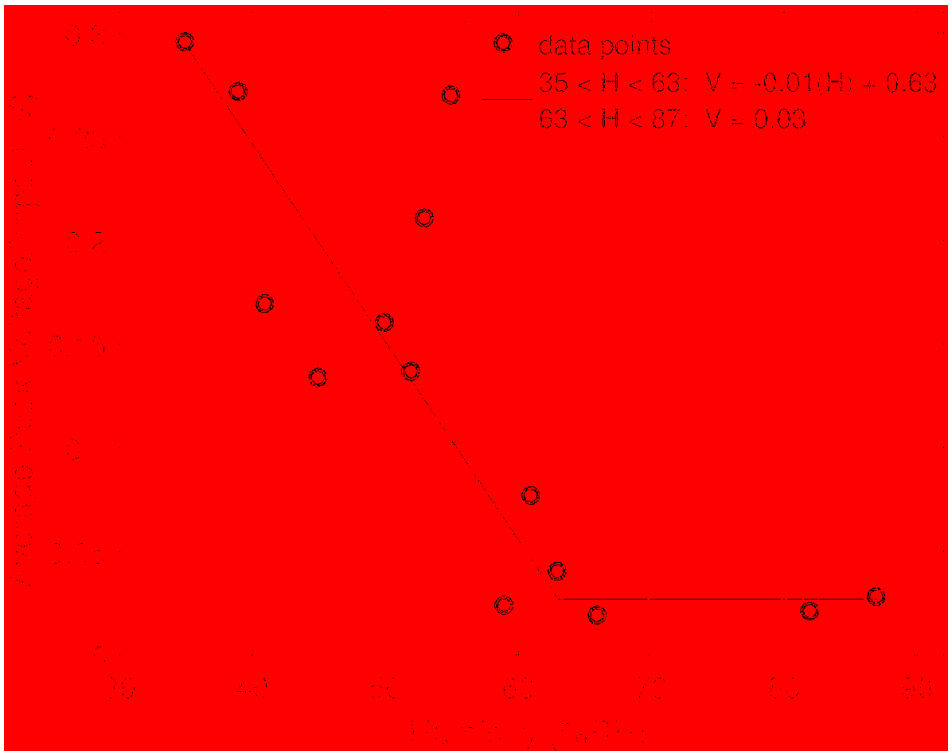

Figure 2-25: The influence of humidity on peak voltage is demonstrated for all tested humidity levels with the proposed piecewise function shown.

strain were more significant it is possible the humidity would affect these properties. If the foam matrix were to soften, it would have an opposite effect on the voltage as increased strain and strain rate increase the peak voltage. Future tests will evaluate humidity effects with higher strains.

2.4.3.2 Temperature

A positive linear effect on peak voltage was discovered for small impact energies with thin NCPF samples with relation to temperature (Figure 2-26). This temperature dependence as outlined in Eq. 2-7 has a positive linear correlation of 13.5 mV/°C when normalized to 35%RH over the temperature range tested.

$$21.5 \leq T \leq 31°C \quad \frac{average\ peak\ voltage}{impact}(normalized\ to\ 35\%RH) = 0.0135(T) + 0.12 \qquad (2\text{-}7)$$

Most of the drift is attributed to the softening effect of the viscoelastic base material, with increased temperature. It is well documented that increasing the temperature of a viscoelastic polymer decreases its stiffness [50, 54]; Young's moduli of similar polyurethanes have been shown to linearly decrease by as much as 3%/°C in this temperature range [55, 56]. Considering that strain is proportional to stiffness/ in the linear elastic region (for a set amount of absorbed energy) and there is an approximately linear relationship between strain and voltage in these sensors [57-59], this can theoretically induce a voltage sensitivity of 2.12%/°C.

This higher strain increases triboelectric rubbing (by engaging more fiber/matrix contact sites and forcing more friction at each site) and the conductivity of the network that transports the resultant voltage to the measurement probe. On top of this mechanical effect, the signal's response to temperature may be partially attributed to an electrical mechanism. Multiple sources have reported increased triboelectric charge accumulation and retention in various materials as

they are brought to higher temperatures [60, 61]. While the exact relationship between temperature and triboelectric efficiency is highly material and application-specific, it is known that the operative mechanism is the change in relative permittivity [60]; this permittivity increases in the presence of higher temperatures, which will strengthen the sensor's electric field and raise its steady-state peak voltage signal (though strain may be held constant).

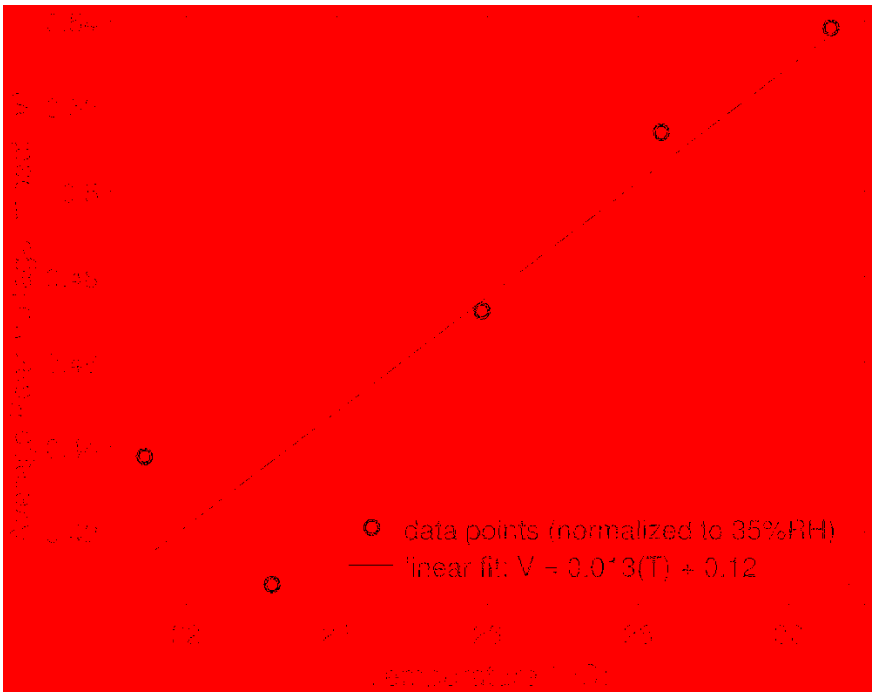

Figure 2-26: Positive linear influence (R^2=0.871) of temperature on an NCPF sensor's average steady-state peak voltage per impact. This data was normalized to 35%RH (using Eq. 1) to isolate the temperature effect from humidity-related drift.

2.5 Discussion

The purpose of this paper was to evaluate how additives and external influences affect the NCPF's measured electrical response to deformation. The understanding of which provides a better understand the internal physics behind the electrical response while providing suggested

recipes for more accurate sensors. The intrinsic, extrinsic and environmental variables were each closely evaluated for evidence supporting the triboelectric hypothesis. Intrinsic characteristics focused on the primary additive which is attributed to the internal triboelectric generation with the polyurethane foam. Carbon and metal-based additives were selected based on their diversity of geometries and surface topologies. Through BET analysis and SEM imaging, the additive's physical characteristics were quantified and used as explanatory variables in observed measures of the NCPF's performance. Some measures of the foam, namely void size, are used to control for any manufacturing variance that occurred through hand making the samples. Others, such as the bulk resistance and peak voltage output are directly attributed to the differences in the additive's physical and material properties or the by the signal is collected. External factors that can possibly affect the performance of the NCPF sensors were categorized into extrinsic or environmental effect and were likewise evaluated. How the digital signal acquisition device evaluates the voltage is dependent upon its internal impedance. Furthermore, as the temperature and humidity change so do the material and electrical properties of the NCPF. With all the above-described evaluations a phenomenological model is developed.

Special care was taken during manufacture of the NCPF to maintain constant physical characteristics, such as density and homogeneity, so comparison of the primary additives would be significant. Evaluation of each sensor revealed that most all variance in void sizes was due to additive effects on the foam as it was rising. These effects are attributed to the size and geometry of the particles by means of increasing nucleation points for the foam. NCPF samples made with carbon black and MWCNTs were found to have the smallest voids with almost half the size voids as M103 graphite. The NCPF void size, because of its statistical significance, was then used in subsequent models. A commercially manufactured foam can have the void size adjusted

to a wide range of sizes to customize the material properties of the foam and isn't dependent upon additives. By using void size in all models, this information can be used to dictate the optimized void sizes in manufacturing.

Bulk resistance of the NCPF is expected to increase the overall performance of the sensor by creating a network by which the generated charge can make its way to the measurement probes. Previous composite sensor development indicated that a secondary, electrically conductive, fiber filler could increase the electrical performance of the sensors. This theory was evaluated by including control samples, which had no secondary filler with the same primary filler loading. Comparison of the control samples to the standard samples demonstrated a lower resistance in all additives. Some additives benefited more than others depending on the dispersion and geometry of the particles. Low density and high aspect ratio particles benefitted less than their denser and shorter counterparts for the most part. Nickel powder benefited the most from the inclusion of fiber as the geometry of the particles prohibited efficient conductivity without longer fibers bridging the gaps between particle clusters. Further differences were also observed between additives when the secondary additive was held constant, copper provided the most conductive samples, nickel producing the least, and larger voids correlated with lower resistance. This material property like void size is considered in all subsequent models.

The primary focus of this paper was evaluating how each additive contributed to the electrical voltage generation within the NCPF sensors. The additives were evaluated in a combined model to determine which variables were statistically significant between all additives. Higher additive surface area, lower resistance, higher impact energy and higher impact number were correlated to higher voltage outputs. All additives were not significantly different from each other, but additive type was significant. Additional tests demonstrated that the additives could be

grouped into carbon-based and metal-based subgroups. The carbon-based additives created on average a larger peak voltage response than the metal-based additives which supports the hypothesis that voltage is dependent upon triboelectric affinity separation. Carbon-based materials are more prone to positive charge and more freely give up electrons to the polyurethane matrix, resulting in a larger response. The carbon-based additives could be further separated into natural or manmade categories with statistical significance. This difference is proposed to be caused by the difference in carbon content between them. The manmade or higher purity additives contributed to an increased electrical response. Ultimately, a selection matrix was created, demonstrating the R squared correlation coefficient for each additive vs mean peak voltage. This matrix can be used in additive selection and demonstrates the wide range of electrical properties each additive provides. By our selection criteria, we found nickel powder and F104 graphite to provide the best results. nickel powder consistently provided strong correlation, but had a lower mean voltage, while, F104 had a strong correlation with a higher mean voltage.

Other factors which were found to affect the measured response include the electrical probe, the digital acquisition device used to measure the system, and the environmental conditions (temperature and humidity). The electrical probe used to measure the NCPF response was found to contribute to the signal on a very small scale. Neat foam samples which had electrical probes embedded inside them saw a positive correlation between the voltage generated and increased probe surface area. NCPF samples with the same configuration generated a voltage that was an order of magnitude greater than the Neat foam which had zero correlation to probe surface area. Multiple DAQ systems were evaluated and each device was evaluated for its internal impedance. The DAQs evaluated represented a wide range of input impedances and

demonstrated the large disparity in measurements with the same input. A strong correlation between input capacitance and peak voltage was observed. These observations provide evidence that proper evaluation of different DAQs can lead to direct comparison between devices. The humidity and temperature both affected the electrical response of the sensors. Increased humidity decreases the NCPF response by disrupting the triboelectric transfer of charge between the embedded additives and the polyurethane foam. Temperature had the opposite effect with a positive between temperature and peak voltage. This correlation is attributed to the softening of the viscoelastic foam matrix which allows for a larger amount of internal motion for the same impact energy.

Through evaluation of multiple additives and loadings, F104 graphite and nickel powder were shown to provide the most accurate and repeatable electrical response to impacts. Their electrical response was consistent throughout all levels of loading regardless of the model (categorical or continuous). Furthermore, the data seem to support the internal triboelectric generation theory behind the NCPF response, which relies on the affinity of each material and the surface area of contact. Future work will be focused on the dual sensing ability to increase their utility as consumer and research measurement devices.

2.6 Acknowledgements

This material and research are based upon work supported by the National Science Foundation under grant numbers CMMI-1235365 and CMMI-1538447.

3 SPATIAL DETECTION OF IMPACT WITH PIEZORESPONSIVE NANO COMPOSITE FOAM

3.1 Abstract

With the continual progress of wearable devices, prosthetics, and robotics, multifunctional materials that integrate sensing capabilities with a tailored mechanical response have found wide market application. This study evaluates the potential for a previously developed multifunctional material (Nano Composite Piezoresponsive Foam or NCPF) to simultaneously measure both impact magnitudes, as well as spatial detection of impact location within a single sensor. NCPF exhibits non-linear, rate-dependent mechanical properties. Furthermore, the internal triboelectric generation can be altered by NCPF geometry, impact material, and the electrical circuit used to measure the response. In the present work, the material and electrical characteristics of the system are measured and subsequently used to tune a system, which was able to provide accurate spatial location information along the length of an NCPF sensor.

3.2 Introduction

Extensive research has been dedicated to the field of multifunctional materials, resulting in many different types of sensors that can be designed directly into systems or products [38, 62-73]. This paper evaluates the capability of a specific multifunctional material, Nano Composite Piezoresponsive Foam (NCPF) [23], to measure both the magnitude and spatial location of impacts. NCPF sensors are created by adding a mixture of nickel powder and nickel coated carbon fiber to the liquid components of a polyurethane foam before casting. The foam is cast on, or around, conductive elements which measure the foam's voltage response. The NCPF

voltage response is generated by a triboelectric effect between the composite additives (nickel and carbon), and the polyurethane foam matrix.

NCPF sensors have been used in systems ranging from football helmets for impact detection, to bushings for vibration monitoring, and shoes for gait analysis [14-16]. Analysis of the material performance in these applications has shown relationships between voltage response and acceleration, impact energy, frequency, and magnitude of solitary and vibrational impacts. These systems used discrete sensors to determine locational information. In various applications where the detailed spatial characterization of impact is required, it is more convenient to cast a single foam component and extract spatial data via the probe circuitry rather than using discrete sensors. This paper will evaluate how appropriate circuitry designed into an individual continuous NCPF sensor can be used to determine the location of impact on the sensor.

Viable NCPF sensors have been demonstrated using several different foam matrices including silicone, latex, and polyurethane. This paper will focus on the most common and affordable matrix, namely open-cell polyurethane foam; this is also the first commercially available NCPF sensor material. Polyurethane foam lends itself well to a composite material due to its ease of manufacture and insensitivity to fillers without material change in foam properties. All NCPF sensors studied in this paper were manufactured by Rogers Corporation from XRD® material in sheet form with a thickness of 12.7 mm and a 240 kg/m^3 density [74].

To ensure the efficacy of the envisaged position-sensitive self-sensing foam components, several factors that fundamentally influence the response of the system must also be studied. These include:

1. Response to Localized Impact - The mechanical and electrical response from a local impact on a large area of foam requires characterization.

2. Impactor Characteristics - The effect of different impact materials may have a significant influence on the triboelectric nature of the electrical response.
3. Electrical Circuit Considerations - The geometry and material of the probe circuitry require analysis for optimal spatial detection.

Each of these individual effects will be discussed in more detail in the following paragraphs.

Local Impact Characteristics - The spatial resolution of an impact depends upon the ability of the detection circuitry and software to correctly interpret the localized nature of the self-sensing foam's response. The magnitude of the electrical response is known to correlate with the magnitude of impact but may also relate to the volume/area of foam being compressed, and it will certainly depend upon the distance between the position of impact and the probe that is monitoring the voltage signal. These relations have not been adequately studied and will be considered here. In terms of mechanical response, the non-linear stress-strain curve associated with polymeric foams is likely to significantly modify the electrical response to impact – particularly in the densification region of the curve. When an NCPF sensor is impacted in an increasingly localized region, the mechanical response can enter this non-linear response region and see exponential changes in stiffness. The viscoelastic properties of the NCPF will be evaluated by analyzing the stress strain curves at varying strain rates.

Impactor Characteristics – Due to the triboelectric nature of the NCPF response, there is a potential for biasing of the electrical signal by different impacting materials. The electrical response is generated through the interaction between the embedded particles and the foam matrix, which has a significant disparity in triboelectric affinities [75]. It is possible that impact materials of differing affinities could affect the internal response.

Table 3-1 shows that polyurethane foam has a triboelectric affinity of +60 (nC/J) whereas the conductive filler materials used in the foam, nickel and carbon fiber, have affinities around 0 (nC/J) [76]. When two materials rub against each other the higher affinity material (polyurethane) will give electrons to the lower affinity material (nickel or carbon) resulting in a positive surface charge on higher affinity material. This paper evaluates an aluminum and Teflon impact head to determine if their triboelectric affinity affects the NCPF response.

Electrical Circuit Considerations – The probing circuit design is key to the ability to determine where an impact occurred on a surface. Several probe attributes will be evaluated with different geometries, materials, and manufacturing methods, to determine how each approach affects the response. This evaluation will look at several post-manufactured methods and compare their response to that of a probe that is cast into the NCPF during manufacture. The latter approach is also compatible with the printing of complex probe circuitry onto foam components.

Spatial Detection of Impact - Finally, the ability to resolve the spatial position of impact is assessed for a 1-dimensional trial along a continuous NCPF sensor, with varying probe geometry. The results might readily be extrapolated to 2D, or even 3D, sensing situations.

3.3 Testing Equipment

A National Instrument 9229 voltage module was initially used to evaluate the NCPF sensors electrical response. The NI-9229 module has a ±60 V sensing range with 24-Bit resolution and a sampling rate of up to 50 kHz. This system was used to evaluate the characteristics of the signal and determine the sampling requirements. It was found that most

components of the signal that correlated well with impact characteristics were in the sub 500 Hz range.

A custom-built circuit board was subsequently used to measure the voltage on most of the NCPF experiments (Figure 3-1). This board was designed specifically for the NCPF sensors, with an op-Amp voltage following circuit specially tuned for the low amperage signal. The custom board has the capability of measuring one to eight analog channels with a voltage range of 3.3 V with 12-Bit resolution; controlled by a custom iOS app. The custom board records the

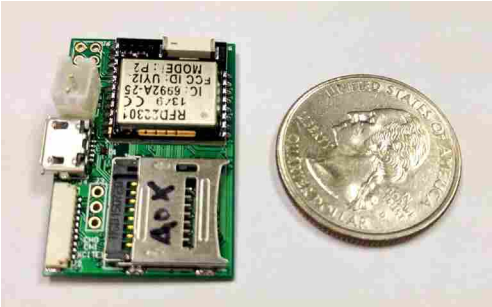

Figure 3-1: Custom micro-controller developed to measure and record NCF response.

analog signal to an onboard microSD card slot at 1000 Hz while also streaming the data to a Bluetooth device at 40 Hz.

A Dynatup 8200 drop weight impact tester manufactured by Instron was used for all impact testing. This dual guide column drop tester is capable of testing a wide range of drop energies (0 to ~300 Joules) with varying weights (2.5 to 20 kg) and heights (0 to 1.5 m). The drop tester was modified by removing the tup from the crosshead, allowing for varying drophead materials and sizes to be attached. The pneumatic brake system was removed, and a flat plate deck was placed at the bottom to accommodate the large foam samples.

3.4 Methods

3.4.1 Local Impact Characteristics

The mechanical properties of a foam significantly affect how the foam matrix responds to localized impacts. The electrical response generated within an NCPF sensor is directly dependent upon the foam's internal deformation, and therefore upon the foam matrix mechanical properties. Furthermore, as an impact becomes more localized, there is the potential for higher levels and rates of strain. While the mechanical response is affected slightly by the addition of conductive additives, this modification is secondary to the overall response of the matrix. Hence the initial study of localized mechanical response focuses on the stress-strain curve and rate sensitivity of the underlying Rogers Corporation's XRD® foam.

As elastic foam is compressed, it passes through three distinct regions in its stress-strain curve: the linear elastic region, the plateau region, and the densification region as shown in Figure 3-2 [77, 78]. The linear elastic region is controlled by the bending of the cell walls throughout the foam and is very small in elastic foams. The plateau region is associated with the collapse of each of the cells throughout the foam. Once most of the cells have collapsed the foam enters the densification region, and the void-less polymer material is compressed. When the foam is compressed into the densification region, all motion in the foam occurs through a Poisson effect, in which the sides of the foam will expand as the height decreases. It is expected that in this region, the associated triboelectric effect in NCPF foams will dramatically decrease

as the relative motion of matrix and filler reduces. Furthermore, mechanical properties of some foams, such as the XRD® foam used in NCPF, are highly rate dependent.

As a preliminary to the present work, XRD® foam samples were tested at strain rates between 0.0003 and 832 strain/sec at room temperature (23° C). Each stress-strain curve was evaluated to determine the start of the densification region. This was calculated by identifying the point on the curve where the stress exceeds the plateau slope by more than 40%, as shown in Figure 3-2. The plateau modulus, or slope, in this study, was calculated by evaluating the slope between the stress value at 10% and 30% strain. By characterizing the effect of impact

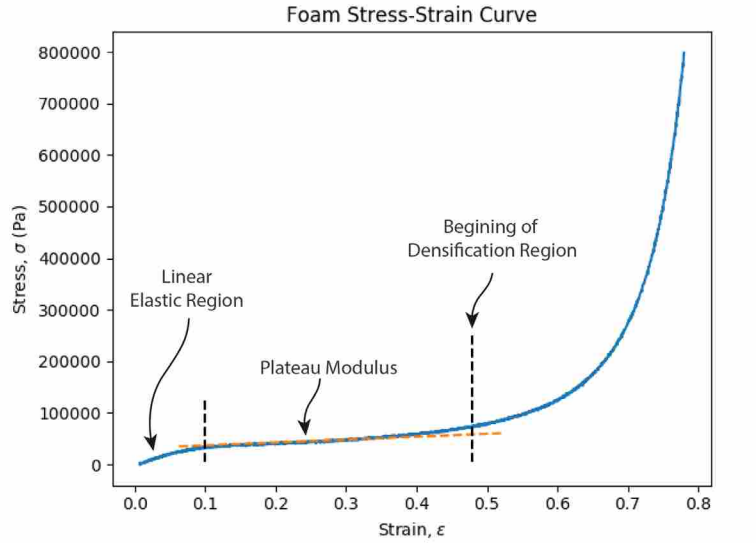

Figure 3-2: Quasi static XRD® foam Stress-Strain curve with strain regions labeled.

localization (regarding potential foam densification) across a range of impact rates, a set of design rules can be formulated to ensure the desired mechanical response (and associated electrical response) of a sensing component.

3.4.1.1 Mechanical and Volumetric Effects

The electrical response of the NCPF was tested by applying three separate impact energies to the same 12.7mm thick NCPF sensor while incrementally reducing the volume of the NCPF (Figure 3-3). The impactor head used in the testing was larger than the largest area of the sensor. The initial (largest) NCPF sensor size and impact energy were selected to ensure the energy was

Figure 3-3: NCF sensor used to determine the volumetric effects on response.

on the lower portion of the plateau region of the stress-strain curve. The NCPF was circular and constructed with a metallically coated film cast in the middle to transfer the mechanically generated voltage from the NCPF to the microcontroller. The NCPF had an initial volume of 206 cm3. Following each round of testing described below, the sensor size was incrementally reduced by 25 cm3 by cutting the NCPF according to the pattern shown in Figure 3-3. The excess NCPF was thus severed electrically from the sensor, but still provided the same (or nearly the same) mechanical resistance to deformation. Seven incremental size reductions were made, resulting in a final volume of 31 cm3. Each test was performed at one of three impact velocities, 3.17, 2.47 and 1.47 m/s, with an impact weight of 5.7 kg yielding impact energies of 3.2, 8.7 and 14.4 J. Ten impacts for each energy level were performed at each sensor size, and the voltage

response was measured for a total of 210 tests. All impact tests throughout this paper were performed on a modified Dynatup 8200 impact testing machine (Figure 3-4).

These same tests were used to evaluate how the rate of foam deformation affects the electrical response by recording several of the tests described above with a high-speed camera. A Fastcam APX RS high-speed camera was used to record the impacts at 3000 frames per second. The NCPF's strain rate and max strain were evaluated by a custom script which recorded the drop head position in each frame of the high-speed video recorded on each test. The script averaged the pixel brightness across the width of the image and calculated the position of the drop head in each frame. Each test was evaluated for both the max strain and the average strain rate.

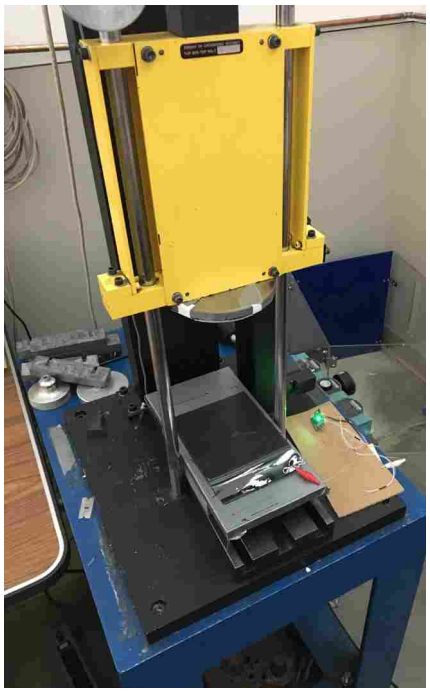

Figure 3-4: Modified Dynatup 8700 impact tester with interchangeable heads.

3.4.2 Impactor Characteristics

While all testing was performed under controlled conditions the NCPF is ultimately used in many environments and comes into contact with varying materials. When an impact head comes into contact with the NCPF, it can potentially bias the internal triboelectric response via a triboelectric effect at the surface of the sample. The aluminum and Teflon impactor heads represent different triboelectric affinities which might cause such a bias (Table 3-1). Teflon (-190 nC/J) and aluminum (0 nC/J), were selected to represent materials at the bottom and middle of the triboelectric affinity series in comparison to the NCPF sensor's main ingredient, polyurethane (+60 nC/J), which is found near the top of the series (Table 3-1). A testing procedure was created in which the NCPF sensors were impacted with materials with varying impact energies and different impact head areas, all of which were smaller than the NCPF. The impact head size variations are varied to evaluate how the triboelectric interaction between the NCPF and head contributes to the overall response.

Table 3-1: Several materials with their associated triboelectric affinities.

Material	Affinity (nC/J)
Polyurethane foam	+60
Polyurethane	+40
Nylon	+30
Glass	+25
Wool	0
Nickel, Copper	-
Acrylic	-10
Polystyrene	-70
Silicone	-72
PVC	-100
Latex natural rubber	-105
Teflon	-190

Six custom-made circular disc-like impact heads, made of aluminum and Teflon, were attached to the Dynatup drop tester and dropped from varying heights on an NCPF sensor (13 cm diameter and 12.7 mm thick). Three of the impact heads were made of Teflon and had diameters of 5.1 cm, 9.7 cm, and 12.7 cm. These diameters yielded surface areas of 20.3 cm^2, 73.2 cm^2 and 126.6 cm^2 respectively (Figure 3-5). The remaining impact heads were made of Aluminum and were the same diameter and surface area as the aforementioned Teflon impact heads. The thickness of each impact head varied between 13 and 24 mm, yielding masses of 70, 280, and

Figure 3-5: Teflon and aluminum impact heads used to test impact material effects.

700 g for the aluminum heads and 60, 210 and 370 g for the Teflon heads. Each of the impact heads was dropped from three different energy levels: high (34.9 J), medium (21.6 J), and low (8.26 J), five times each. In order to account for the differences in mass between each impact head, the heights from which the impact heads were dropped were adjusted to yield the correct energy.

3.4.3 Electrical Circuit Considerations

A primary consideration in an NCPF system design is the electrical circuit used to transmit the sensor's response to a voltage measurement device. Thus, the conductive probe material, its geometrical arrangement, and the means of attaching it to the NCPF were studied. Previously

reported studies on probe configuration demonstrated that the voltage response for copper wires cast into the foam was directly related to the area of the conductor, which in the reported tests was also related to the volume of foam sampled by the probes. It was also reported that wires inserted into the foam after manufacturing induced noise in the voltage response. In the current study, various film-like circuits were tested as potential replacements for embedded wires.

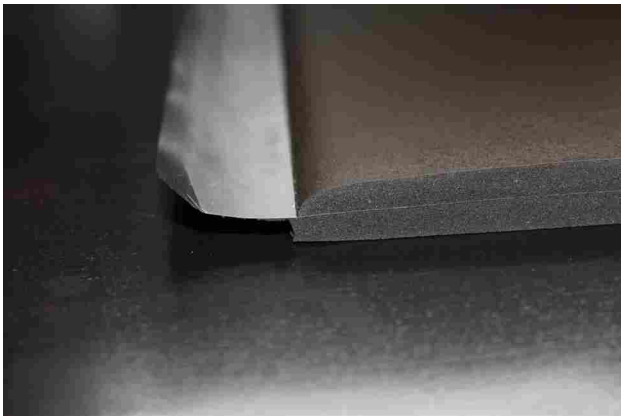

Figure 3-6: Cast NCF sample with metalized PET film in the center.

Two probe configurations were evaluated; one design was incorporated directly into the manufacturing of the NCPF (cast) while the other one was added after the foam was cast (adhesive). When casting the NCPF foam into the sheet, a metallically coated Polyethylene Terephthalate (PET) film was added in the middle of the liquid product, with a resultant probe configuration as shown in Figure 3-6. This process allowed for a continuous cast sheet of NCPF with embedded electrode material, which could be cut into multiple sensors of arbitrary geometry from the same sheet. The other conductor was applied to the foam surface after casting. The same metallically coated film as described above was adhered it to the NCPF with a conductive adhesive. The final stack was configured similarly to the cast NCPF sensor in Figure 3-6 with two NCPF pieces adhered to both sides of the film. Both of the conductors were tested

under the same impact conditions to evaluate their effectiveness in gathering the electrical response.

All samples had a density of 240 kg/m^3 with a final thickness of approximately 12.7mm and were tested with ten impacts from three different heights (0.11, 0.31 and 0.51 m), with two different masses (4.7 and 6.79 kg), resulting in six different impact energies. Each sample was connected to the same custom microcontroller described above, and all voltage responses were recorded.

3.4.4 Spatial Detection

During an impact event in an NCPF sensor, a voltage is created that propagates through the volume of the sensor. It was hypothesized that the voltage, measured at different locations throughout the volume of the NCPF, could be used to determine the location of impact based on the electrical signal decay as a function of distance from impact area. An example conductor configuration intended to resolve the 1-dimensional position of impact on an NCPF sheet is shown in Figure 3-7. Several similar configurations were evaluated to determine ideal spacing

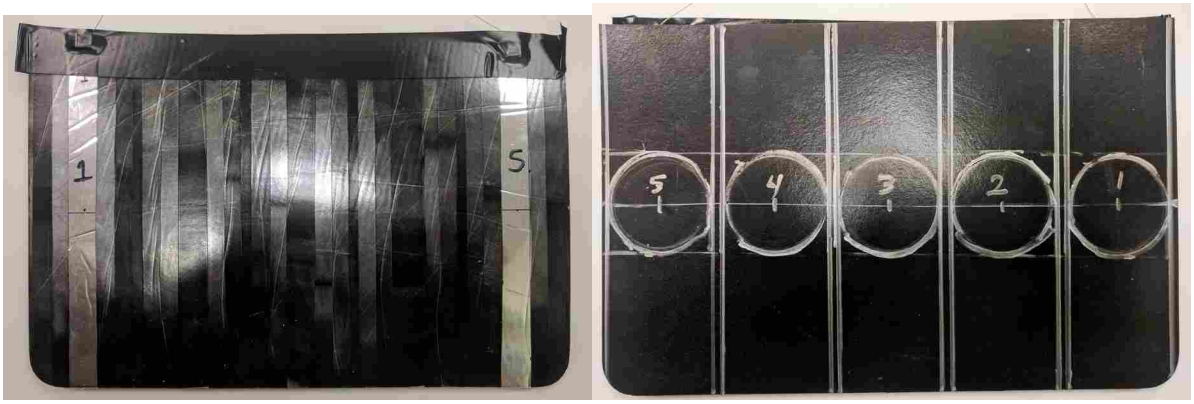

Figure 3-7: (Left) Bottom side of NCF sensor with two conductive probes, 1 and 5, added to measure location of impact. (Right) Demonstrates the impact locations that correspond to the same numbers on the bottom side. Each probe configuration was evaluated with 3 impacts above each location, the final testing configuration is shown.

and conductor area, resulting in different probe to sensor ratios. The goal was to identify a minimum probe-to-sensor area ratio which provided accurate spatial resolution of the impact location.

The 1D spatial resolution and sensing radius of the NCPF was evaluated by modifying an initial probe configuration of a 220 mm x 140 mm x 8.5 mm NCPF sensor, which was originally cast onto a continuous metalized PET film. The film was separated into five separate columns by scoring and pealing a portion of the film away from each probe. The initial width for each probe was 37.7 mm and was reduced to 24.7 and 9.1 mm in subsequent tests. To increase the distance between the sensing areas in subsequent tests, columns 2 and 4 were removed, followed by column 3. The final test only involved columns 1 and 5. The spatial impact detection was evaluated by impacting each configuration at the five positions shown in Figure 3-7, while recording the response from all attached probes simultaneously for a total of 75 tests.

3.5 Data Processing

All NCPF voltage data collected for this paper were collected at 1000 Hz with the custom microcontroller previously described. The sampling rate was preset on the microcontroller and was selected to be two to three times the Nyquist frequency found in the NCPF's electrical response throughout a wide range of impacts. All data was post-processed with a 5^{th} order low-pass Butterworth filter with a cutoff frequency of 200 Hz. The upper cutoff frequency was selected by evaluating the Fourier transform of the raw signal. By evaluation of the FFT frequencies in Figure 3-8, one can see most of the signal is comprised of frequencies ranging from 0 up to 100 Hz. However, there is another band between 100 and 200 Hz that is picked up with the 200 Hz cutoff.

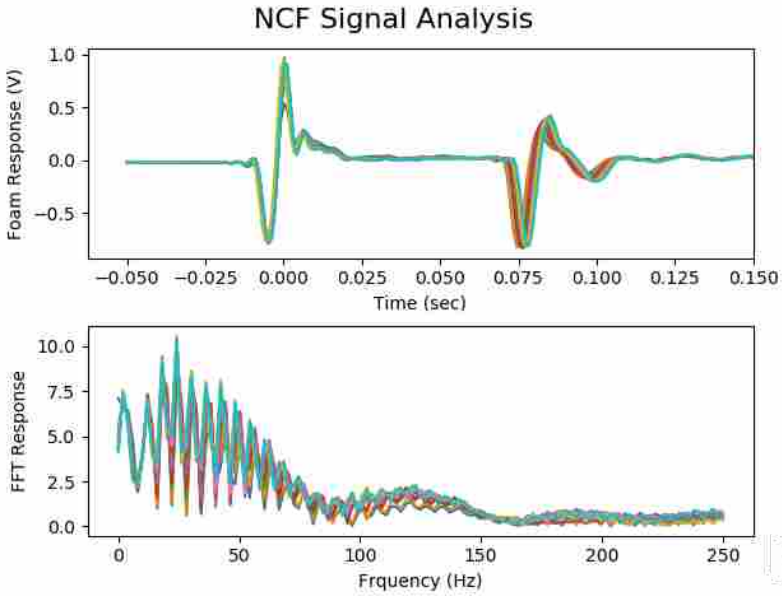

Figure 3-8: Typical NCF response to impact, both plots show the analysis of 10 separate impacts. Top: FFT vs frequency response. Bottom: NCF voltage response vs time.

Two different measures of NCPF response were assessed: the peak voltage (Peak) and the Integral of the Absolute Voltage (Integral). Peak voltage is one of the most straightforward measures to extract from the signal and has been used extensively in correlation to impact energy in other works [14-16]. The peak was selected by identifying the first positive peak voltage value in the signal (Figure 3-8). Integral has also been used to account for the overall charge displacement in the signal [14]. This metric accounts for the total electric oscillation in a signal during the impact event and often provides different insights to impact mechanisms than peak alone.

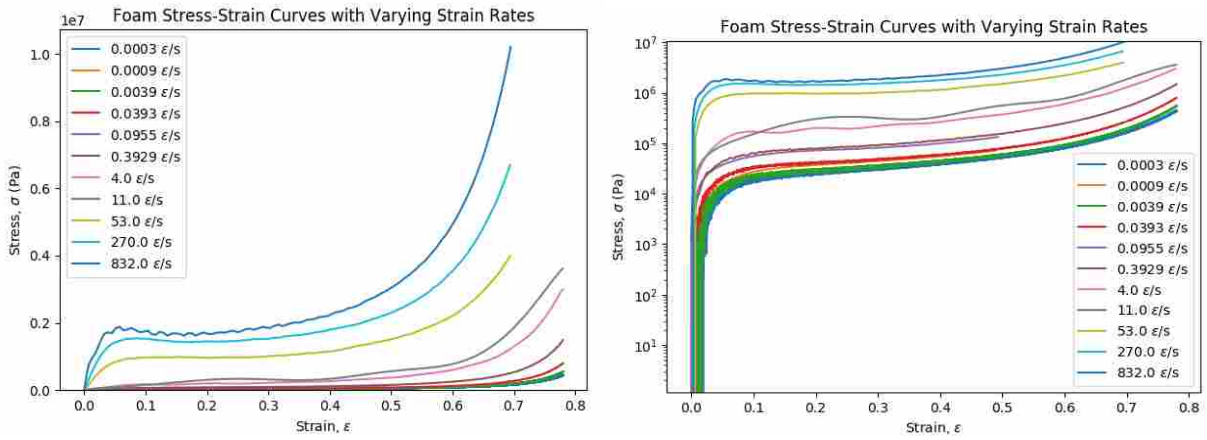

Figure 3-9: Stress-Strain curves for Roger's XRD foam at varying strain rates. (Right) Stress on a log scale to demonstrate similarities in shape between all curves,

3.6 Results

3.6.1 Local Impact Characteristics

Figure 3-9 displays the stress strain curves for the polyurethane foam at various strain rates. The foam displayed viscoelastic tendencies, with the higher strain rates resulting in several orders of magnitude higher stresses at the same strain compared with quasi-static deformation. Furthermore, the foam reaches the densification region at reduced strains with these higher strain rates. Figure 3-10 demonstrates the correlation between strain rate and densification strain. As the strain rate increases the densification of the foam decreases until approximately 50 strain/sec where the slope changes. The leveling of the slope indicates the material properties become less strain rate dependent at the upper limit of testing. Densificaiton is only one measure of the foam, however, it provides evidence that the material properties have an exponential nature. By visual inspection of both Figure 3-9 and Figure 3-10, it demonstrates that the properties of the XRD material are both, highly rate dependent and show evidence that higher rates approach an asymptote. Current testing methods were limited to strain rates up to 832 strain/s, thus further testing would be required to verify these trends at higher rates. All testing in this paper exceeds

the 53 strain/sec strain rate which allows us to assume constant, or nearly constant, densification of approximately 0.48 strain. The constant densification strain simplifies the spatial detection analysis and allows for a correlation that is independent of strain rate.

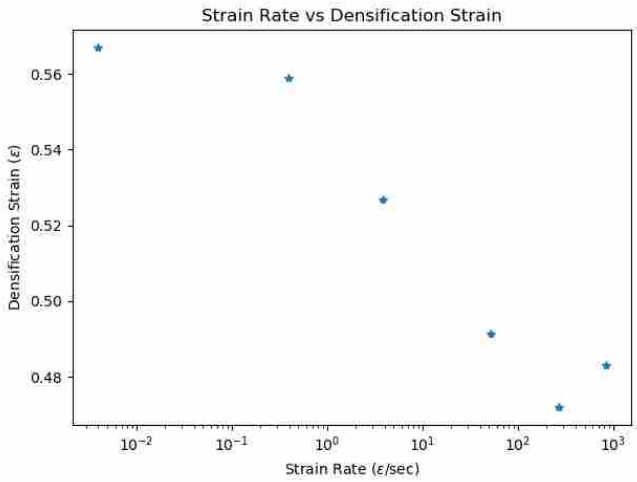

Figure 3-10: Measured densification of the foam at varying strain rates.

3.6.1.1 Mechanical Effects on Electrical Response

To evaluate how strain rate and max strain affect the NCPF peak voltage response, a sample of NCPF was tested at set impact energies while reducing the volume of the sensor. By reducing the volume and maintaining the same impact energy the impact energy to volume ratio increased, pushing the mechanical response into the densification range. Figure 3-11 demonstrates how the NCPF's normalized peak voltage, when log-transformed, shows a linear correlation to max strain. Two separate linear models were fit to the data by impact energy. Each model showed strong correlation from 0.10 to approximately 0.47 strain with R^2 values of 0.99 and 0.95 for 8.7 and 14.4 Joule impact energies respectively.

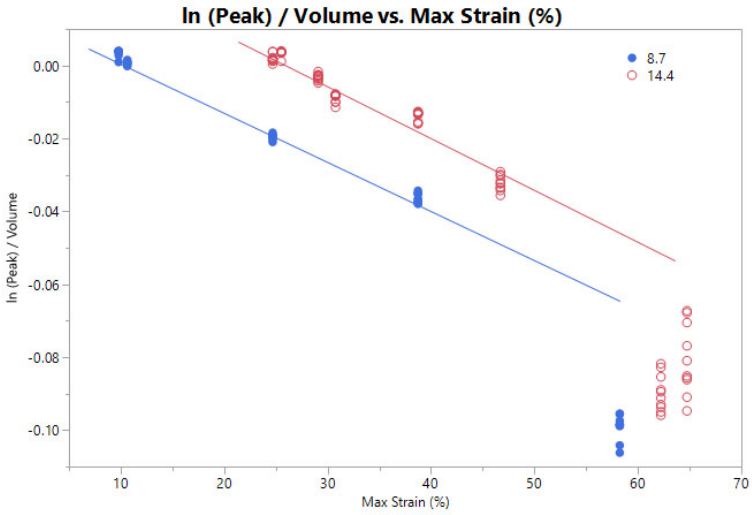

Figure 3-11: Analysis of log transformed peak voltage with relation to max NCF strain. There is a linear correlation present throughout the lower strain rates that extends up until approximately 50-55% strain, where there is a sharp decrease in voltage response. This discontinuity in response correlates well with the calculated densification of the foam evaluated in the previous section.

When the max strain exceeds 0.47 strain, the linear model breaks down and the peak voltage no longer follows the expected pattern. The change in electrical properties occurs at the previously observed densification strain demonstrating that the internal triboelectric generation changes when the foam densifies. It is proposed that when the NCPF is compressed into the densification region, it creates a change in both the material and electrical properties of the NCPF. When the impact conditions enter this region, the foam exponentially stiffens as the voids completely compress, altering the mechanism behind the electrical response. The resultant voidless compression results in less motion between the particles and the foam matrix limiting the triboelectric generation. These results highlight the need to design a system in which the NCPF operate within the elastic and plateau regions of motion. These design criteria align well with standard design practices in foam. If foam enters the densification region it no longer

provides adequate protection and the design should be reconsidered. These analyses show the direct correlations between electrical response and physical deformation of the NCPF sensors. When these results along with the predicted densification of the foam are combined, it provides upper limit design considerations to be used in the final spatial detection model.

3.6.1.2 Volumetric Effects

Individual Volume Models by Energy

The linear correlation between the natural log of peak voltage and NCPF volume, by impact energy, is shown in Figure 3-12. The linear model is described as

$$\ln(Peak) = a * Volume + b \tag{0-1}$$

where a is the slope and b is the electrical DC offset. This linear model fits the data well with R^2 correlations of 0.90, 0.92 and 0.91 with slopes of 0.017, 0.017 and 0.15 for 3.2, 8.7 and 14.4 impact energies respectively. Not only does each model fit well, but the DC offsets are linearly spaced with respect to energy. When the DC offsets are back transformed to peak voltage, we see that with each increase in impact energy we see an increase of 0.0047 V in the peak response. These results demonstrate that the voltage is a function of both impact energy and NCPF volume. Impact energy increases the triboelectric generation through increased interactive motion between the particles and the foam matrix. The volume of the NCPF exposed to the impact increases the potential to generate more triboelectric charges by having more particles or nano-generators present. Thus, the peak voltage can be adjusted by changing the size of the NCPF sensor.

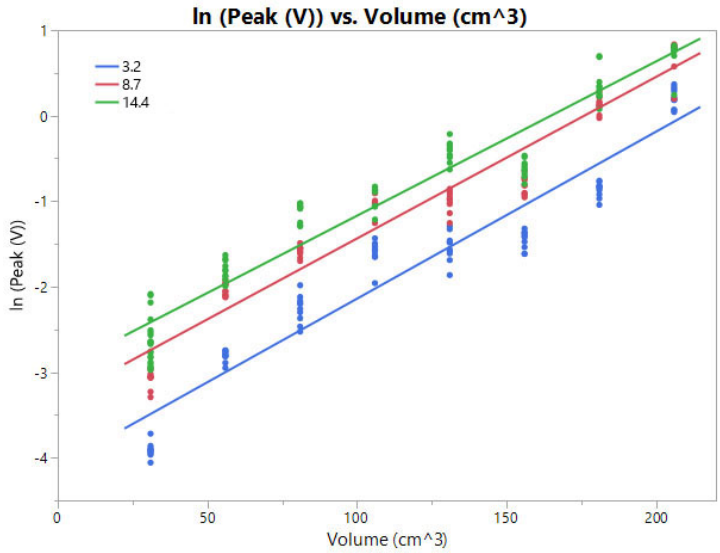

Figure 3-12: The log transform of the Peak voltage is linearly correlated to NCF volume with increased response from larger impact energies.

Combined Model

The previous models demonstrated that impact energy can be correlated directly to both the NCPF impact volume and impact energy. A combined model to predict voltage response in terms of both impact energy and NCPF impact volume can be derived from the test results as

$$Peak(E,V) = \ 0.0098 * E^{0.4446} * e^{0.0207*V} \qquad (0\text{-}2)$$

where E is impact energy measured in Joules and V is NCPF impact volume measured in cubic centimeters. The measured voltage vs predicted voltage based on the model is shown in Figure 3-13. The model works very well over the large impact energy range found in this testing procedure with an R^2 of 0.92.

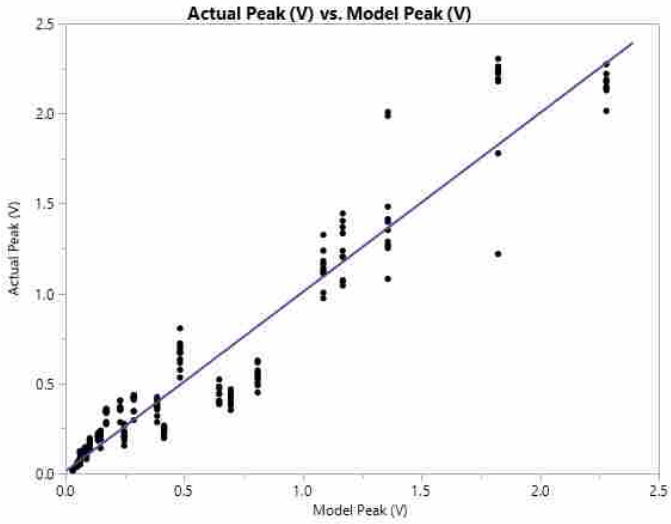

Figure 3-13: Measured peak voltage vs predicted model as a function of volume and impact energy with R^2 of .92.

3.6.2 Impactor Characteristics

The effect of impact head material and size were evaluated by measuring the peak electrical response from 180 drop tests on one NCPF sensor. A multiple regression model was created to evaluate impact material and impact area to the Peak voltage response. The model started with the input variables: impact head material, impact head size, and impact energy. Not all variables were significant; those which were not significant were trimmed until the model only contained the statistically significant variables. Impact material and impact energy were found to be significant input variables whereas impact head size was not. For peak voltage, the regression coefficients for both impact energy and impact head material were statistically significant, with p-values of <.0001 and 0.0025 respectively. For impact energy, when regressing Peak on impact energy, it indicates that for every increase of one Joule we expect an increase of 0.046 V in Peak.

The difference in peak voltage between Aluminum and Teflon impact heads can be found in Figure 3-14. The aluminum impact head creates an increased peak voltage of approximately 0.2 volts on average between all impacts. It is proposed that this is caused by the differences in triboelectric affinity between Teflon and aluminum. As both materials come into contact with the NCPF they will either rob or deposit electrons into the surface of the sensor. Teflon deposits electrons to the system and reduces the peak voltage response in the NCPF. Aluminum has a neutral triboelectric affinity, which neither deposits nor robs electrons from the system.

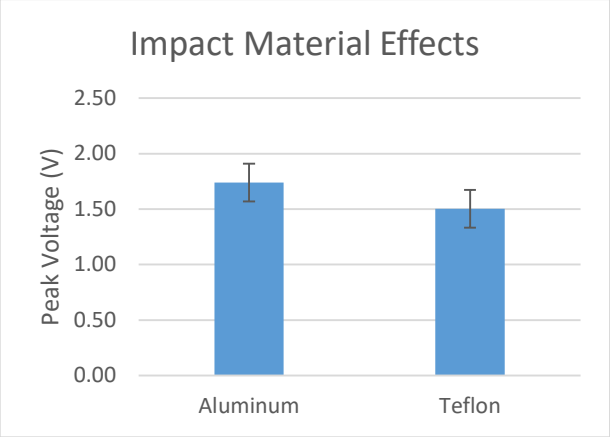

Figure 3-14: Impact material effects on NCF peak voltage.

The initial hypothesis was that changing the surface area between the different impact heads would result in different triboelectric charges. This hypothesized relationship between the impact head surface area and Peak voltage didn't manifest itself in this experiment and could be due to the competing strain rate dependence of the electrical signal. We now hypothesize that as the impact head area is reduced, the strain rate increases creating a larger peak voltage response, while the triboelectric generation between the head and the NCPF decreases. When the impact head area increases, the strain rate decreases but the triboelectric generation increases, resulting in competing effects.

3.6.3 Electrical Circuit Considerations

Peak voltage from 120 impact tests comparing the cast electrode with the SLA adhesive electrode was evaluated in a multiple regression model to assess the effects of xyz on responseto allow for direct comparison of each probe while accounting for all tested impact energies. The differences in mean peak voltage between the electrical probes are represented in the bar graph found in Figure 3-15. In the regression of Peak on impact energy and conductor type the affect

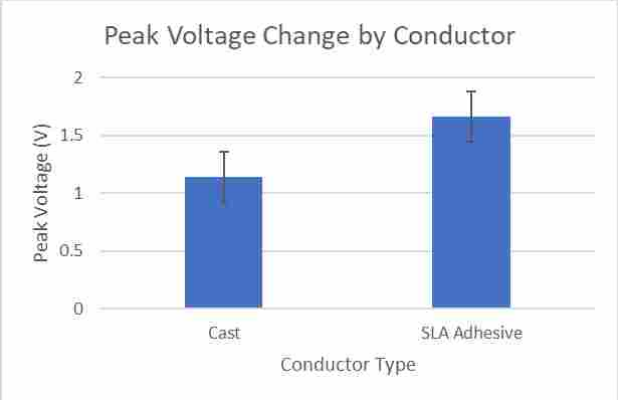

Figure 3-15: Peak voltage means for both conductor types with error bars reflecting variability after adjusting for differences in impact energy.

for conductor type was found to be statistically significant with the adhesive sample providing a larger response than the cast sample. In a simple linear regression, with Peak on impact energy for each of the two circuits, we find that the cast sample doesn't provide as large of a peak voltage response but does have the strongest correlation to impact energy with an R^2 of 0.85, whereas the adhesive sample had an R^2 of 0.76. The conductive adhesive that was used in this analysis is a prototype material and is expected to increase in performance as the formulation is finalized. Future work will evaluate the difference between the conductors used in each probe system. The electrical probes come with varying levels of difficulty in manufacture and measurement accuracy, which must be considered when designing a sensing system.

3.6.4 Spatial Detection

From initial evaluation of the signal, shown in Figure 3-16, there was an apparent difference between the signal closest to the impact area (red) and those adjacent to it (gray). The probe closest to, or directly beneath the impact, showed an initial negative spike with a larger magnitude positive spike afterward, whereas the adjacent probes showed a lower magnitude response that mirrors the signal (e.g., opposite in sign, similar signal shape) from the impact location. The Peak and Integral of each channel were calculated and reported for each test. These measures have been shown to accurately and effectively determine the magnitude of impact within NCPF systems [14, 15].

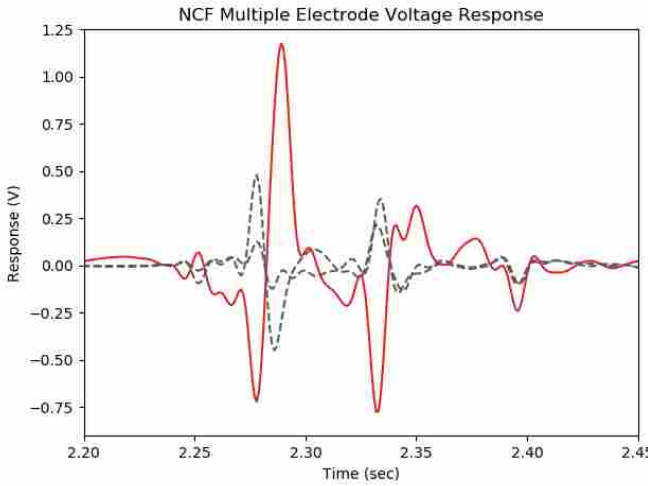

Figure 3-16: Typical NCF response to impact with multiple voltage measuring probes within NCF. The red plot is the response from the probe which was impacted, and dashed gray lines are from the two adjacent probes.

The electrical response, Peak and Integral, from each of the NCPF's electrode locations, was evaluated by Linear Discriminant Analysis (LDA) and multiple regression analysis. An LDA location model was created to determine the discrete location of each impact whereas the multiple regression analysis was used to predict a continuous location. The discrete model was

intended to predict the best fit variable which was independent of location. Each variable represented one of the five sensing columns, each column having a width of 44 mm. The accuracy of the discrete model was determined by how often the model predicted the correct column of impact. The continuous model was intended to predict an exact location along the continuous length of the sensor. A multiple regression model was created to predict the exact location of impact along the sensor. The accuracy of the continuous model was reported as the predicted distance from the actual impact centerline. Both models were cross-validated via hold-one-out cross-validation.

The discrete model results are outlined in Table 3-2. Each row represents a specific probe configuration with, number of column probes, width of the probe, and probe-to-sensor area ratios reported. For example, when the NCPF system has all five probes with a probe-to-sensor area ratio of 86%, the discrete Peak and Integral models predicted 93% and 100% of the impacts correctly, respectively. Both models showed great accuracy until the probe-to-sensor area was reduced below 12%, where the Peak model saw a large reduction in accuracy. The Integral model showed higher accuracy throughout the entire range of probe-to-sensor ratios, with the lowest accuracy model still predicting 87% of the impacts correctly. The current probe arrangement would allow for a spatial accuracy to as fine as 44 mm. Further testing would need

Table 3-2: Percent of correctly classified locations using a Linear Discriminant Analysis classifier. All classification rates are estimated using hold-one-out cross validation.

Sensing Columns	Probe Width (mm)	Probe Area (mm^2)	Probe-to-Sensor Area Ratio (%)	Peak Model Accuracy (%)	Integral Model Accuracy (%)
5	37.7	26390	86	93	100
5	24.7	17290	56	100	100
5	9.1	6370	21	93	100
3	9.1	3822	12	100	100
2	9.1	2548	8	53	87

to be carried out to determine if a different configuration with a smaller spacing between probes and a lower probe area to sensing area ratio would result in higher resolution.

Table 3-3: Summary of continuous multiple regression analysis spatial accuracy. All prediction accuracies are estimated using hold-one-out cross validation.

Sensing Columns	Probe Width (mm)	Probe Area (mm^2)	Probe-to-Sensor Area Ratio (%)	Peak Model Resolution (mm)	Abs Int Model Resolution (mm)	Peak Model Accuracy (%)	Integral Model Accuracy (%)
5	37.7	26390	86	25.91	14.05	87	87
5	24.7	17290	56	26.35	19.71	67	80
5	9.1	6370	21	11.20	4.83	93	100
3	9.1	3822	12	33.18	44.87	60	47
2	9.1	2548	8	398.15	211.97	33	47

In contrast, the continuous model predicts the location of an impact along the length of the sensor. The absolute distance in millimeters between the predicted location of impact and the actual center of impact was calculated and is reported in Table 3-3. The accuracy of each continuous model was determined by whether or not the predicted location was within the width of each column. For example, when all five probes were present, and the probe-to-sensor area ratio was 21% the continuous Peak and Integral models predicted the center of impact within ± 11.2 and 4.83 mm of the center of impact, resulting in 93 and 100% accuracy respectively. The accuracy of this model appears to be dependent upon the probe to sensor ratio and number of probes present. Figure 3-17 demonstrates the absolute distance between prediction and actual impact location vs probe-to-sensor area ratio. The data indicate that 5 column probes with a probe-to-sensor area ratio of 21% provided the best accuracy of the tested configurations. Above the 21% ratio, the accuracy is reasonably constant but below 21% the accuracy diminishes very

quickly. The reduction in the probe-to-sensor area ratio from 86 to 21% was due to the narrowing of the probes. The reduction from 21 to 8% was caused by removing probes.

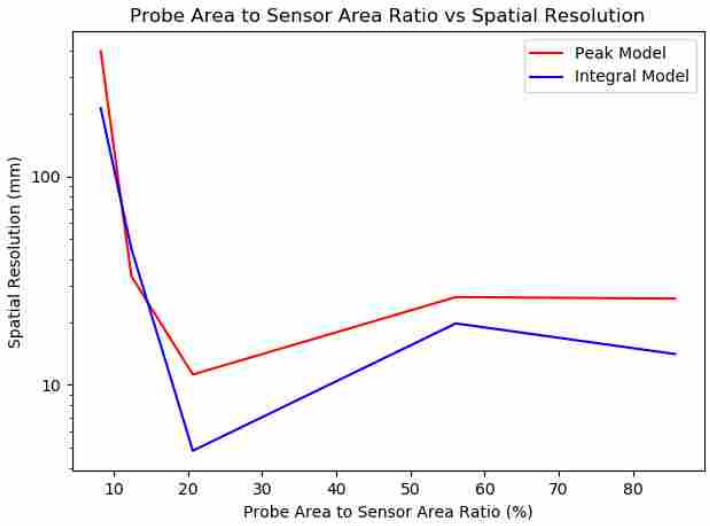

Figure 3-17: NCF sensor spatial accuracy is dependent upon the probe to sensor area ratio. If the ratio drops below approximately 20%, the accuracy dramatically decreases. Both the Peak and Integral models are demonstrated.

It is proposed that each probe has an effective sensing radius; when impacts occur beyond that sensing radius, accuracy diminishes. The sensing radius is dependent upon the electrical properties of the NCPF, as well as the magnitude of the generated signal. As the electric charge travels through the NCPF, it dissipates. Thus, a larger charge can travel further before it has completely decayed resulting in a larger sensing radius. Figure 3-18 demonstrates the differences between the LDA and multiple regression models. This plot demonstrates the trend in which the lowest probe-to-sensor area ratios loose accuracy. These results show that an optimum sensor width for both models was 6.5 mm with all five probes present. LDA was able to achieve higher accuracy across all sensor configurations than the multiple regression and would be a strong

method to be used in determining location of impact in a NCPF system especially if more tightly spaced probes proved to be as accurate.

The spatial detection of an NCPF system signifies an evolutionary step in sensor progress and allows a much larger functional base for future systems. The discrete model provides basic yet strong correlation while the continuous model allows for applications where spatial resolution is of importance. Future work will create models that combine multiple electrical responses to increase spatial accuracy while also determining other characteristics of the impacts.

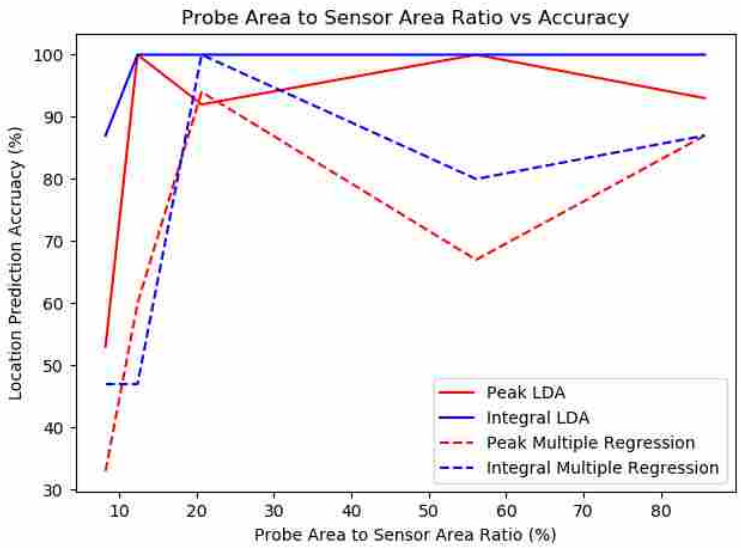

Figure 3-18: Comparison of Linear Discriminant Analysis and Multiple Regression models for spatial accuracy with respect to probe-to-sensor area ratio.

3.7 Conclusion

The purpose of this study was to identify an NCPF system which could accurately measure spatial location of impact within a single NCPF sensor. When an NCPF signal is adjusted for mechanical and electrical response variables, the sensors can provide accurate spatial detection.

This paper provides guidance to adjust the electrical response to various NCPF sensor sizes, impact materials, and electrical probe designs to increase spatial accuracy. The volume of the NCPF sensor had a positive correlation with electrical response; the more volume present to generate the response the higher the response. These tests only evaluated a limited range of volumes, but the correlation was strong and suggests the same trend would continue through larger volumes. Impact material was found to affect only the peak voltage response while Integral and FFT were not affected; however, these metrics were affected by impact head size while peak voltage was not. Additionally, the electrical probe design was evaluated, and it was determined that the signal changes magnitude dependent upon the probe selected. The cast and conductive adhesive samples provided correlation to impact magnitude, with varying levels of accuracy dependent upon probe design. This provides freedom in designing the NCPF sensor to meet the requirements of the system.

Once the electrical and mechanical variables are taken into consideration and the signal is tuned the spatial location of the impact can be determined with sub centimeter accuracy. Two different methods were used to determine the location of impact, the window and continuous predictions. When predicting the impact location within a window as wide as the impact head (i.e., the discrete model), the accuracy was sufficient using both Peak and Integral models. Best results for the continuous model were found when the electrodes were trimmed to 6.5 mm wide with all five electrodes present and resulted in spatial accuracy of the width of the window with 100% accuracy. Both the Integral continuous and the Peak continuous models were able to predict the location of impact with 4.83 mm and 11.20 mm accuracy respectively. These results demonstrate a sensor that is capable of high spatial accuracy measurements while also providing impact mitigation and magnitude measurement. This paper demonstrated that the spatial

detection can be applied along a single axis, however these same methods could be used to extend the functionality to 2 dimensions by providing a secondary circuit on the opposite side of the NCPF sensor. The NCPF sensors provide unique multifunctional capabilities with highly customizable material properties which allow the sensors to be used in the burgeoning wearable sensors space.

3.8 Acknowledgements

This material and research are based upon work supported by the National Science Foundation under grant numbers CMMI-1235365 and CMMI-1538447.

4 NANO-COMPOSITE FOAM SENSOR SYSTEM IN FOOTBALL HELMETS

4.1 Abstract

American football has both the highest rate of concussion incidences as well as the highest number of concussions of all contact sports due to both the number of athletes and nature of the sport. Recent research has linked concussions with long term health complications such as chronic traumatic encephalopathy and early onset Alzheimer's. Understanding the mechanical characteristics of concussive impacts is critical to help protect athletes from these debilitating diseases and is now possible using helmet-based sensor systems. To date, real time on-field measurement of head impacts has been almost exclusively measured by devices that rely on accelerometers or gyroscopes attached to the player's helmet, or embedded in a mouth guard. These systems monitor motion of the head or helmet, but do not directly measure impact energy. This paper evaluates the accuracy of a novel, multifunctional foam-based sensor that replaces a portion of the helmet foam to measure impact. All modified helmets were tested using a National Operating Committee Standards for Athletic Equipment (NOCSAE)-style drop tower with a total of 24 drop tests (4 locations with 6 impact energies). The impacts were evaluated using a headform, instrumented with a tri-axial accelerometer, mounted to a Hybrid III neck assembly. The resultant accelerations were evaluated for both the peak acceleration and the severity indices. These data were then compared to the voltage response from multiple Nano Composite Foam (NCF) sensors located throughout the helmet. The foam sensor system proved to be accurate in measuring both the HIC and Gadd severity index, as well as peak acceleration while also providing additional details that were previously difficult to obtain, such as impact energy.

4.2 Introduction

Concussions due to contact sports have received a great deal of attention in recent years. For decades, the dangers were ignored or misunderstood, but with scientific data showing they are more dangerous than originally assumed, they can no longer be overlooked [79-83]. Younger athletes are believed to be more susceptible to concussion than older athletes and can have severe, acute, and long-term complications that are not found in their older counterparts [84-86]. Furthermore, it has been found that young athletes do not consistently self-report concussion, or concussion related symptoms, with some studies showing only 21% self-reporting [87]. A recent study found that out of 20 high school sports football had the highest incidence of concussion with an injury rate of 22.9 concussions per 10,000 athletic exposures, defined as one athlete participating in one athletic practice or competition [88]. Many scholars and medical professionals are looking for ways to more effectively quantify both the frequency and severity of impacts the players are experiencing [89-94]. With an increased understanding of athlete exposure throughout a game and even over a player's career, medical professionals and helmet designers can better identify and protect against injury.

Real time impact detection has become a reality with the introduction of consumer-based accelerometer systems [95]. Wearable devices have been developed to measure and/or calculate the head's linear and angular acceleration during impact. These devices vary in their design and function, but generally depend on several different accelerometers and gyroscopes. These sensors have been directly implemented into helmets, patches (adhered to the skin), earplugs, skullcaps, mouthpieces, or chinstraps [96-102]. The accuracy in determining location and severity of impacts of each implementation has become the focus of researchers [103]. One system that is often included in studies is Riddell's Head Impact Telemetry System, or HITS [99,

104]. Riddell's HIT system has been used in studies to determine severity and frequency of head impacts during a full season of play [105, 106]. These data are then used to determine the effectiveness of efforts to reduce athlete concussion risk. These systems are experiencing a low adoption rate due to several factors: the expense (HITS costs $1,200 per helmet), difficulty of operation, and the limited number of helmets that are compatible with the system.

Many of the current football impact measurement systems are mounted directly into or on the helmet and almost exclusively use accelerometers. These systems have been shown to overestimate head motion and head exposure [107, 108]. Some systems, including the HITS, have attempted to reduce this disparity by using accelerometers that are pressed to the head with springs to maintain constant contact [109]. Furthermore, it has been shown that helmet fit can affect the accuracy of the HIT system [105]. Some systems attempt to directly measure head acceleration through closer contact with the head in the form of mouth guards, patches, or skull caps [103, 110, 111]. Some systems, such as Riddell's Insight and Shockbox's impact detection system, make no attempt in overcoming this disparity through design; it is assumed it is accomplished through post-processing. These issues are not easy to overcome and have been widely overlooked in previous work.

The most widely accepted mobile gold standard helmet sensor is Riddell's HITS [99, 109]. Duma *et al.,* demonstrate that Riddell's HITS was capable of real-time measurement of impacts during football practice and games. HITS correlated well with a helmet-equipped Hybrid III dummy instrumented with an accelerometer array ($R^2 = 0.97$) *[109]*. Other systems have shown similar results by different implementations [96, 103, 112, 113]. However, HITS only works with two different Riddell helmets. Additionally, the other systems mentioned must be calibrated for each helmet based on where the sensor is placed on the helmet. This paper seeks to evaluate

the accuracy of a new NCF-based sensor that could be adapted into existing helmet designs. An ideal system would be compatible with any helmet type and provide measurement of impact directly experienced by the head.

4.3 Materials and Methods

4.3.1 Nano Composite Foam (NCF) Sensors

This paper demonstrates the use of a new type of foam sensor that can measure impacts through a triboelectric response, to compression and subsequent relaxation. The triboelectric charge is generated by an interaction between the nickel-based additives and the polyurethane foam matrix. The NCF is created by adding nickel nano particles and nickel coated carbon fiber to the liquid components of polyurethane foam prior to casting. The foam is cast around a conductive electrode, which is used to measure the generated charge and transmit it to the measurement device. The NCF sensors used in this experiment used stranded copper wires, however other NCF sensors use conductive films to measure the response. With further development, the NCF sensors can be implemented into foams currently used in helmets.

The NCF response is dependent upon several characteristics (strain rate, total strain, impact area, impact duration, etc.) of the impact which may prove helpful in head impact measures. When the foam is impacted, it creates both a positive and negative voltage response as shown in Figure 4-1. The NCF response scales with the magnitude of the impact and is strongly dependent upon both the impact force and initial velocity. Impact force correlates to the maximum strain whereas the initial impact velocity significantly affects the strain rate. Higher rates of strain will result in larger NCF charge generation if the foam doesn’t bottom out or enter the densification

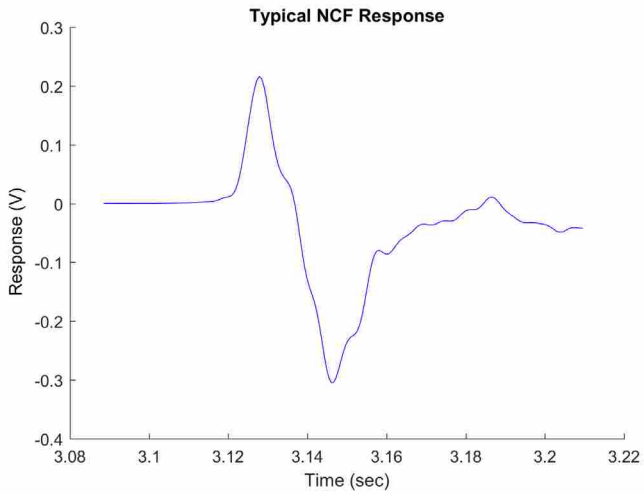

Figure 4-1: Typical NCF voltage response to dynamic deformation or impact.

region on the stress strain curve. The NCF response maintains a linear correlation throughout the plateau region of the stress strain curve but that correlation breaks down as it passes into the densification region. Figure 4-2 demonstrates a general correlation between impact energy and NCF voltage response with strains within the plateau region. The NCF sensors were designed to keep the strain of the sensors in the lower half of the stress strain curve with no strains exceeding 50%. As the NCF response is dependent upon both the impact velocity and force it allows the foam to measure the standard helmet impact metrics of interest to researchers.

The nature of the NCF material lends itself particularly well to the football helmet environment, where the sensor acts multifunctionally. It directly replaces the existing traditional foam padding and provides equivalent energy absorption, while also measuring impact data. Football helmets are designed with the goal of reducing the amount of energy that is transferred to the head. A portion of the energy is absorbed and dispersed in the helmet's shell, while the rest is either absorbed or transferred to the head via the foam. Due to their positioning in the direct

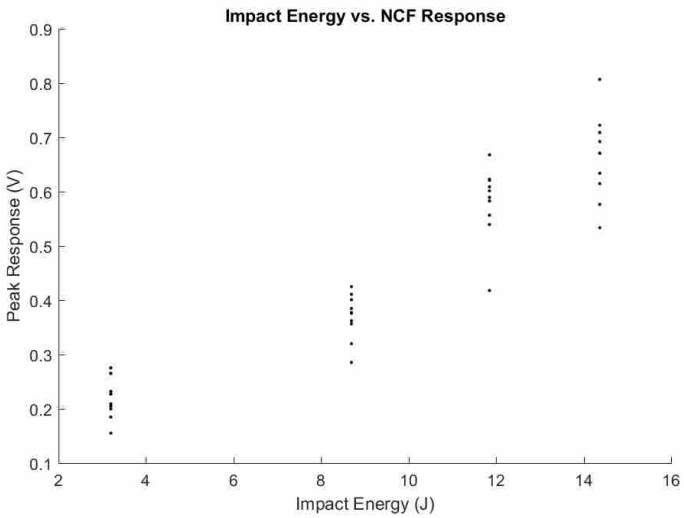

Figure 4-2: NCF peak response to varying levels of impact energy.

line of action between the helmet shell and the energy is transmitted to the player's head, the deformation of the foam sensors can directly measure how much of the impact energy is passed to the head.

4.3.2 Impact Severity Measures

Kinematic measures of the head are most commonly used to assess brain injury, as they are thought to be indicative of the mechanical response of the brain. The development of criteria that estimate head injury date back to the early 1950s. Two head injury indexes have been adopted as the standards for determination of head injury: The Head Injury Criterion and The Gadd severity index. Both indexes are functions of acceleration and require the use of highly accurate accelerometers placed within the head of anthropomorphic test devices (ATDs).

4.3.2.1 Head Injury Criterion

The Head Injury Criterion (HIC) was initially developed for the auto industry to quantify brain injury and was based on the linear acceleration of the head [114-118]. The HIC is calculated as,

$$HIC = (t_2 - t_1)\left[\frac{1}{(t_2 - t_1)}\int_{t_1}^{t_2} a(t)\,dt\right]^{2.5} \quad (0\text{-}1)$$

where a(t) and t represents the linear acceleration at the head's center of mass (measured in g) and the time which maximizes the expression respectively. The criterion was developed to measure the rate of kinetic energy change while determining the average value which results in injury [118]. Automotive Federal regulations require that the HIC does not exceed 1000 however, the threshold for concussion is even lower with some research suggesting a HIC of 615 ± 309 results in a concussion [119].

4.3.2.2 Gadd Severity Index

The Gadd severity index [120] was developed after the HIC as a generic head injury index. Its derivation is similar to the HIC but has been simplified for easier calculation. The Gadd severity index is calculated as,

$$I_{Gadd} = \int a^{2.5}\,dt \quad (0\text{-}2)$$

where: a and t represent the acceleration and time respectively. In 1973 NOCSAE adapted the Gadd index to create standards in football helmet performance. NOCSAE adjusted the index by limiting the time integration interval to periods when the acceleration exceeds 10g. The current

NOCSAE standard for newly manufactured football helmets states that the peak Gadd severity index of any impact shall not exceed 1200 SI [121]. The Gadd severity index wasn't intended to be used to determine if one received a concussive blow, but rather determine if that blow would cause loss of life.

4.3.2.3 Linear and Angular Acceleration

To accurately measure the effects of acceleration on the human body in car impacts, General Motors developed an anthropomorphic test dummy called the Hybrid III. The Hybrid III headform mimics human geometry, weight, inertia, and biomechanical response to impact, while measuring triaxial acceleration at the head's center of gravity [122]. The head acceleration traces recorded by the Hybrid III ATD are used to calculate the HIC, Gadd Severity index, and the peak accelerations for all impacts.

4.3.3 Equipment

In this study, a standard Riddell 360 football helmet was modified to accommodate eight NCF sensors throughout the inner surface of the helmet (Figure 4-3). Each Riddell 360 helmet is comprised of an outer shell and 3 inner foam liners: the front, top, and one piece that surrounds the rest of the head. The foam liner has inner "head side" and outer "helmet side" foam pads. Both the inner and outer foam pads are contained in a plastic liner with an additional plastic film that separates the inner foam from the outer foam. Eight separate pieces of the inner foam on the front, sides, and top, were removed by cutting the plastic liner and removing and replacing them with NCF sensors with similar energy absorption characteristics of the same size and shape (Figure 4-4). The inner foam was selected as it is in direct contact with the head and would

provide the most direct measure of the head during impact. All NCF sensors were individually connected to one central data acquisition device.

Figure 4-3: Football helmet instrumented with eight NCF sensors which replaced existing helmet padding.

All NCF sensors were attached to a National Instrument NI 9234 high accuracy data acquisition module, sampled at the Nyquist frequency of 1650 Hz. Previous frequency response testing of the NCF demonstrated that the highest frequency of interest in the NCF response is 800 Hz. The NCF sensors were connected to the NI 9234 module using 14 AWG shielded wire and connected with BNC connectors directly to the DAQ to reduce signal noise during acquisition. All data was recorded through a custom LabVIEW script with each recording representing an individual impact event. All drop tests were performed on a NOCSAE approved twin-wire guide, carriage assembly with a NOCSAE approved headform instrumented with a 3-2-2-2 head accelerometer array [123]. All acceleration data was collected from the tri-axial accelerometer at the headform's center of mass at a sampling rate of 20 kHz. Additionally, the drop tower and accelerometer array were properly calibrated per NOCSAE standards prior to testing.

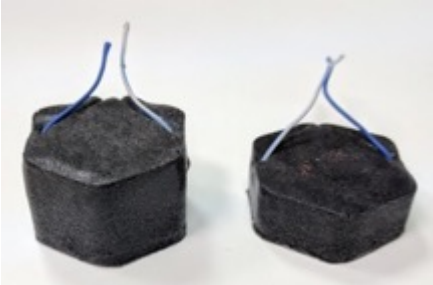

Figure 4-4: Nano Composite Foam helmet sensors used in this study. The sensors replaced a portion of the foam in the helmet to create a sensing helmet.

4.3.4 Star Testing

The Virginia Tech STAR testing procedure [106] attempts to recreate impacts that represent the hits that an average player experiences during a season of play. The test is conducted by dropping the helmet on 4 locations (front, rear, right-side, and top) from five different heights (12, 24, 36, 48, and 60 inches). All tests were performed with increasing heights at each location starting with the front followed by rear, side, and top, for a total of 20 tests [106]. The voltage response from the NCF sensors, as well as the acceleration data, were recorded for each drop test for a total of 20 tests. Both data sets were recorded with separate acquisition systems, which required synchronization afterwards.

4.3.5 Data Analysis

All data were collected and stored on an individual impact basis with both the acceleration and NCF data maintaining the same naming convention for later correlation. The impact velocity, impact energy, and severity index for each impact were calculated from the drop height, weight, and resultant acceleration traces respectively. As all tests were performed on a drop

tower, the helmet will experience an initial impact with subsequent bounces. All NCF data were trimmed to 120 milliseconds to account for the entire compression and recovery of the foam during the initial impact. The acceleration was limited to 30 milliseconds as the response only accounts for the impact and does not have a recovery time. The NCF signal was recoded for a longer duration to measure the entire response, initial impact, and recoil.

An example response from all NCF sensors during a typical 60-inch drop test is shown in Figure 4-5. The voltage response can be separated into different portions of interest. The initial spike occurs when the headform compresses or releases the padding inside the helmet upon impact, and the subsequent spikes occur when the headform recoils. The remaining positive and negative spikes occur as the headform continues to recoil in the helmet before coming to rest. Figure 4-5 shows the rear sensors, which are initially compressed, exhibiting a positive voltage

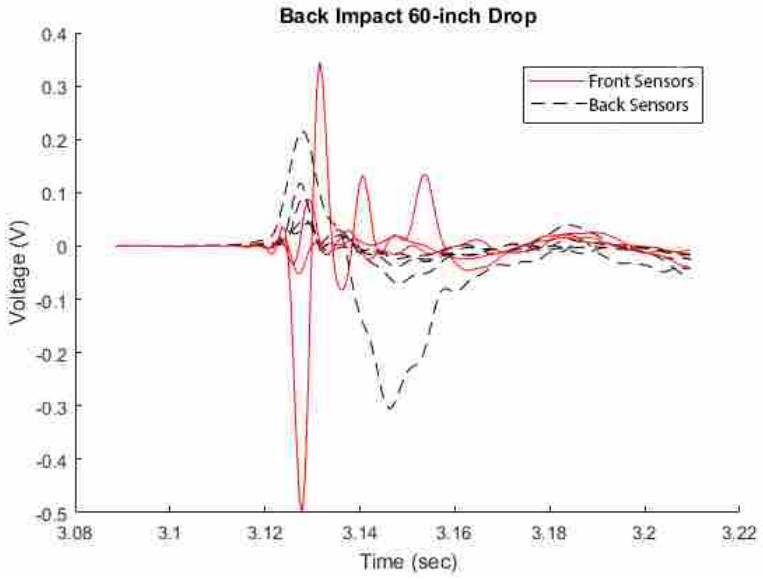

Figure 4-5: Sample voltage response from all NCF sensors to 60-inch rear helmet drop test. This signal shows a positive response from all the rear sensors while the front sensors show an opposite response.

response while the front sensors, which are initially decompressed, exhibit a negative voltage response. All 3D acceleration data were post processed by Virginia Tech to filter out noise, remove subsequent bounces, and converted to a resultant acceleration. Figure 4-6 shows a typical resultant acceleration trace from a 60-inch impact.

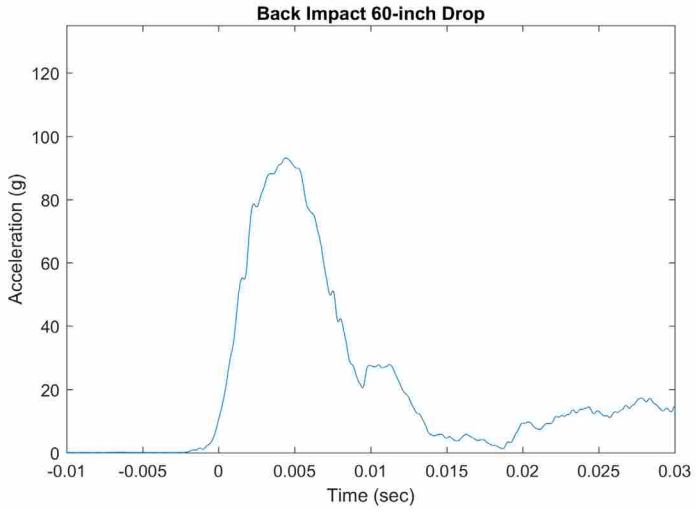

Figure 4-6: Sample resultant acceleration trace from tri-axial accelerometer in testing head form.

The NCF sensor data, sampled at 1652 Hz, were filtered with a 5th order Butterworth low-pass filter with a cutoff frequency of 200 Hz. The cutoff frequency was selected by inspecting the FFT of the signal surrounding the peaks. Additionally, the long wires used in the test setup introduced some higher frequency noise during impacts which were filtered out with the selected cutoff frequency. The headform acceleration data, sampled at 20 kHz, were filtered with a 2nd order phaseless Butterworth low-pass filter with a cut off frequency of 1650 Hz as per SAE J211 specification. The 3D acceleration data was then converted to a resultant acceleration, which was used for all calculations.

4.4 Results

This study evaluated the accuracy of a helmet instrumented with eight separate NCF sensors at measuring the magnitude of impact. The helmet was tested with 20 separate drops following the STAR testing procedure. The helmet was dropped on four locations from five different heights. The NCF signal was correlated to the standard measures of impact and each will be evaluated below.

4.4.1 Statistical Analysis

Multiple regression was performed showing that NCF sensors can be used to predict the impact severity measures of interest including: severity index (SI), head injury criterion (HIC), maximum acceleration (MA) and impact energy (IE). Other studies that have evaluated impact severity have measured impact forces [124], however due to the interdependency of acceleration and force this paper will focus on the acceleration based measures. After examining many characteristics of the NCF signal (voltage integral, FFT frequencies, distance between peaks, etc.) it was found that peak NCF response was both most significant as well as easiest to extract. We considered models using the measured peaks for the NCF sensors located in the front (F), left (L), back left (BL), back (B), back right (BR), right (R), top front (TF), and top (T) of the helmet. For each of the impact severity measures, the squared multiple correlation coefficient R^2 based on all 8 predictors is between 0.91 and 0.94. However, to minimize the potential of overfitting the data, we consider the predictive ability for subsets of the predictors. Subsets of predictors and the R^2 for predicting each impact severity measure is given in Table 4-1. Note that because our training data includes drops on the right side of the helmet, we tend to include more of the NCP sensor peaks from the right side of the helmet. The model with the best fit, as determined by R^2 and Root Mean Squared Error (RMSE), is the model with five sensors (F, B,

BR, R and TF). The best subset of three sensors includes the BR, R, and FT sensors with R^2 values between 0.84 and 0.87. However, using a more geographically balanced set of three sensors (L, R, and FT) still yields R^2 values between 0.79 and 0.88, with the severity index being the only measure with substantially diminished predictability. Note that even using a model with only two predictors yields R^2 values between 0.76 and 0.87. Thus, we have compelling evidence for the relationship between the NCP sensors and the accuracy of several measures of impact severity.

Table 4-1**:** R2 values and RMSE, in parentheses, for predicting each of the different impact severity measures.

	Variables Included in Predictive Model				
Response Variable	All 8 NCP Peaks	F, B, BR, R, and TF	BR, R, and TF	L, R, and TF	R and TF
Gadd Severity Index	0.91 (54.90)	0.91 (49.68)	0.85 (58.94)	0.79 (71.08)	0.76 (73.78)
Head Injury Criterion	0.93 (27.90)	0.93 (26.37)	0.88 (31.75)	0.74 (46.34)	0.69 (49.03)
Maximum Acceleration	0.94 (8.88)	0.94 (7.91)	0.87 (10.44)	0.88 (9.95)	0.87 (10.29)
Impact Velocity	0.92 (.42)	0.88 (.43)	0.84 (.48)	0.85 (.46)	0.84 (.47)
Impact Energy	0.92 (11.32)	0.90 (10.95)	0.85 (12.9)	0.85 (12.72)	0.85 (12.7)

Many of the previous or existing impact systems referenced in this paper determine the direction of the impact in addition to the impact severity measures. Some models use impact location as an input to their models for added accuracy. During testing the NCF equipped helmet was dropped on four locations: the front, right back and top. Discriminant analyses were performed using the peak voltage values from all eight NCF sensors. Two different methods were used: k-nearest neighbors (KNN) with k=5 and linear discriminant analysis (LDA). Using hold-one-out cross validation, 0% and 5% misclassification rates were obtained with KNN and LDA, respectively.

A confusion matrix demonstrates the fit of a prediction by showing all the predicted locations vs actual locations. A perfect model will only contain numbers along the diagonal of

the table; if there are numbers outside of the diagonal they represent improper predictions. The resultant confusion matrix from k-nearest neighbors model would only have values in the diagonal of the matrix. The discriminant analysis confusion matrix is shown in Table 4-2 with 1 out of 20 locations incorrectly predicted (shown in red). The model predicted a front impact once when it was a back impact. Predicting the opposite side of impact can be explained by the headform compressing the NCF sensors on the side of impact and then recoiling to the opposite side, resulting in a measure on both sides of the helmet. This analysis only evaluated peak NCF response, independent of time. It is expected that future analysis or algorithms would account for time differences between peaks, further increasing the accuracy.

Table 4-2: Confusion Matrix demonstrating predicted impact location vs true impact location.

		Predicted Condition			
		Front	Right	Back	Top
True Condition	Front	5	0	0	0
	Right	0	5	0	0
	Back	1	0	4	0
	Top	0	0	0	5

4.5 Discussion

The purpose of this study was to evaluate the use of NCF sensors in a football helmet in measuring location and quantifying severity of impacts. A study by Guskiewicz *et. al* highlights the discrepancies between many of the acceleration-based determinations of concussions [125]. Furthermore, many different acceleration thresholds have been proposed that do not necessarily correlate with actual head injuries. This paper proposes a new method of quantifying the severity

of impacts while also reporting the standard measures used in the field. The NCF sensors were effective in determining both the location and severity of impacts, correlating well with the measurements taken by the accelerometer inside the testing headform. A total of 20 drop tests were performed using the STAR testing method, impacting on the four sides of the helmet. Predictions of impact severity, max acceleration, impact energy, impact velocity, and location of impact, all obtained an R^2 of 90% fit or better. This overall accuracy is considerably higher than several existing consumer products and provides evidence that NCF sensors are a viable solution for real time impact measurement in helmets. Helmet manufacturers would simply place several NCF sensors in lieu of standard foam and measure their response with a microcontroller. As the NCF is self-powered, the microcontroller system would require little power to monitor helmet activity.

The standard measurement systems on the market today directly measure the acceleration of the helmet through accelerometers and then use that to calculate the severity indexes and the maximum acceleration of the player's head. The measure of acceleration can be erroneous when the helmet, mouth guard, etc., are dropped, or otherwise removed from the player during play. Furthermore, helmet-based accelerometer systems have been shown to measure different accelerations from what the head actually experiences. Some studies have shown that improper helmet fit can reduce accuracy by more than 15% [105]. The NCF sensors measure impact when they are compressed, which could result in lower false impact measures and higher accuracy than competing acceleration-based systems. Ultimately, the accelerometer and gyroscope systems could be combined into the electronics that measure the NCF sensors to create redundancy and adding new measurements to the helmet-based impact system.

In addition to correlating well with acceleration-based metrics of head impacts, the NCF sensor response relates directly to the interactions between helmet shell and head, potentially providing a truer indication of the impact experienced by the head. Some of the first models created to predict concussions were based on linear acceleration alone. Subsequent models combined multiple measures of acceleration, thereby increasing the accuracy of the concussion model. Future concussion models could include measures of impact energy and velocity to further increase accuracy.

This NCF based sensor system proved to be accurate in measuring standard impact metrics (e.g. peak acceleration, Gadd Severity index and HIC) while also providing additional details (e.g. impact velocity and impact energy) that were previously difficult to obtain. The NCF sensors can measure max acceleration, impact velocity, impact energy, severity index, and impact location with 90% or better accuracy, with a foam product similar to that which is already designed into all football helmets. New manufacturing methods have been developed since this study, which reduce the difficulty in manufacturing the NCF. These newer methods increase the consistency between sensors while also providing a sheet foam product which is commonly used in helmets. Future work will include the use of these newer NCF sensors and live testing. It is expected that with different head shapes, helmet sizes and impact scenarios more than just the NCF peak will be used to create more complex and accurate models.

4.6 Acknowledgments

This material and research are based upon work supported by the National Science Foundation under grant numbers CMMI-1538447 and IIP1549719. All helmet testing was

performed at Virginia Polytechnic Institute and State University's Biomedical Engineering and Mechanics helmet testing lab

5 USING NANOPARTICLES AND SHORT FIBERS TO INCREASE THE ENERGY ABSORPTION OF FOAMS

5.1 Abstract

Polymeric foams have been widely used in applications where high energy absorption and low weight are key design considerations. The lattice of cell walls in the foam absorbs energy by going through large deflections of thin membranes. The entrained air bubbles have the additional benefit of decreasing the overall density of the material. When nanoparticles and short fibers are added, this not only directly reinforces the cell walls and increases strength and stiffness, but it also facilitates nucleation of gas bubbles during the cure process, which decreases cell size and further increases strength and stiffness. To better characterize how fibers and nanoparticles increase the strength and energy absorption of foams, several different foams were created by varying the polymer base and the nanoparticle additives. Quasi-static compression tests were performed on these foams, and the data was analyzed for energy absorption up to the densification part of the stress strain curve. The results show that adding nickel coated carbon fibers (NCCFs) can significantly increase the energy absorption ability of the foam, while nickel nanoparticles (NiNs) had less of an effect. The reinforcement received from NCCFs increases with increasing fiber length for a given additive percentage. These results help clarify which nanoparticles and additive amounts are desirable for reinforcing foams, and also the limitations of reinforcing foams with nanoparticles and short fibers.

5.2 Previous Work in Reinforcing Foams with Small Particles

Several papers have been published on the potential for improvement of the performance of polymeric foams by the addition of nanoparticles and short fibers, but not all results have been positive, and researchers sometimes disagree about what it is that produces the improvements. Experiments using short fibers or nanoparticles found that the cell size in the foams that included the additives were drastically reduced compared to pure foams. Researchers in these studies attributed this to an increased gas and bubble nucleation rate. Since adding nanoparticles and fibers adds a large amount of surface area per unit volume of added particulate, this increased surface area should act as a driving force to increase the nucleation of cells, directly leading to the smaller cell size observed [126, 127]. However, Mahfuz, who fabricated polyurethane foams embedded with nanoparticles such as Silicon Carbide and Titanium Oxide, found that the cell size was increased by the introduction of nanoparticles, and most particularly by the introduction of Titanium Oxide. Despite this difference in the morphology of the foam, the nanoparticles still increased the strength and stiffness of the foam by 50-70% [128].

In addition to strengthening due to reduced cell size, strengthening of polymeric foams by nanoparticles and short fibers has been attributed to the additives congregating in the walls of the cells, leading to increased resistance to crack propagation [126-128]. Fibers and nanoparticles yield the greatest strength increase when the particles or fibers are able to be directly bonded, rather than being simply wetted by the matrix [127]. The change in specific strength with short fiber additives was different for each formulation of the foam, with a small number of foams actually exhibiting a decrease in performance with the additives, highlighting the need to analyze each formulation specifically instead of assuming that adding fibers or nanoparticles will also increase strength. To fully take advantage of the improvements offered by nanocomposite foams

the additives need to be mixed in very thoroughly, which can pose challenges to preparing the foam [126, 127, 129].

While researchers disagree about the mechanics behind the increased performance of these nanocomposite foams, it is clear that the area shows great potential for high performance materials. In another study, the mechanical properties of short fiber reinforced phenolic foams are assessed, comparing them to conventional foams. The fibers used in this study were aramid and glass fibers. The aramid fiber reinforced foams showed significantly lower friability (the tendency of a foam to disintegrate when rubbed or tumbled), higher resistance to cracking, and more isotropic behavior, while glass fiber-reinforced foam was found to be significantly stiffer and stronger than unreinforced foam. This study did not account for fiber length, orientation, or dispersion, and also neglects to consider fiber/foam interfacial adhesion [130]

Another frequently studied effect on polymeric foams by the addition of nanoparticles and nanofibers is the increase in fracture toughness. Studies have compared several different nanoparticles of varying sizes, such as Titanium Oxide, nanoclay, carbon nanofibers, and multiwall carbon nanotubes. It has been found that the presence of the nanoparticles and fibers generally made the foams cells smaller and more resilient to crack propagation, but more especially with small fibers of high aspect ratio with length long enough to bridge the crack propagation gap [129, 131]. Studies which vary the amount of doping through a range of weight percentages are particularly valuable, since they show how much material must be added to gain a desired property. Thus it is possible to find the ideal amount of doping required to get maximum strengthening of the foam from each additive, and compare across additives to determine which increased the toughness the most [129, 131].

All of these studies contribute to a case that nanocomposite foams are a promising class of material, but so far very few have looked specifically at energy absorption through the elastic and compaction regimes. Zeng studied a sponge's ability to absorb more energy with carbon nanotubes embedded. Although this isn't an exact parallel, because it is a sponge and not a foam, it shows that there is an interest in using embedded nanoparticles to increase energy absorption. The sponges that were made were not homogeneous composites but rather layers of sponge sandwiching a layer of upright carbon nanotubes. Zeng found that the composite formed was capable of greater energy absorption than either constituent material alone [132].

Further research in this area is clearly needed, as nanocomposite foams have been shown to provide increases in strength, stiffness, fracture toughness, and durability, however it has yet to be verified that they provide a great performance increase in elastic energy absorption capability up to the densification regime. Such an improvement would be of great value for a variety of potential applications, such as energy absorbing automobile structures, protective clothing, noise and vibration control, athletic equipment, fracture resistant structures, and multifunctional materials [129].

5.3 Methods

The material properties varied and measured in this experiment were the porosity (% air by volume) of the foam, the weight percent of each type of nanoparticle and the energy absorption capability of the foam up to the densification region. An optimal foam is light, absorbs large amounts of energy, and is inexpensive. Energy absorption is often normalized by porosity to give the energy absorption per mass of a given foam. Since the nanoparticle additives form a

relatively high percent of the cost of the foam, those which give the greatest performance for the amount of additive present are of particular interest.

Quasi-static compression tests were performed to understand the relationship between energy absorption and nanoparticle reinforcement of the foam. A set of 24 foam samples were prepared and used in these tests. Each sample measures 66 mm x 35.7 mm x 12 mm. 14 samples were made from a polyurethane foam and the other 10 were a silicone foam. The composition of each sample is detailed in Table 5-1 and Table 5-2.

Table 5-1: Silicone foam sample weights and compositions.

Sample	Weight (g)	Porosity (% Air)	Nanoparticle (% Weight)
1	18.17	48.29	12
2	17.19	51.08	12
5	17.47	59.16	22
6	17.32	56.2	22
9	17.14	55.13	17
10	17.75	55.51	17
13	16.27	55.1	12
14	16.25	56.54	12
17	16.51	53.23	22
18	17.37	51.57	22

.The samples were originally prepared through a design of experiments (DOE) in which each of 5 factors had a high and a low state. These factors were Foam Type, NiNs concentration, NCCF concentration, length of NCCFs, and whether the NiNs were screened beforehand to break up clumps. This would have resulted in a set of 32 samples, however those with high

concentrations of both NiNs and NCCFs were found to react unfavorably, failing to form a cohesive foam due to insufficient matrix material.

Table 5-2: Polyurethane foam sample weights and compositions.

Sample	Weight (g)	Porosity (% Air)	Nanoparticle (% Weight)
3	14.35	59.16	12
4	15.39	56.2	12
7	17.47	55.13	22
8	17.32	55.51	22
11	17.48	55.1	17
12	16.92	56.54	17
15	17.14	53.23	12
16	17.75	51.57	12
19	15.01	59.04	17
20	13.99	61.83	17
21	16.27	53.7	-
22	16.25	53.75	-
23	15.26	56.57	-
24	14.82	57.82	-

The samples tested were based on A-3240 platinum silicone foam from Factor II, Inc. and AFX-20655 polyurethane foam from Utah Foam Products. Since the foam types were not randomly selected we cannot infer quasi-static energy absorption to all types of silicone and polyurethane foam. However, the foams were randomly assigned and so causation inferences can be drawn on these two foams. Once a statistical analysis of the effect of the foam type on energy absorption is done, further attention will be given to the polyurethane foam as it is a more common foam in industry and is less expensive.

5.3.1 Quasi-Static Compression Tests

Compression tests were performed to determine the stress-strain relationship of each sample. Nominal compressive stress was calculated by:

$$\sigma = \frac{F}{A} \tag{5-1}$$

where F is the force on the foam sample and A is the initial surface area in contact with the load cell. (Load cell area: 24.88 mm x 49.8 mm). The nominal strain was calculated as:

$$\varepsilon = \frac{(t_0 - t)}{t_0} \tag{5-2}$$

where t_0 is the initial sample thickness and t is the thickness of the foam which varies during the compression test.

Compression testing was performed at 20 ºC at a strain rate of 0.002/sec. Results are shown in Figure 5-1 with compressive stress (MPa) on the vertical axis and strain on the horizontal axis. Compression testing was performed up to 60% strain or 2000 N of compressive

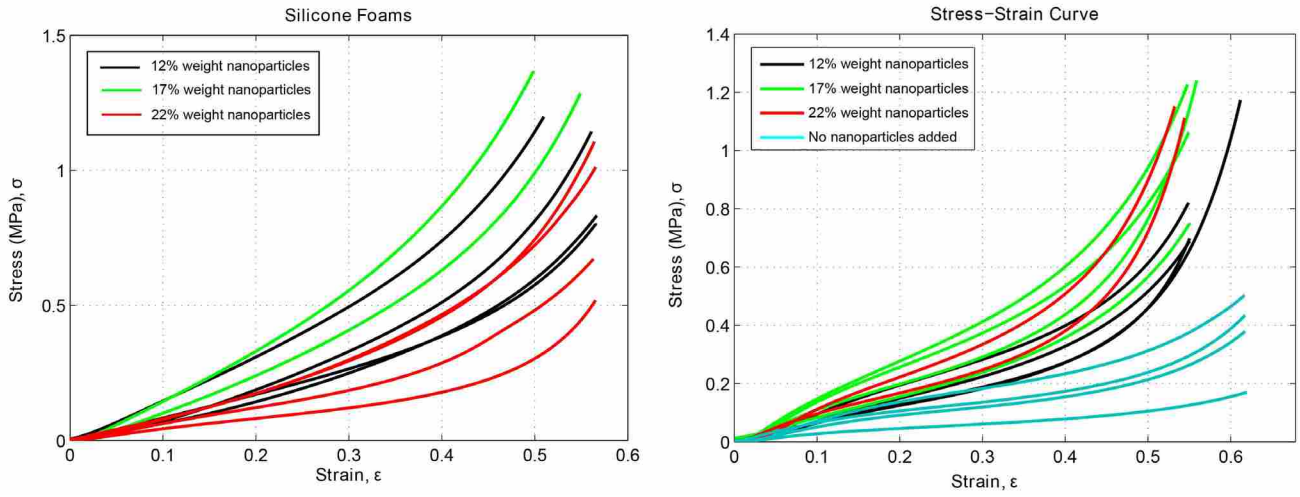

Figure 5-1: Stress strain curves for silicone foam (left) and polyurethane foam (right) corresponding to the samples described in Table 5-1 and Table 5-2.

force, whichever occurred first. This allowed testing through the elastic, plateau, and densification regions for the foam.

Density of the foam samples was measured using the mass and volume of the block of foam. A value for energy absorption was calculated by taking the second derivative of the smoothed stress-strain curve, and halting integration of that curve when

$$\frac{d^2 Energy}{d\epsilon^2} \geq 175 \frac{kJ}{m^3} \tag{5-3}$$

signifying the onset of the densification regime. Preliminary analysis shows that the energy absorbed by each sample in quasi-static testing is approximately linear with porosity for a given composition, and so normalizing based on porosity is useful for differentiating between different foam compositions of different porosities. This helps to focus on the effects of the fillers and eliminates some of the noise due to variation in porosity that occurs during manufacturing. Data from these calculations and from measurements described were then used to compare the ratio of

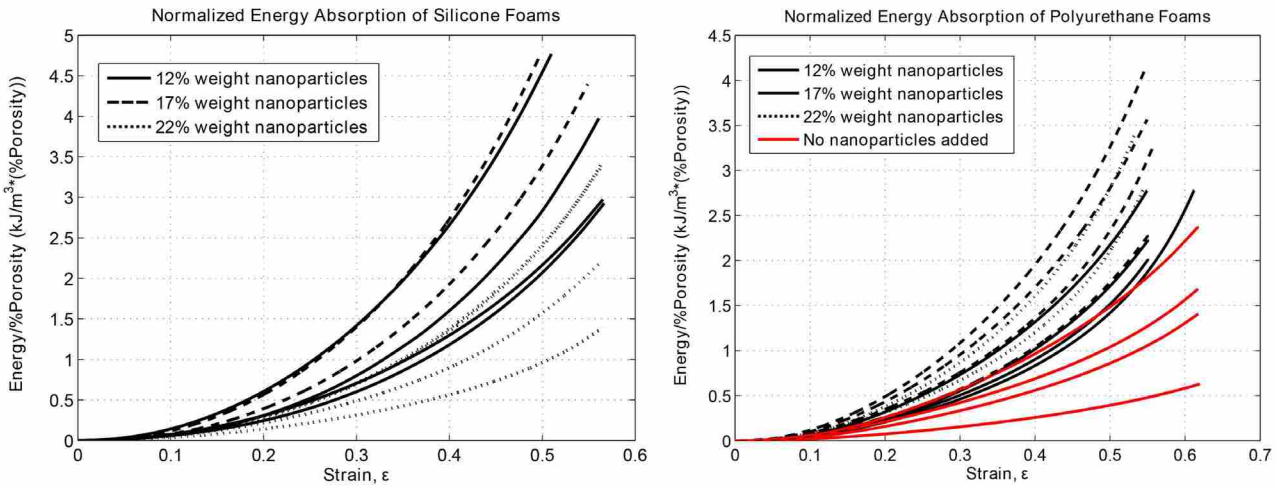

Figure 5-3: Energy absorption test results for silicone foam (left) and polyurethane (right) with varying amounts of nanoparticles, the composition of which can be found in Table 5-1 and Table 5-2.

energy absorbed to the percentage of nanoparticles in each foam, for a given foam density. This comparison is illustrated in Table 0-2 found in Appendix A.

5.4 Results

The data shows that the median total quasi-static energy absorption of polyurethane foam was lower than the median total quasi-static energy absorption of silicone foam, even after the effects of porosity are accounted for, with a two-sided p-value of .002. The median total quasi-static energy absorption of polyurethane foam was estimated to be only 39% that of the silicone foam with no added nanoparticles, after accounting for the variables mentioned above (Appendix A Table 0-1). However, the data also provide evidence that there is a difference in slope of total energy absorption, with respect to porosity, between the two types of foam (two-sided p-value of .07). The equations for polyurethane and silicone that show the estimated energy absorption of each type of foam with respect to porosity are given respectfully as:

Polyurethane $$Energy_{max} = 3.58x10^5 - (3.73x10^5) * (\%Porosity) \quad (5\text{-}4)$$

Silicone $$Energy_{max} = 9.31x10^5 - (1.4x10^6) * (\%Porosity) \quad (5\text{-}5)$$

Porosity affects the energy absorption of silicone foams much more than polyurethane foams, with each percent of porosity having about 3.74 times the effect on energy absorption in silicon than polyurethane and maintaining max quasi-static energy absorption with higher percentage porosities for the range of porosities measured in this experiment. Further information on this statistical analysis can be found in Table 0-3 in Appendix A.

To study the effects of the nanoparticles on the foam, only the polyurethane foams were included in the final statistical analysis so that the effect of the nanoparticles would not be

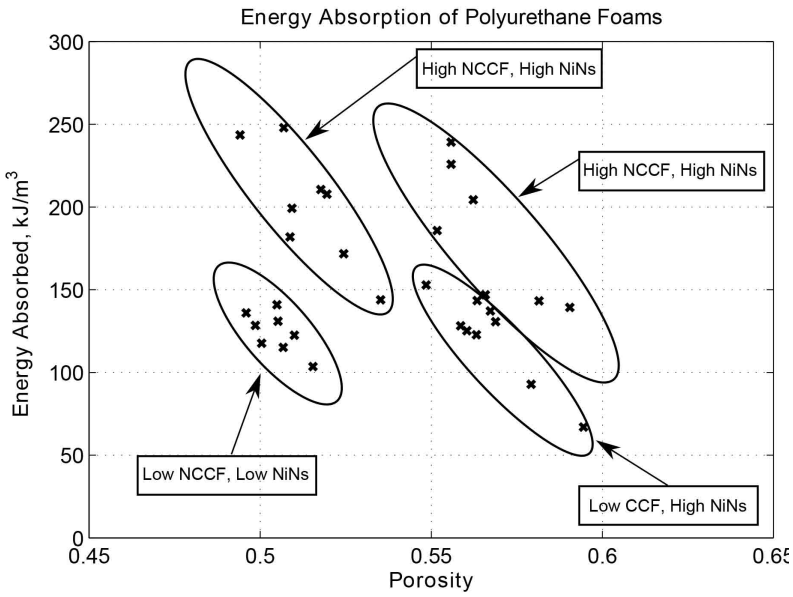

Figure 5-4: A subset of data points from Figures 1 and 2 showing the discrete energy absorption values and the grouping that occurs based on nanoparticle composition.

overshadowed by the differences in the foam. The data is summarized in Figure 5-3. From this it is immediately clear that while adding NCCFs leads to a very significant increase in energy absorption, adding NiNs causes a change in the reaction of the polymer, which leads to higher porosity. The multiple regression analysis showed the NiNs effect confounded the results and was therefore left out in further analysis. Screening the NiNs had no statistical significance on the energy absorption.

A separate model was created to determine whether longer NCCF, NCCF loading or porosity correlated with higher energy absorption. The resulting analysis shows that there is a trend toward higher energy absorption with longer fibers, higher NCCF content and lower porosity (Appendix A -Table 0-4). The data provides convincing evidence that the max quasi-static energy absorption of the polyurethane foam is dependent upon the NCCF %, NCCF

Length, and the porosity (p-values of <0.0001, 0.0039 and 0.003 respectively). The estimated maximum quasi-static energy absorption can be estimated by the following equation:

$$Energy_{max} = 264{,}997 + 15{,}912 * NCCF(\%) + 36{,}908 * NCCF(length) \ [J/m^3 \quad (5\text{-}6)$$

This estimate is based on NCCF length from 0 to 1 mm and from 0 to 7% by weight NCCF. The statistical data for an analysis of NCCF content alone, and for NCCF content, length and porosity are available as Table 0-3 and Table 0-4 in Appendix A.

5.5 Discussion

When nanoparticles and short fibers are added to reinforce NCPF they are able to absorb more energy than non-reinforced foams in a quasi-static environment. The effect of porosity, NCCF% and NCCF length were significant both statistically and practically. The results show that adding NCCFs can significantly increase the energy absorption of the foam, while NiNs had less of an effect. Screening or sifting the NiNs before mixing them in the resin was shown to have no statistically significant effect on energy absorption. These results help clarify which nanoparticles and additive amounts are desirable for reinforcing foams and the limitations of reinforcing foams with nanoparticles and short fibers.

6 CONCLUSION

The development and subsequent use of NCPF sensors is well documented throughout this dissertation. The NCPF sensors are shown to support the triboelectric generation theory wherein additive triboelectric affinity and surface area contribute to increased electrical response. Two additives were selected as the top performers in accuracy and repeatability, F104 graphite and nickel powder. Their electrical response had the strongest linear and categorical correlation with impact energy throughout all levels of loading with average R-squared correlations exceeding 0.7 and 0.8 for each respectably. The results from this analysis can be used to increase sensor performance by selecting additives that provide accuracy and response magnitude desired. A basic understanding into how different additive's base material, surface area, geometry and size change the signal has been established, laying the foundation for fine tuning the NCPF sensors moving forward. Furthermore, the results from this and future work can now be directly compared when the input impedance of the DAQ is known and ideal circuits can be designed to . The linear correlation between input impedance and measured response allows for easy adjustment to the signal for different applications.

NCPF sensors have been shown to provide one-dimensional spatial location information for impacts on a single sensor. Accurate results are dependent upon proper calibration of the sensor which includes NCPF volume, base foam material properties and the electrical circuit design. An ideal electrode design for a spatial location system in one dimension was found to have electrodes 6.5 mm wide with a probe-to-sensor area ratio of 20%. These results can be directly applied to more complex systems or higher dimensions. These capabilities allow for

diverse application of the NCPF sensors in biomechanical systems where impact information is critical.

NCPF sensors have been shown to provide a viable alternative method of measuring impacts in a football helmet. NCPF based sensor system proved to be accurate in measuring standard impact metrics (e.g. peak acceleration, Gadd Severity index and HIC) while also providing additional details (e.g. impact velocity and impact energy) that were previously difficult to obtain. The NCF sensors can measure max acceleration, impact velocity, impact energy, severity index, and impact location with 90% or better accuracy, with a foam product similar to that which is already designed into all football helmets.

Future work is needed on further electrical model development, and additional foam functionality. The NCPF material has been developed and refined a great deal throughout the course of this dissertation but has been limited mostly to a phenomenological evaluation. Future work could focus on the true electrical model of the foam to enable prediction of response with known loading and impact characteristics. Until such a model is created all correlations are based solely on observation and require calibration for each new density, formula and dimension. Initial testing has been carried out and shown that the foam can provide a dual electrical response to impacts and pressure. The dual response would allow for increased utility and functionality in applications like shoes where the weight and impacts are both important. Lastly, the energy harvesting capabilities of the material have only been initially evaluated remain to be further characterized. There is an ever-increasing number of wearable devices and most all of them require frequent charging. If a material such as NCPF could generate sufficient current to charge the device, or subsidize the power used to measure its response it would provide new opportunities to evaluate biomechanical interactions like never before.

REFERENCES

[1] Calkins, T. B., Fullwood, D. T., Ghosh, S., Hyatt, T. B., Johnson, O. K., Hansen, N., and Hansen, G., 2010, "Applications for a Nano-composite High Displacement Strain Gauge," SAMPESalt Lake City.

[2] Remington, T. D., Merrell, A. J., Stolworthy, D. K., McArthur, D., Fullwood, D., Bowden, A., and Hansen, N., 2013, "Biomechanical applications of nano-composite strain gauges," SAMPELong Beach, CA.

[3] Koecher, M., Yeager, J. D., Park, T., Fullwood, D., Colton, J. S., Mara, N., and Hansen, N., 2013, "Characterization of Nickel Nanostrand Nanocomposites Through Dielectric Spectroscopy and Nanoindentation," Polym Eng Sci, 53(12), pp. 2666-2673.

[4] Johnson, O. K., Gardner, C. J., Fullwood, D. T., Adams, B. L., Hansen, N., and Hansen, G., 2010, "The colossal piezoresistive effect in nickel nanostrand polymer composites and a quantum tunneling model," Computers, Materials, & Continua, 15(2), pp. 87-112.

[5] Hansen, N., Adams, D. O., and Fullwood, D. T., 2015, "Evaluation and Development of Electrical Conductivity Models for Nickel Nanostrand Polymer Composites," Polym Eng Sci, 55(3), pp. 549-557.

[6] Koecher, M. C., Pande, J. H., Merkley, S. S., Henderson, S., and Fullwood, D. T., 2012, "Evaluation of nickel nanostrands as strain sensors in CFRP," SAMPEBaltimore, MD.

[7] Bilodeau, R. A., Fullwood, D. T., Colton, J., Yeager, J. D., Bowden, A. E., and Park, T., 2015, "Evolution of Nanojunctions in Piezoresistive Nanostrand Composites," Composites Part B: Engineering, 72, pp. 45-52.

[8] Johnson, O. K., Kaschner, G. C., Mason, T. A., Fullwood, D. T., Hyatt, T., Adams, B. L., and Hansen, G., "Extreme piezoresistivity of silicone/nickel nanocomposite for high resolution large strain measurement," Proc. TMS 2010.

[9] Johnson, O., Kaschner, G., Mason, T., Fullwood, D., Adams, B., and Hansen, G., 2011, "Optimization of Nickel Nanocomposite for Large Strain Sensing Applications," Sensors and Actuators A, 166, pp. 40-47.

[10] Gardner, C. J., Johnson, O., Fullwood, D. T., Hansen, G., and Adams, B. L., "Piezoresistive Effect in Nickel Nanostrand - Polymer Composites," Proc. TMS.

[11] Koecher, M. C., Pande, J. H., Merkley, S., Henderson, S., Fullwood, D. T., and Bowden, A. E., 2015, "Piezoresistive in-situ strain sensing of composite laminate structures," Compos Part B-Eng, 69, pp. 534-541.

[12] Johnson, T. M., Fullwood, D. T., and Hansen, G., 2012, "Strain monitoring of carbon fiber composite via embedded nickel nano-particles," Compos Part B-Eng, 43(3), pp. 1155-1163.

[13] Johnson, O., Gardner, C., Fullwood, D., Adams, B., Hansen, G., and Kalidindi, S., 2009, "Textures of Dispersion of Nickel Nanostrand Composites, and Modeling of Piezoresistive Behavior:," MS&TPittsburgh.

[14] A. Jake Merrell, W. F. C., Matthew K. Seeley, Anton E. Bowden, David T. Fullwood, 2017, "Nano-Composite Foam Sensor System in Football Helmets," Annals of Biomedical Engineering.

[15] Bird, E. T., Merrell, A. J., Anderson, B. K., Newton, C. N., Rosquist, P. G., Fullwood, D. T., Bowden, A. E., and Seeley, M. K., 2016, "Vibration monitoring via nano-composite piezoelectric foam bushings," Smart Mater Struct, 25(11).

[16] Rosquist, P. G., Collins, G. Q., Merrell, A. J., Tuttle, N. J., Tracy, J. B., Bird, E. T., Christensen, W. F., Bowden, A. E., Fullwood, D. T., and Seeley, M. K., 2017, "Measurement of 3D Ground Reaction Force using Nanocomposite Piezo-Responsive Foam Sensors during Walking," Annals of Biomedical Engineering.

[17] Lin, L., Hu, Y. F., Xu, C., Zhang, Y., Zhang, R., Wen, X. N., and Wang, Z. L., 2013, "Transparent flexible nanogenerator as self-powered sensor for transportation monitoring," Nano Energy, 2(1), pp. 75-81.

[18] Wang, Y. R., Zheng, J. M., Ren, G. Y., Zhang, P. H., and Xu, C., 2011, "A flexible piezoelectric force sensor based on PVDF fabrics," Smart Mater Struct, 20(4), p. 045009.

[19] Souri, H., Nam, I. W., and Lee, H. K., 2015, "A zinc oxide/polyurethane-based generator composite as a self-powered sensor for traffic flow monitoring," Composite Structures, 134, pp. 579-586.

[20] Hwang, H. Y., 2011, "Piezoelectric particle-reinforced polyurethane for tactile sensing robot skin," Mechanics of Composite Materials, 47(1), pp. 137-144.

[21] Wegener, M., "Piezoelectric polymer foams: transducer mechanism and preparation as well as touch-sensor and ultrasonic-transducer properties," p. 76441A.

[22] Merrell, A. J., Fullwood, D. T., Bowden, A. E., Remington, T. D., Stolworthy, D. K., and Bilodeau, A., "Applications of Nano-Composite Piezoelectric Foam Sensors," Proc. ASME 2013 Conference on Smart Materials, Adaptive Structures, and Intelligent Systems.

[23] Merrell, A. J., Fullwood, D. T., Bowden, A. E., and Remington, T. D., 2015, "Composite material used as a strain gauge," Nano Composite Products, Inc.

[24] Rosquist, P. G., Merrell, A. J., Anderson, B. K., Bird, E. T., Fullwood, D. T., Bowden, A. E., and Ridge, S., 2014, "Application of nano-composite piezoelectric foam in tracking aerobic energy output," CAMXOrlando, FL.

[25] Johnson, O. K., Gardner, C. J., Seegmiller, D. B., Mara, N. A., Dattelbaum, A. M., Rae, P. J., Kaschner, G. C., Mason, T. A., Fullwood, D. T., and Hansen, G., 2011, "Multiscale Model for the Extreme Piezoresistivity in Silicone/Nickel Nanostrand Nanocomposites," Metall. Mater. Trans. A-Phys. Metall. Mater. Sci., 42A(13), pp. 3898-3906.

[26] de la Vega, A., Sumfleth, J., Wittich, H., and Schulte, K., 2012, "Time and temperature dependent piezoresistance of carbon nanofiller/polymer composites under dynamic load," Journal of Materials Science, 47(6), pp. 2648-2657.

[27] Qu, S., and Wong, S.-C., 2007, "Piezoresistive behavior of polymer reinforced by expanded graphite," Composites Science and Technology, 67(2), pp. 231-237.

[28] Avilés, F., May-Pat, A., Canché-Escamilla, G., Rodríguez-Uicab, O., Ku-Herrera, J. J., Duarte-Aranda, S., Uribe-Calderon, J., Gonzalez-Chi, P. I., Arronche, L., and La Saponara, V., 2016, "Influence of carbon nanotube on the piezoresistive behavior of multiwall carbon nanotube/polymer composites," J Intel Mat Syst Str, 27(1), pp. 92-103.

[29] Lozano-Pérez, C., Cauich-Rodríguez, J. V., and Avilés, F., 2016, "Influence of rigid segment and carbon nanotube concentration on the cyclic piezoresistive and hysteretic behavior of multiwall carbon nanotube/segmented polyurethane composites," Composites Science and Technology, 128, pp. 25-32.

[30] Pham, G. T., Park, Y.-B., Liang, Z., Zhang, C., and Wang, B., 2008, "Processing and modeling of conductive thermoplastic/carbon nanotube films for strain sensing," Composites Part B: Engineering, 39(1), pp. 209-216.

[31] Lenicek, I., Ilic, D., and Malaric, R., 2008, "Determination of high-resolution digital voltmeter input parameters," Ieee T Instrum Meas, 57(8), pp. 1685-1688.

[32] Rietveld, G., 2004, "Accurate determination of the input impedance of digital voltmeters," IEE Proc.-Sci. Meas. Technol., 151(5), pp. 381-383.

[33] Davies, D., 1969, "Charge generation on dielectric surfaces," Journal of Physics D: Applied Physics, 2(11), p. 1533.

[34] Fan, F.-R., Lin, L., Zhu, G., Wu, W., Zhang, R., and Wang, Z. L., 2012, "Transparent Triboelectric Nanogenerators and Self-Powered Pressure Sensors Based on Micropatterned Plastic Films," Nano Letters, 12(6), pp. 3109-3114.

[35] Fan, F.-R., Tian, Z.-Q., and Lin Wang, Z., 2012, "Flexible triboelectric generator," Nano Energy, 1(2), pp. 328-334.

[36] Husak, M., and Bily, A., "Model of the triboelectric generator," Proc. Advanced Semiconductor Devices & Microsystems (ASDAM), 2016 11th International Conference on, IEEE, pp. 109-112.

[37] Li, W., Torres, D., Wang, T., Wang, C., and Sepúlveda, N., 2016, "Flexible and biocompatible polypropylene ferroelectret nanogenerator (FENG): On the path toward wearable devices powered by human motion," Nano Energy, 30, pp. 649-657.

[38] Siddiqui, S., Kim, D.-I., Roh, E., Duy, L. T., Trung, T. Q., Nguyen, M. T., and Lee, N.-E., 2016, "A durable and stable piezoelectric nanogenerator with nanocomposite nanofibers embedded in an elastomer under high loading for a self-powered sensor system," Nano Energy, 30, pp. 434-442.

[39] Wang, Z. L., 2015, "Triboelectric nanogenerators as new energy technology and self-powered sensors–Principles, problems and perspectives," Faraday Discuss., 176, pp. 447-458.

[40] Wang, Z. L., 2016, Triboelectric Nanogenerators, Springer International Publishing : Imprint: Springer, Cham.

[41] Akande, A. R., and Lowell, J., 1985, "CONTACT ELECTRIFICATION OF POLYMERS BY METALS," J. Electrost., 16(2-3), pp. 147-156.

[42] Castle, G. S. P., 1997, "Contact charging between insulators," J. Electrost., 40-1, pp. 13-20.

[43] Diaz, A., and Felix-Navarro, R., 2004, "A semi-quantitative tribo-electric series for polymeric materials: the influence of chemical structure and properties," J. Electrost., 62(4), pp. 277-290.

[44] Lowell, J., and Roseinnes, A. C., 1980, "CONTACT ELECTRIFICATION," Advances in Physics, 29(6), pp. 947-1023.

[45] Shin, S. H., Bae, Y. E., Moon, H. K., Kim, J., Choi, S. H., Kim, Y., Yoon, H. J., Lee, M. H., and Nah, J., 2017, "Formation of Triboelectric Series via Atomic-Level Surface Functionalization for Triboelectric Energy Harvesting," Acs Nano, 11(6), pp. 6131-6138.

[46] Wu, Y., Castle, G. S. P., and Inculet, II, 2005, "Particle size analysis in the study of induction charging of granular materials," J. Electrost., 63(3-4), pp. 189-202.

[47] Diamond, A. S., 2001, Handbook of imaging materials, CRC Press.

[48] Merrell, A. J., Fullwood, D. T., Bowden, A. E., Remington, T. D., Stolworthy, D. K., and Bilodeau, R. A., 2013, "Applications of Nano-Composite Piezoelectric Foam Sensors," SMASIS, ASME, Snowbird, UT.

[49] Schönert, K., Eichas, K., and Niermöller, F., 1996, "Charge distribution and state of agglomeration after tribocharging fine particulate materials," Powder technology, 86(1), pp. 41-47.

[50] Şerban, D. A., Weber, G., Marşavina, L., Silberschmidt, V. V., and Hufenbach, W., 2013, "Tensile properties of semi-crystalline thermoplastic polymers: Effects of temperature and strain rates," Polymer Testing, 32(2), pp. 413-425.

[51] White, S. W., Kim, S., Bajaj, A., Davies, P., Showers, D., and Liedtke, P., 2000, "Experimental techniques and identification of nonlinear and viscoelastic properties of flexible polyurethane foam," Nonlinear Dynamics, 22(3), pp. 281-313.

[52] Dounis, D. V., Moreland, J., Wilkes, G. L., Dillard, D. A., and Turner, R. B., 1993, "The mechano‐sorptive behavior of flexible water‐blown polyurethane foams," Journal of applied polymer science, 50(2), pp. 293-301.

[53] Payen, D., 1967, "Title."

[54] Bower, D. I., 2002, An introduction to polymer physics, Cambridge University Press.

[55] Sheth, J. P., Aneja, A., Wilkes, G. L., Yilgor, E., Atilla, G. E., Yilgor, I., and Beyer, F. L., 2004, "Influence of system variables on the morphological and dynamic mechanical behavior of polydimethylsiloxane based segmented polyurethane and polyurea copolymers: a comparative perspective," Polymer, 45(20), pp. 6919-6932.

[56] Szycher, M., 1999, Szycher's handbook of polyurethanes, CRC press.

[57] Merrell, A. J., Fullwood, D. T., Bowden, A. E., Remington, T. D., Stolworthy, D. K., and Bilodeau, A., "Applications of Nano-Composite Piezoelectric Foam Sensors," Proc. ASME 2013 Conference on Smart Materials, Adaptive Structures and Intelligent Systems, American Society of Mechanical Engineers, pp. V001T001A024-V001T001A024.

[58] Merrell, A. J., Christensen, W. F., Seeley, M. K., Bowden, A. E., and Fullwood, D. T., 2017, "Nano-Composite Foam Sensor System in Football Helmets," Annals of Biomedical Engineering, pp. 1-8.

[59] Bird, E. T., Merrell, A. J., Anderson, B. K., Newton, C. N., Rosquist, P. G., Fullwood, D. T., Bowden, A. E., and Seeley, M. K., 2016, "Vibration monitoring via nano-composite piezoelectric foam bushings," Smart Materials and Structures, 25(11), p. 115013.

[60] Manouchehri, H.-R., Hanumantha Rao, K., and Forssberg, K., 2002, "Triboelectric charge, electrophysical properties and electrical beneficiation potential of chemically treated feldspar, quartz and wollastonite," Physical Separation in Science and Engineering, 11(1-2), pp. 9-32.

[61] Carta, M., Alfano, G., Carbini, P., Ciccu, R., and Del Fa, C., 1981, "Triboelectric phenomena in mineral processing. Theoretic fundamentals and applications," Journal of Electrostatics, 10, pp. 177-182.

[62] Ding, L., Xuan, S., Feng, J., and Gong, X., 2017, "Magnetic/conductive composite fibre: A multifunctional strain sensor with magnetically driven property," Composites Part A: Applied Science and Manufacturing, 100(Supplement C), pp. 97-105.

[63] Cannata, G., Maggiali, M., Metta, G., and Sandini, G., "An embedded artificial skin for humanoid robots," Proc. Multisensor Fusion and Integration for Intelligent Systems, 2008. MFI 2008. IEEE International Conference on, IEEE, pp. 434-438.

[64] Dunne, L. E., Brady, S., Smyth, B., and Diamond, D., 2005, "Initial development and testing of a novel foam-based pressure sensor for wearable sensing," Journal of neuroengineering and rehabilitation, 2(1), p. 4.

[65] Gong, S., Schwalb, W., Wang, Y., Chen, Y., Tang, Y., Si, J., Shirinzadeh, B., and Cheng, W., 2014, "A wearable and highly sensitive pressure sensor with ultrathin gold nanowires," Nature communications, 5.

[66] Wichmann, M. H., Buschhorn, S. T., Böger, L., Adelung, R., and Schulte, K., 2008, "Direction sensitive bending sensors based on multi-wall carbon nanotube/epoxy nanocomposites," Nanotechnology, 19(47), p. 475503.

[67] Yao, S., and Zhu, Y., 2014, "Wearable multifunctional sensors using printed stretchable conductors made of silver nanowires," Nanoscale, 6(4), pp. 2345-2352.

[68] Massaro, A., 2011, "Design and Characterization of a Nanocomposite Pressure Sensor Implemented in a Tactile Robotic System," IEEE Transactions on Instrumentation and Measurement, 60(8), pp. 2967-2975.

[69] Cingolani, R., 2011, "Real time optical pressure sensing for tactile detection using gold nanocomposite material," Microelectronic engineering, 88(8), pp. 2767-2770.

[70] Lin, F., Wang, A., Zhuang, Y., Tomita, M. R., and Xu, W., 2016, "Smart Insole: A Wearable Sensor Device for Unobtrusive Gait Monitoring in Daily Life," IEEE Transactions on Industrial Informatics, Industrial Informatics, IEEE Transactions on, IEEE Trans. Ind. Inf., p. 2281.

[71] Massaro, A., Spano, F., Cazzato, P., Cingolani, R., and Athanassiou, A., 2011, "Real time optical pressure sensing for tactile detection using gold nanocomposite material," Microelectronic engineering, 88(8), pp. 2767-2770.

[72] Massaro, A., Spano, F., Cazzato, P., La Tegola, C., Cingolani, R., and Athanassiou, A., 2013, "Robot Tactile Sensing: Gold Nanocomposites As Highly Sensitive Real-Time Optical Pressure Sensors," IEEE Robotics & Automation Magazine, 20(2), pp. 82-90.

[73] Massaro, A., Spano, F., Lay Ekuakille, A., Cazzato, P., Cingolani, R., and Athanassiou, A., 2011, "Design and Characterization of a Nanocomposite Pressure Sensor Implemented in a Tactile Robotic System," IEEE Transactions on Instrumentation and Measurement, 60(8), pp. 2967-2975.

[74] 2017, "XRD Extreme impact protection," http://www.xrd.tech/index.aspx.

[75] Diaz, A. F., and Felix-Navarro, R. M., 2004, "A semi-quantitative tribo-electric series for polymeric materials: the influence of chemical structure and properties," Journal of Electrostatics, pp. 277-290.

[76] Inc., A., "The TriboElectric Series," https://www.trifield.com/content/tribo-electric-series/.

[77] Sun, Y., Amirrasouli, B., Razavi, S., Li, Q., Lowe, T., and Withers, P., 2016, "The variation in elastic modulus throughout the compression of foam materials," Acta Materialia, 110, pp. 161-174.

[78] De Vries, D., 2009, "Characterization of polymeric foams," Eindhoven University of Technology.

[79] Fainaru-Wada, M., and Fainaru, S., 2013, League of denial: The NFL, concussions, and the battle for truth, Three Rivers Press.

[80] Funk, J. R., Duma, S. M., Manoogian, S. J., and Rowson, S., 2007, "Biomechanical risk estimates for mild traumatic brain injury," Annual proceedings / Association for the Advancement of Automotive Medicine. Association for the Advancement of Automotive Medicine, 51, pp. 343-361.

[81] Guskiewicz, K. M., McCrea, M., Marshall, S. W., Cantu, R. C., Randolph, C., Barr, W., Onate, J. A., and Kelly, J. P., 2003, "Cumulative effects associated with recurrent concussion in collegiate football players - The NCAA Concussion Study," Jama-Journal of the American Medical Association, 290(19), pp. 2549-2555.

[82] Guskiewicz, K. M., Marshall, S. W., Bailes, J., McCrea, M., Cantu, R. C., Randolph, C., and Jordan, B. D., 2005, "Association between recurrent concussion and late-life cognitive impairment in retired professional football players," Neurosurgery, 57(4), pp. 719-724.

[83] Guskiewicz, K. M., Marshall, S. W., Bailes, J., McCrea, M., Harding, H. P., Jr., Matthews, A., Mihalik, J. R., and Cantu, R. C., 2007, "Recurrent concussion and risk of depression in retired professional football players," Medicine and Science in Sports and Exercise, 39(6), pp. 903-909.

[84] Patel, D. R., and Greydanus, D. E., 2002, "Neurologic considerations for adolescent athletes," Adolescent Medicine Clinics, 13(3), p. 569.

[85] Patel, D. R., Shivdasani, V., and Baker, R. J., 2005, "Management of sport-related concussion in young athletes," Sports Medicine, 35(8), pp. 671-684.

[86] Buzzini, S. R. R., and Guskiewicz, K. M., 2006, "Sport-related concussion in the young athlete," Current opinion in pediatrics, 18(4), pp. 376-382.

[87] Wojtowicz, M., Iverson, G. L., Silverberg, N. D., Mannix, R., Zafonte, R., Maxwell, B., and Berkner, P. D., 2016, "Consistency of self-reported concussion history in adolescent athletes," Journal of Neurotrauma.

[88] Marar, M., McIlvain, N. M., Fields, S. K., and Comstock, R. D., 2012, "Epidemiology of Concussions Among United States High School Athletes in 20 Sports," The American journal of sports medicine, 40(4), pp. 747-755.

[89] Miyashita, T., Diakogeorgiou, E., Marrie, K., and Danaher, R., 2016, "Frequency and Location of Head Impacts in Division I Men's Lacrosse Players," Athletic Training and Sports Health Care.

[90] Crisco, J. J., Fiore, R., Beckwith, J. G., Chu, J. J., Brolinson, P. G., Duma, S., McAllister, T. W., Duhaime, A. C., and Greenwald, R. M., 2010, "Frequency and location of head impact exposures in individual collegiate football players," Journal of athletic training, 45(6), pp. 549-559.

[91] Crisco, J. J., Wilcox, B. J., Beckwith, J. G., Chu, J. J., Duhaime, A. C., Rowson, S., Duma, S. M., Maerlender, A. C., McAllister, T. W., and Greenwald, R. M., 2011, "Head impact exposure in collegiate football players," J Biomech, 44(15), pp. 2673-2678.

[92] Daniel, R. W., Rowson, S., and Duma, S. M., 2012, "Head Impact Exposure in Youth Football," ANNALS OF BIOMEDICAL ENGINEERING, pp. 976-981.

[93] Rowson, S., Duma, S. M., Greenwald, R. M., Beckwith, J. G., Chu, J. J., Guskiewicz, K. M., Mihalik, J. P., Crisco, J. J., Wilcox, B. J., McAllister, T. W., Maerlender, A. C., Broglio, S. P., Schnebel, B., Anderson, S., and Brolinson, P. G., 2014, "Can helmet design reduce the risk of concussion in football?," J Neurosurg, 120(4), pp. 919-922.

[94] Young, T. J., Daniel, R. W., Rowson, S., and Duma, S. M., 2014, "Head Impact Exposure in Youth Football: Elementary School Ages 7-8 Years and the Effect of Returning Players," Clinical Journal of Sport Medicine, 24(5), pp. 416-421.

[95] Zanetti, E. M., Bignardi, C., Franceschini, G., and Audenino, A. L., 2013, "Amateur football pitches: Mechanical properties of the natural ground and of different artificial turf infills and their biomechanical implications," Journal of Sports Sciences, 31(7), pp. 767-778.

[96] Camarillo, D. B., Shull, P. B., Mattson, J., Shultz, R., and Garza, D., 2013, "An instrumented mouthguard for measuring linear and angular head impact kinematics in American football," Annals of biomedical engineering, 41(9), pp. 1939-1949.

[97] Higgins, M., Halstead, P. D., Snyder-Mackler, L., and Barlow, D., 2007, "Measurement of impact acceleration: mouthpiece accelerometer versus helmet accelerometer," Journal of athletic training, 42(1), p. 5.

[98] Wu, L. C., Zarnescu, L., Nangia, V., Cam, B., and Camarillo, D. B., 2014, "A Head Impact Detection System Using SVM Classification and Proximity Sensing in an Instrumented Mouthguard," Ieee T Bio-Med Eng, 61(11), pp. 2659-2668.

[99] Duma, S. M., Manoogian, S. J., Bussone, W. R., Brolinson, P. G., Goforth, M. W., Donnenwerth, J. J., Greenwald, R. M., Chu, J. J., and Crisco, J. J., 2005, "Analysis of real-time head accelerations in collegiate football players," CLINICAL JOURNAL OF SPORT MEDICINE, pp. 3-8.

[100] Olvey, S. E., Knox, T., and Cohn, K. A., 2004, "The development of a method to measure head acceleration and motion in high-impact crashes," Neurosurgery, 54(3), pp. 672-677.

[101] Knox, T., Pellettiere, J., Perry, C., Plaga, J., and Bonfeld, J., 2009, "New Sensors to Track Head Acceleration during Possible Injurious Events," DTIC Document.

[102] Rowson, S., Beckwith, J. G., Chu, J. J., Leonard, D. S., Greenwald, R. M., and Duma, S. M., 2011, "A Six Degree of Freedom Head Acceleration Measurement Device for Use in Football," Journal of Applied Biomechanics, 27(1), pp. 8-14.

[103] Siegmund, G. P., Guskiewicz, K. M., Marshall, S. W., DeMarco, A. L., and Bonin, S. J., 2016, "Laboratory validation of two wearable sensor systems for measuring head impact severity in football players," Annals of biomedical engineering, 44(4), pp. 1257-1274.

[104] Hanlon, E. M., and Bir, C. A., 2012, "Real-Time Head Acceleration Measurement in Girls' Youth Soccer," Medicine and Science in Sports and Exercise, 44(6), pp. 1102-1108.

[105] Jadischke, R., Viano, D. C., Dau, N., King, A. I., and McCarthy, J., 2013, "On the accuracy of the Head Impact Telemetry (HIT) System used in football helmets," Journal of Biomechanics, 46(13), pp. 2310-2315.

[106] Rowson, S., and Duma, S. M., 2011, "Development of the STAR evaluation system for football helmets: integrating player head impact exposure and risk of concussion," Ann Biomed Eng, 39(8), pp. 2130-2140.

[107] Manoogian, S., McNeely, D., Goforth, M., Brolinson, G., and Duma, S., 2006, "Head acceleration is less than 10 percent of helmet acceleration during a football impact," Biomed Sci Instrum, 42, pp. 383-388.

[108] Campbell, K. R., Warnica, M. J., Levine, I. C., Brooks, J. S., Laing, A. C., Burkhart, T. A., and Dickey, J. P., 2016, "Laboratory evaluation of the gForce Tracker™, a head impact kinematic measuring device for use in football helmets," Annals of biomedical engineering, 44(4), pp. 1246-1256.

[109] Duma, S. M., Manoogian, S. J., Bussone, W. R., Brolinson, P. G., Goforth, M. W., Donnenwerth, J. J., Greenwald, R. M., Chu, J. J., and Crisco, J. J., 2005, "Analysis of real-time head accelerations in collegiate football players," Clin J Sport Med, 15(1), pp. 3-8.

[110] Hernandez, F., Wu, L. C., Yip, M. C., Laksari, K., Hoffman, A. R., Lopez, J. R., Grant, G. A., Kleiven, S., and Camarillo, D. B., 2015, "Six Degree-of-Freedom Measurements of Human Mild Traumatic Brain Injury," Ann Biomed Eng, 43(8), pp. 1918-1934.

[111] Conidi, F. X., 2015, "Helmets, sensors, and more: a review," Pract Neurol, 15(2), pp. 32-36.

[112] Higgins, M., Halstead, P. D., Snyder-Mackler, L., and Barlow, D., 2007, "Measurement of impact acceleration: Mouthpiece accelerometer versus helmet accelerometer," Journal of athletic training, 42(1), pp. 5-10.

[113] Allison, M. A., Kang, Y. S., Bolte, J. H., Maltese, M. R., and Arbogast, K. B., 2014, "Validation of a Helmet-Based System to Measure Head Impact Biomechanics in Ice Hockey," Medicine and Science in Sports and Exercise, 46(1), pp. 115-123.

[114] Gurdjian, E., Lissner, H., Latimer, F., Haddad, B., and Webster, J., 1953, "Quantitative Determination of Acceleration and Intracranial Pressure in Experimental Head Injury Preliminary Report," Neurology, 3(6), pp. 417-417.

[115] Gurdjian, E. S., Hodgson, V. R., Hardy, W., Patrick, L., and Lissner, H., 1964, "EVALUATION OF THE PROTECTIVE CHARACTERISTICS OF HELMETS IN SPORTS," Journal of Trauma and Acute Care Surgery, 4(3), pp. 309-324.

[116] Gurdjian, E. S., Roberts, V., and Thomas, L. M., 1966, "Tolerance curves of acceleration and intracranial pressure and protective index in experimental head injury," Journal of Trauma and Acute Care Surgery, 6(5), pp. 600-604.

[117] Versace, J., 1971, "A review of the severity index," No. 0148-7191, SAE Technical Paper.

[118] Hutchinson, J., Kaiser, M. J., and Lankarani, H. M., 1998, "The Head Injury Criterion (HIC) functional," Applied Mathematics and Computation, 96(1), pp. 1-16.

[119] Funk, J. R., Rowson, S., Daniel, R. W., and Duma, S. M., 2012, "Validation of concussion risk curves for collegiate football players derived from HITS data," Annals of biomedical engineering, 40(1), pp. 79-89.

[120] Gadd, C. W., 1966, "Use of a weighted-impulse criterion for estimating injury hazard," No. 0148-7191, SAE Technical Paper.

[121] NOCSAE, 2014, "Standard Performance Specification for Newly Manufactured Football Helmets," National Operating Committee on Standards for Athletic Equipment.

[122] Foster, J. K., Kortge, J. O., and Wolanin, M. J., 1977, "Hybrid III-A Biomechanically-Based Crash Test Dummy," SAE Technical Paper Series, SAE International.

[123] NOCSAE, 2015, "Standard test method and equipment used in evaluating the performance characteristics of protective headgear/equipment.."

[124] Tianyi, F.-L., Agbor, V. N., and Njim, T., 2017, "Motorbike-handlebar hernia-a rare traumatic abdominal wall hernia: a case report and review of the literature," Journal of medical case reports, 11(1), p. 87.

[125] Guskiewicz, K. M., and Mihalik, J. P., 2011, "Biomechanics of sport concussion: quest for the elusive injury threshold," Exercise and sport sciences reviews, 39(1), pp. 4-11.

[126] Lee, L. J., Zeng, C., Cao, X., Han, X., Shen, J., and Xu, G., 2005, "Polymer nanocomposite foams," 20th Anniversary Special Issue, 65(15â€“16), pp. 2344-2363.

[127] Alonso, M. V., Auad, M. L., and Nutt, S., 2006, "Short-fiber-reinforced epoxy foams," Composites Part A: Applied Science and Manufacturing, 37(11), pp. 1952-1960.

[128] Mahfuz, H., Rangari, V. K., Islam, M. S., and Jeelani, S., 2004, "Fabrication, synthesis and mechanical characterization of nanoparticles infused polyurethane foams," Composites Part A: Applied Science and Manufacturing, 35(4), pp. 453-460.

[129] Sun, L., Gibson, R. F., Gordaninejad, F., and Suhr, J., 2009, "Energy absorption capability of nanocomposites: a review," Composites Science and Technology, 69(14), pp. 2392-2409.

[130] Shen, H., and Nutt, S., 2003, "Mechanical characterization of short fiber reinforced phenolic foam," Composites Part A: Applied Science and Manufacturing, 34(9), pp. 899-906.

[131] Saha, M. C., Kabir, M. E., and Jeelani, S., 2009, "Effect of Nanoparticles on Mode-I Fracture Toughness of Polyurethane Foams," Polymer Composites, 30(8), pp. 1058-1064.

[132] Zeng, Z., Gui, X., Lin, Z., Zhang, L., Jia, Y., Cao, A., Zhu, Y., Xiang, R., Wu, T., and Tang, Z., 2013, "Carbon Nanotube Sponge-Array Tandem Composites with Extended Energy Absorption Range," Advanced Materials, 25(8), pp. 1185-1191.

APPENDIX A. TABLES

Table 0-1: Additive surface area by additive type. A BET analysis was used to determine all surface area with the exception of the fiber materials (NCF and PX30) which were provided by manufacturer.

Additive	Analysis Bath Temp (K)	Sample Weight (g)	BET Surface Area (m^2/g)	BET Surface Area Certainty (m^2/g)	BET Constant	Correlation Coefficient
Carbon Black	77.3	0.1256	62.3088	0.4326	181.747	1.00E+00
CNTs	77.3	0.0957	110.802	0.7931	214.226	1.00E+00
F104	77.3	0.1227	6.4008	0.0614	132.8611	1.00E+00
M103	77.3	0.1044	11.6818	0.1113	134.2129	1.00E+00
Novamet	77.3	4.4627	0.5046	0.0009	108.837	1.00E+00
P103	77.3	0.1175	16.7859	0.0566	193.5884	1.00E+00
Copper	77.3	4.8962	0.2748	0.001	26.5147	1.00E+00
NCF	N/A	N/A	0.31614	0.0001	N/A	N/A
PX30	N/A	N/A	0.3289	N/A	N/A	N/A

Table 0-2: Statistical analysis for polyurethane vs silicone foam

Term	Estimate	Std. Error	Prob > |t|	Lower 95%	Upper 95%
Intercept	931,551	286,860	0.0020	355,924	1,507,177
Foam Type [Poly]	-572,987	303,374	0.0645	-1,181,750	35,777
Porosity	-1,399,389	534,532	0.1160	-2,472,006	-326,773
Foam Type [Poly]*Porosity	1,025,545	563,641	0.0746	-105,483	2,156,573

Table 0-3: Parameter estimates from statistical analysis of NCCF content in polyurethane foam.

Term	Estimate	Std. Error	Prob > |t|	Lower 95%	Upper 95%
Intercept	106,758	7,867	<0.0001	90,904	122,612
NCCF by Weight (%)	15,504	2,116	<0.0001	11,240	19,768

Table 0-4: Parameter estimates from statistical analysis of NCCF content and length in polyurethane foam.

Term	Estimate	Std. Error	Prob > |t|	Lower 95%	Upper 95%
Intercept	264,997	60,936	<0.0001	141,840	388,154
NCCF by Weight (%)	15,912	1,695	<0.0001	12,486	19,338
Length (mm)	36,908	12,053	0.0039	12,549	61,267
Porosity	-335,332	106,300	0.003	-550,173	-120,492